Biomineralization and Biomimetic Materials Chemistry: Exploring the Influence of Crystal Growth Modifier

A Dissertation submitted to the
Indian Institute of Technology Guwahati
As Partial Fulfillment for the Degree of
Doctor of Philosophy

Submitted by
Ballav Moni Borah

Department of Chemistry
Indian Institute of Technology Guwahati
October 2008

Biomineralization and Biomimetic Materials Chemistry: Exploring the Influence of Crystal Growth Modifier

Submitted by

Ballav Moni Borah

Department of Chemistry

Indian Institute of Technology Guwahati

Guwahati-781039

October 2008

Dedicated to my beloved Parents

and Brother

…….Ballav

INDIAN INSTITUTE OF TECHNOLOGY, GUWAHATI

Department of Chemistry

STATEMENT

I do hereby declare that the matter embodied in this thesis is the result of investigations carried out by me in the Department of Chemistry, Indian Institute of Technology Guwahati, India under the guidance of Dr. Gopal Das, Associate Professor, Department of Chemistry, Indian Institute of Technology Guwahati, India.

In keeping with the general practice of reporting scientific observations, due acknowledgements have been made wherever the work described is based on the findings of other investigators.

October, 2008 (Ballav Moni Borah)

I.I.T. Guwahati

INDIAN INSTITUTE OF TECHNOLOGY GUWAHATI

Department of Chemistry

CERTIFICATE

This is to certify that Ballav Moni Borah has been working under my supervision since July, 2004 as a regular registered Ph. D. student. I am forwarding his thesis entitled "**Biomineralization and Biomimetic Materials Chemistry: Exploring the Influence of Crystal Growth Modifier**" being submitted for the Ph. D. (Science) Degree of this Institute. I certify that he has fulfilled all the requirements according to the rules of this Institute regarding the investigations embodied in his thesis and this work has not been submitted elsewhere for a degree.

October, 2008
I.I.T. Guwahati

(Dr. Gopal Das)
Supervisor

INDIAN INSTITUTE OF TECHNOLOGY, GUWAHATI

Department of Chemistry

CERTIFICATE OF COURSE WORK

This is to certify that Ballav Moni Borah has satisfactorily completed all the courses required for the Ph.D degree program. These courses include

CH 603:	Supramolecules: Concepts and Applications
CH 627:	New Reagents for Organic Chemistry
CH 630:	Physical Methods inChemistry
CH 632:	Advanced Group Theroy and Application

Ballav Moni Borah has successfully completed his Ph.D qualifying examination in May 2005.

Prof. A. T. Khan
Head, Department of Chemistry
I. I. T. Guwahati

Dr. T. Punniyamurthy
Secretary, DPPC
I. I. T. Guwahati

Acknowledgements

The results of the works reported in the thesis are based on interdependence rather than independence, which reflect where I have been escorted and supported by many people and that gives me a pleasant opportunity to express my gratitude to all of them. First and foremost, with a deepest sense of gratitude, I would like to express my sincere gratitude to my supervisor Dr. Gopal Das for introducing me into this interdisciplinary topic "Biomineralization" and giving me the freedom to pursue my own interests. I earnestly thank him for his astute guidance, encouragement, inspiration and creative and scientific ideas, which helped me to enhance my knowledge in this field and made my pursuit really exciting.

I would like to acknowledge my sincere gratitude to all my doctoral committee members, Dr. Manabendra Ray, Professor Bhisma K. Patel and Dr. Aiyagari Ramesh for their insightful advices and valuable suggestions.

I would like to offer special thanks to Professor M. K. Chaudhuri and Professor A. T. Khan for their constant inspiration and help right from my M.Sc. days. I would also like to mention Professor Arun Chattopadhyay for extending his laboratory facilities.

I am thankful to the Institute, Indian Institute of Technology Guwahati for providing me with the state of the art infrastructure and facilities for advanced research. My sincere thanks are due to all other faculty members in the Department of Chemistry for their help and encouragement and the non-teaching staffs of the Department for their technical support. I would like to take this opportunity to thank Department of Biotechnology, Centre for Nanotechnology and Department of Physics for proving me the necessary instrumental facilities during the entire duration of my research tenure. I am highly indebted to Dr. Mamoranjan Kar, who gave me constant help and encouragement during my research time. I wish to thank both Kaustav Acharya and Indrajit Talukdar, who readily helped me in recording PXRD for my samples. My sincere thanks to Chandan Borgohain and K. Senapati of Central Instruments facility, IIT Guwahati for their help in all the characterizations (SEM, NMR *etc.*) required during my research work.

I would like to thank my group members Harjyoti, Avijit, Bimlesh, Bedabrata, Sandeep and all other former group members Bhaskar Bhuyan, Mausumi Bhuyan, Hema Laksmi, Srinivas, Mrinmoy for their timely help, support and for the wonderful time we shared during this period. I am also thankful to Dr. P. K. Iyer and his former group members, Jasmine and Swastibrata, for their help and pleasant association with whom we shared the lab in the initial stage of my research.

I extend my sincerest thanks to my top friends Dr. Sahid Hussain, Sonit, Prasanta, Dr. Lokman Hakim Choudhury, Rik Rani, Gunin da, Pranjal da, Bolin da, Dr. Biplab Sarkar, Dr. Santanu Sinha, Krishna Kanti, Jashmini, Dr. Biswa Ranjan Panda, Saitanya, Susanda, Manas, Anupam, Bhaskar Krishnatreya, Harjyoti, Deepankar, Partho, Dhruba, Rupam, Satish, Dr. P. Gopinath and Akashi for their constant help, motivation, enthusiastic company and all the wonderful time we spent in various events.

I also take this opportunity to thank my Department seniors Dr. Papori Goswami, Dr. Rupam Jyoti Sarma, Dr. Kavala Veera Babu, Dr. Bachu Rama Raju, Dr. Subrata Ghosh, Dr. Sarala Naik, Dr. Tridip Sarma, Dr. Deepa Dey, Dr. Devasish Choudhury, Dr. Ejabul Mondal, Dr. Arup Purkayastha, Dr. Geetanjali Majumdar, Dr. Lopamudra Homchoudhury, Dr. Priti Rani Sahoo for lending their hands of support whenever needed.

I would like to thank Dr. S. K. Dwivedy and Barun for the simulation works. Further, thanks are also due to Atul Kumar Singh, who helped me with the bio related works. I would also like to mention Dr. Purnananda Nandi for giving access to use the furnaces in his laboratory in Department of Physics during the early part of my research.

I would like to offer my special thanks to my IIT Guwahati M.Sc. batch mates Bani, Ankur, Angshuman, Sumana and Mausumi for their constant unfailing support, their encouragement and all the help they extended from time to time whenever required. I would also like to extend my gratitude to my old friends Arunabhiram, Prasanta and Kaustavmoni. Here special regards are also due to all my esteemed teachers of Department of Chemistry, B. Borooah College, Guwahati.

I wish to express my appreciation to my other friends in the campus and my 2004 Ph.D. batch mates for the wonderful time I had with them. I also thank all my Orkut and Google talk friends who shared their thoughts and views with me.

The financial support from Council of Scientific and Industrial Research (CSIR), New Delhi in the form of JRF and SRF is duly acknowledged.

Finally, my Ph. D. endeavor could not be completed without the endless love, unending support, tolerance and blessings from my family. I wish to express my sincere gratitude to my parents, especially to my father, and my brother. They are the main soul and inspiration for each and every step that I achieve in my life.

Ballav Moni Borah

Synopsis

SYNOPSIS

The thesis entitled, “Biomineralization and Biomimetic Materials Chemistry: Exploring the Influence of Crystal Growth Modifier” is divided into four chapters.

Chapter-1 gives a brief introduction regarding background as well as literature survey of Biomineralization. It describes how in nature, hard tissues of organism such as bone, teeth and mollusk shells *etc.* forms and their characteristics. It also describes the literature survey of *in vitro* biomineralization in presence of low as well as high molecular weight matrix.

The various bioinorganic materials present in living systems are biominerals. *e.g*, Hydroxyapatite [$Ca_5(PO_4)_3(OH)$], Calcite ($CaCO_3$) *etc.* They are formed by all the living organisms starting from bacteria to higher plants and animals. It has shapes and size which are frequently different from analogous inorganic crystals. They are organized hierarchallly and ordered at many length scales. Biominerals have very low solubility in the body fluid. Low solubility product of Ca salt is the main reason why it is the most abundantly found element in the naturally occurring biomineral. They are thermodynamically stable than the analogous inorganic crystals due to the consideration of the ionic size, charge, packing, and their effect on hydration and lattice energies.

Biomineralization is the process of mineralization in living organisms or *in vivo* in an organized manner under the control of acidic organic macromolecules (protein, amylose, etc.) excreted by the specific positions of living organisms, and the hallmark of this process is that the nucleation of the inorganic phase is strictly controlled by the organic phase. The materials can be deposited intra or extra cellular space and are intimately connected to cellular metabolic processes.

Chapter-2 discusses the role of low-molecular-weight growth modifier in biomineralization. This chapter is subdivided into two parts. First part discusses about biomineralization in presence of low-molecular-weight poly-carboxylate derived from amino acids. Second part describes about the influence of organic and inorganic additives in $CaCO_3$ polymorph synthesis.

For last two decades, extensive studies have been done on the biomineralization of Ca. It has been established that the biominerals grow on the organic template containing O and N donor atoms. Group II metals prefer hard O donor ligands according to HSAB principle. A study of $CaCO_3$ crystal binding motif of naturally occurring biominerals reveal the fact that they are grown on proteins containing a special kind of sequence that mainly contains Asp and Glu residues. Depending on the amino acids present at the nucleation center biominerals grow with different morphology that performs various physiological roles. The synthesis of poly-carboxylate ligands derived from naturally occurring α-amino acids reacting with chloro acetic acid at basic pH following Scheme 1.

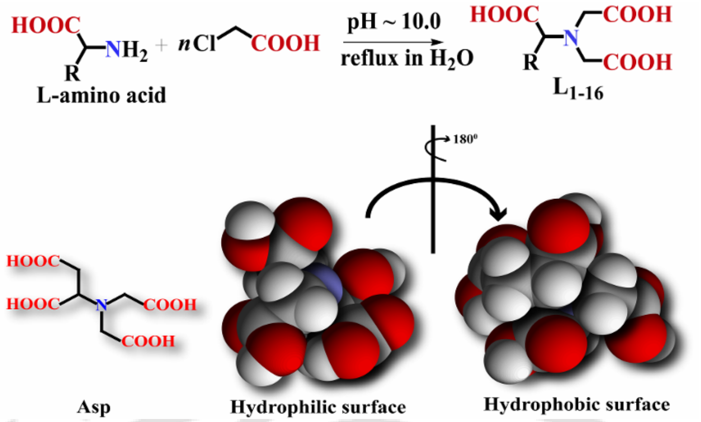

Scheme 1. Synthesis of poly-carboxylate ligands and its space fill model.

The polymorph synthesis of $CaCO_3$ in presence of various organic as well as inorganic additives in different solvents is presented in the second part. The effect of additives has been discussed mechanistically. Vaterite is the major polymorph in non-aqueous solvents irrespective of additives. Coordinating organic additives form extended 3D co-coordination polymers when used stochiometrically. These metal complexes form exclusively porous calcite on thermal decomposition. To establish the thermodynamic stability of different polymorph of $CaCO_3$, temperature dependent experiments were carried out in detail (Scheme 2). Calcite is the major polymorph at two extreme temperatures (-190°C and 189°C).

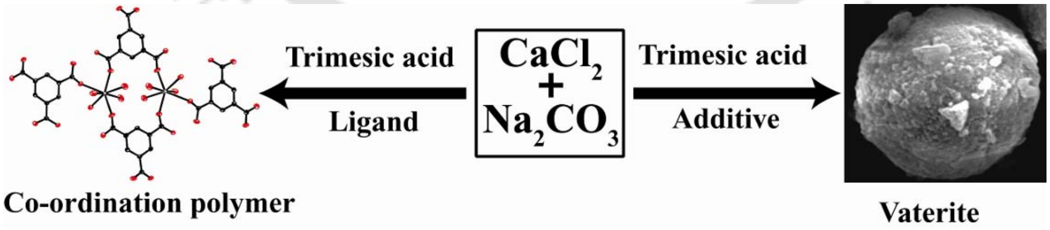

Scheme 2. Additive control polymorph synthesis of $CaCO_3$.

Chapter 3 concerns with the biogenic mineral growth modification in presence of naturally occurring high-molecular-weight matrix. This chapter is divided into three parts. First part discusses the role of naturally occurring high-molecular-weight acidic proteins from lemon extract as a growth modifier of calcium and barium minerals. Second part describes the role of bacterial proteins as a high-molecular-weight organic matrix and the third part deals with biomimetic modulation of crystal morphology using gel diffusion techniques. Crystalline superstructures of Calcium and Barium minerals were synthesized that form micron-sized building blocks in the presence of high-molecular-weight proteins extracted from lemon as shown in the scheme 3, which act as an organic growth modifier. Spherulitic growth of crystalline calcite on the expense of metastable amorphous calcium carbonate (ACC) has been observed (Figuire 1).

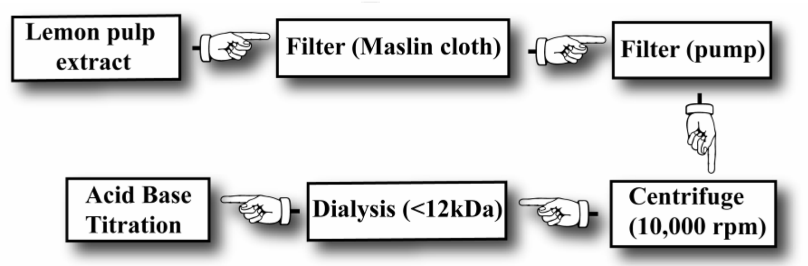

Scheme 3. Extraction of high-molecular-weight acidic proteins from lemon.

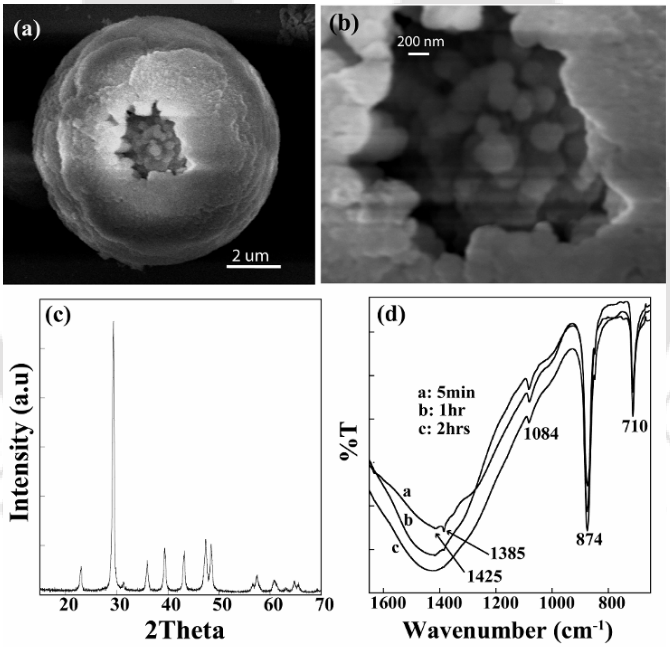

Figure 1. (a) SEM micrographs of hollow spherulitic Calcite, (b) Calcite nano-spherulites, (c) PXRD pattern of Calcite crystals and (d) Time dependent FT-IR analysis with characteristics humps at 1425 & 1386 cm^{-1}.

The role of three different lactic acid bacteria (LAB) *viz*: *Lactobacillus plantarum* MTCC 1325, *Lactobacillus acidophilus* MTCC 4495 and *Pediococcus acidilactici* CFR K7 in the formation of crystalline superstructures of calcium and barium minerals that forms micron-sized building blocks has been discussed in this second part of the chapter. The influence of these bacterial extracts on the crystallization behavior was investigated in details to test the basic coordination behavior of the acidic protein. The significant role of native form of high-molecular-weight bacterial protein extracts in the generation of nucleation centers for crystal growth is also established. A model for the formation of organic matrix-cation complex and the subsequent events leading to crystal growth modification is proposed (Scheme 4). Reproducibly formations of highly pure crystalline minerals phase are highlighted here.

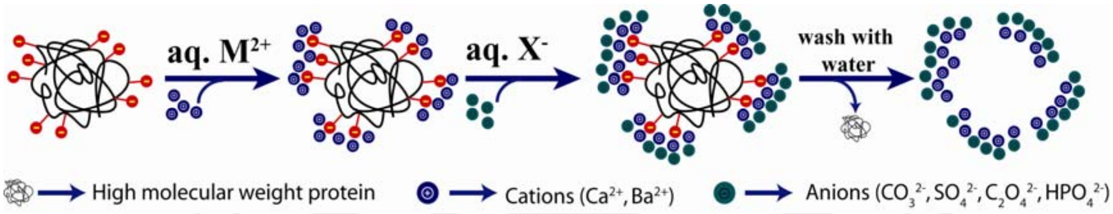

Scheme 4. Proposed mechanism of template action of protein extract.

Gel-diffusion-precipitation methodology is unique. This effective method is capable of characterizing the effects of matrix molecules on mineralization while only using very small quantities of material. In this part we have discussed the versatility of agar-agar and agarose gel in morphosynthesis of different calcium and barium minerals. We have shown the formation of different nano to micron-scale architectures of calcium and barium minerals in presence of these hydrogels. They are formed by well known gel diffusion technique when doped with soluble calcium/barium salts and anions are allowed to diffuse through pores (Figure 2).

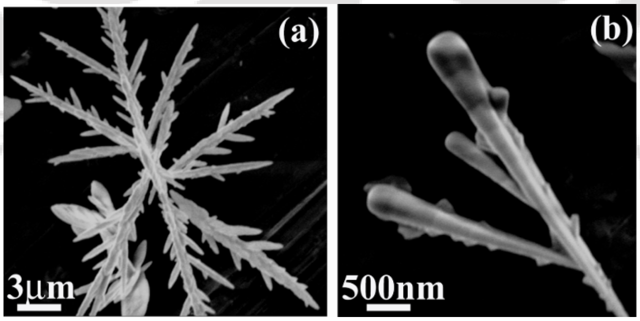

Figure 2. Formation of Barite needles in presence of (a) agar-agar and (b) agarose gel.

Chapter 4 deals with precursor synthesis of inorganic minerals and their characterization. This chapter is subdivided into three parts. First part discusses the synthesis, characterization and application of metal oxides by precursor synthesis method. Second part discusses synthesis, characterization of metal ferrites and the final parts deals with magnetite mineralization and its surface modification.

Precursor synthesis is one of the well established solid-state methods to prepare inorganic mineral. Crystalline precursor complexes transform to other known crystalline mineral phases at higher temperatures *via* calcination-reconstruction method. Among the various inorganic materials, metal oxides have attracted increasing technological and industrial interest. We have carried out synthesis of few metal oxides by precursor synthesis method following Scheme 5. Such synthetic methodology is easy, quantitative and reproducible. All organic precursor salts and thermally decomposed products were characterized in detail (Figure 3).

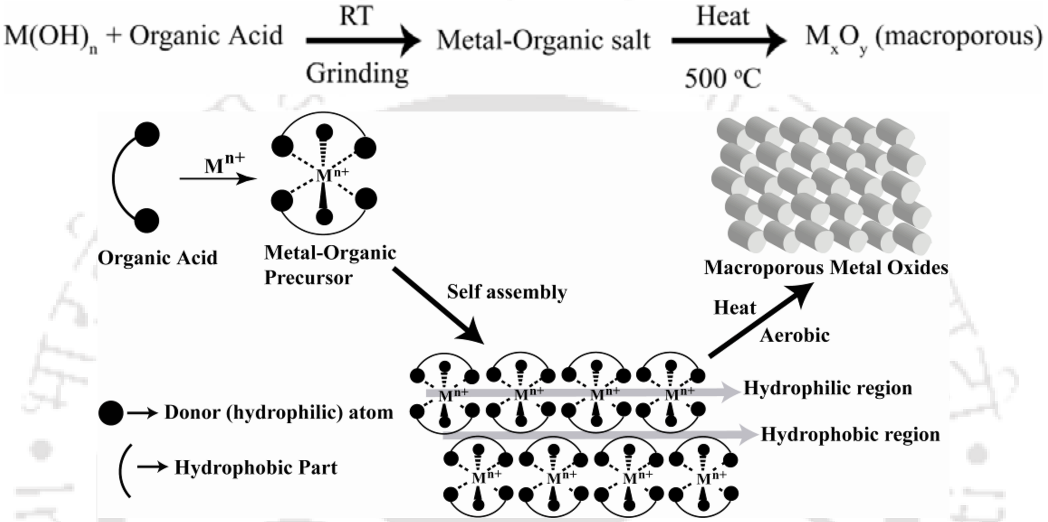

Scheme 5. Synthesis of metal oxides by thermolysis of Metal-organic precursor salts.

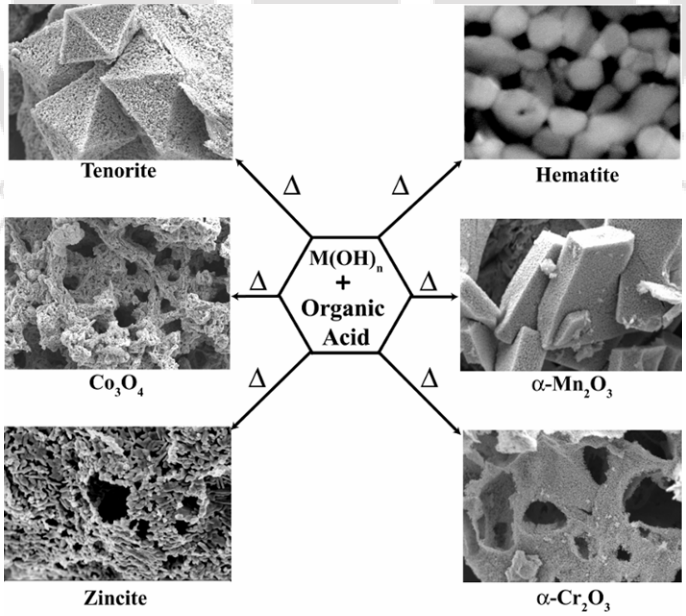

Figure 3. Macroporous metal oxides obtained by thermal decomposition of precursor complex.

Spinel of the type $M^{2+}M_2^{3+}O_4$, when M^{3+} = Fe, the resulting spinel ferrites having a general chemical composition of MFe_2O_4 (M = Mn, Co, Ni, Cu, Zn) have been widely applied as magnetic materials in various biomedical applications. We have carried out synthesis of soft ferrites by precursor synthesis method following Scheme 6.

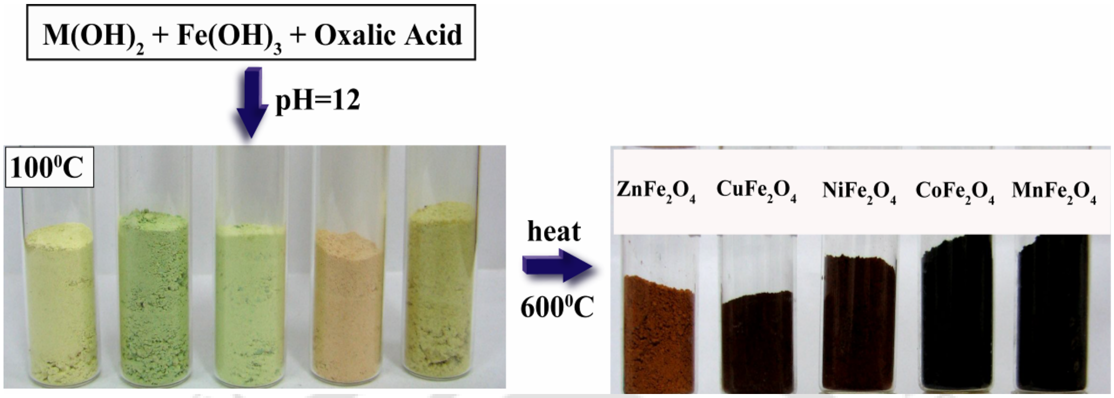

Scheme 6. Synthesis of metal ferrites by thermolysis of M(II)-organic precursor salts.

Magnetite (Fe_3O_4) is a natural magnet and is a member of the spinel group. Magnetite biomineralization is a universal phenomena which is evident in a number of microorganisms *e.g.* magnetotactic bacteria under ambient conditions. We report here the formation and growth modification of magnetite micro crystalline minerals in Agarose gel (Scheme 7).

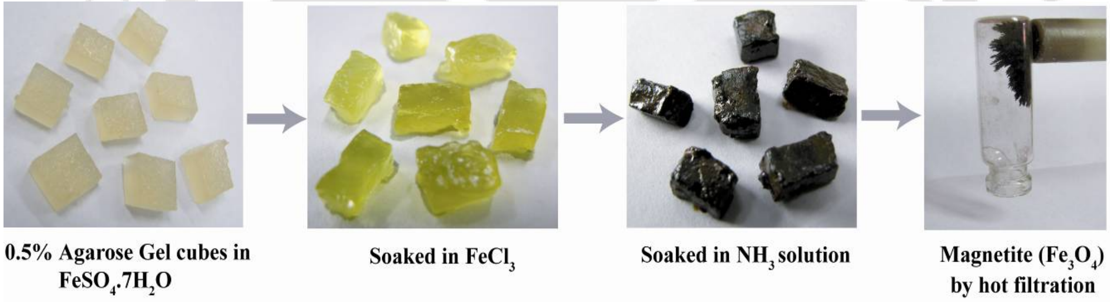

Scheme 7. Magnetite mineralization in Agarose Gel.

We have carried out surface modification of these magnetite particles by Trimesic acid (TMA) and stearic acid. Surface modification results in the complete change in their adsorption behavior, which has various practical applications such as protein adsorption, separation etc. Stearic acid modification generates a hydrophobic surface upon coating on magnetite particles whereas trimesic acid modification generates an improved hydrophilic surface. Change of the water adsorption behavior of the stearic acid coated magnetite particles has been shown in Figure 4.

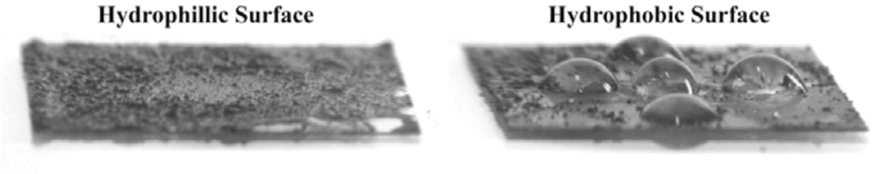

Figure 4. Surface modification of magnetite particle with stearic acid.

We have studied the protein interaction phenomenon with bare magnetite particles and the changes in adsorption features upon surface modification. Bovine serum albumin (BSA) was taken as a model study. Detail conformational features of BSA are known therefore it would be easier to analyze the conformational change of BSA at the interface upon adsorption (Pink-native BSA, Blue-changed BSA). Equilibrium adsorption capacity and protein conformation at the interface was studied with these as-prepared and surface modified particles. Fluorescence labeled magnetite particles has been synthesized by adsorbing Fluorescein onto the surface as shown in Figure 5.

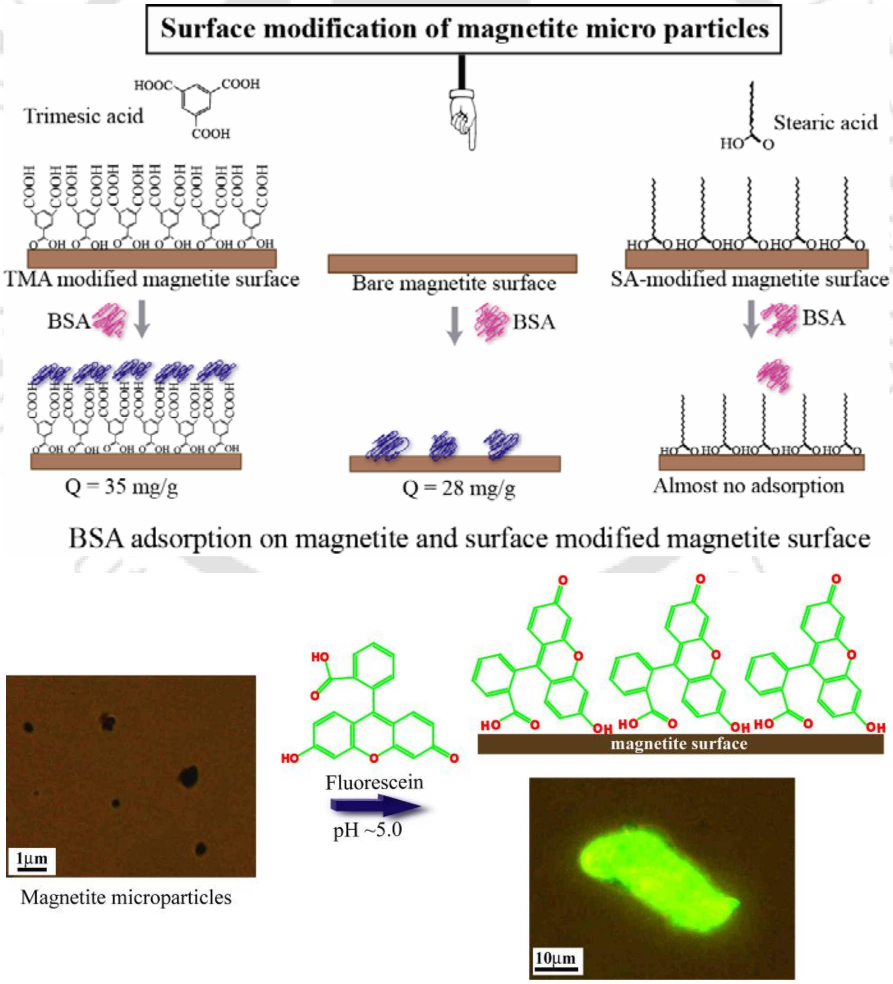

Figure 5. Adsorption of fluorescein by magnetite micro particles.

Contents

Chapter 1 – Introduction

Chapter 2 - Biomineralization in presence of Low-Molecular-Weight growth modifier

2.1 Biomineralization in presence of Low-Molecular-Weight Poly- Carboxylate ligand derived from naturally occurring amino acids

2.1.4. Results and discussions

2.2 Polymorphism in $CaCO_3$

2.2.2. Results and Discussions

Chapter 3 - Biogenic mineral growth modification in presence of High-Molecular-Weight matrix

3.1. High-molecular-weight acidic proteins as a crystal growth modifier

3.1.1. Experimental Section

3.1.2. Results and discussions

3.2. Lactic Acid Bacterial (LAB) extract as a growth modifier of minerals

3.2.1. Experimental Section

3.2.2. Results and discussions

3.3. Modulation of crystal morphology using gel diffusion technique

3.3.2. Results and discussions

Chapter 4 - Precursor synthesis and applications of inorganic materials

4.1. Synthesis and application of metal oxides

4.1.1. Experimental Section

4.1.2. Results and discussions

4.2. Synthesis and application of Soft Metal Ferrites

4.2.1. Experimental Section

4.2.2. Results and discussions

4.3. Gel mediated Magnetite mineralization

4.3.1. Experimental Section

4.3.2. Results and discussions

Chapter - 1

Introduction

1.1 Biomineralization

Scientists and engineers have long been inspired by the beautiful structures and functional properties of the materials formed within living organisms. In nature, hard tissues of organism such as bone, teeth and mollusk shells consists of a crystalline inorganic phase (biomineral) within a polymeric organic matrix [1.1], and thus are bio-composites. Biomineral (Figure 1.1) are the bridge between the living, organic and the mineral world. The various bioinorganic materials present in living systems are biominerals. *e.g*, Hydroxyapatite [$Ca_5(PO_4)_3(OH)$], Calcite ($CaCO_3$) *etc*. Biominerals are formed by all the living organisms starting from bacteria to higher plants and animals.

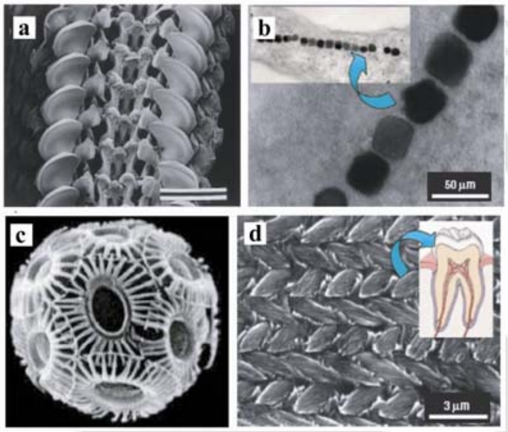

Figure 1.1. (a) Scanning electron microscope (SEM) of radula of the chiton *Acanthopleura hirtosa* (Chiton teeth) Fe_3O_4, Magnetite biomineral, (b) Fe_3O_4, Magnetite nanoparticles formed by magnetotactic bacterium (*Aquaspirillum magnetotacticum*), (c) Calcified scales (coccolith) in marine alga *Emiliania huxleyi* and (d) Mouse enamel consisting of hydroxyapatite crystallites that assemble into woven rod structure.

Biominerals has shapes and size which are frequently different from analogous inorganic crystals [1.1, 1.2]. Biomineral crystals may not have a defined crystal habit at all. They are organized hierarchallly and ordered at many length scales. Biominerals have very low solubility in the body fluid. Low solubility product of Ca salt is the main reason why it is the most abundantly found element in the naturally occurring biomineral [1.2]. They are thermodynamically stable than the analogous inorganic crystals due to the consideration of the ionic size, charge, packing, and their effect on hydration and lattice energies. In living organisms, biominerals perform various functions like

- Robust support and defense structures (mollusk shell, skeleton)
- As sensors (dense -2.9 gm/cm^3, spindle in the inner ear to sense acceleration)
- As tools and weapons (teeth)
- As storage (Fe_2O_3 stored in ferritin protein)
- For detoxification (deposition of toxic CdS)

Biomineralization is the process of mineralization in living organisms or *in vivo* in an organized manner [1.3] under the control of acidic organic macromolecules [1.4] (protein, amylose, etc.) excreted by the specific positions of living organisms, and the hallmark of this process is that the nucleation of the inorganic phase is strictly controlled by the organic phase [1.5]. The materials can be deposited intra or extra cellular space and are intimately connected to cellular metabolic processes. Biomineralization as a field of scientific study falls within several branches of sciences including biochemistry, biology, condensed mater physics, geology, inorganic chemistry, and molecular biology. The aqueous precipitation of inorganic crystals forming minerals is a straight forward laboratory procedure, but growth of these crystals in the preorganized way as the biominerals grow is a very tedious job. There is a strong interrelationship between biomineralization and biomimetic material chemistry [1.6]. There are several stages in the biological mineralization process:

1. Supramolecular Preorganization
2. Interfacial Molecular Recognition
3. Vectorial Regulation
4. Cellular Processing

Figure 1.2 shows a biomineralization paradigm, which is not general: it applies to some prokaryotic and many eukaryotic biominerals. Supramolecular pre-organization is the initial stage of biomineralization in which the template on which crystals will grow undergoes a structural organization such that the crystal growth is thermodynamically favored. This is the first order molecular construction of organic supramolecular system which provides a base for the growth of biominerals. Interfacial molecular recognition is the stage in which the nucleation of the biomineralization takes place. This nucleation center is in the surface of the supramolecular assembly. It is generally considered that the assembly of mineral nuclei is governed by the electrostatic, structural and stereochemical complementarities at the organic inorganic interface. After the formation of the nucleation center, crystal growth on it leads to a distinct

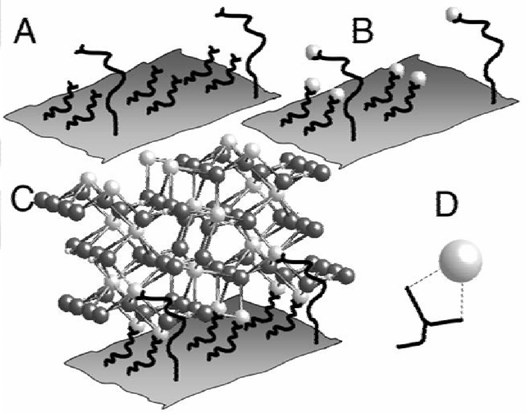

Figure 1.2. A. Pre-organization of organic matrix, B. Molecular recognition, C. Epitaxial growth at the matrix interface and D. Interaction at the organic–inorganic interface.

biomineral. Vectorial regulation is this stage in which the actual growth of the biominerals takes place. After the growth of a biomineral, it is utilized by the body for various functions. This is done in the process of cellular processing. In this stage of bimineralization, a variety of constructional processes are involved leading to the production of the biominerals of higher ordered architecture with elaborate ultra and micro structural properties. It is at this level of biomineralization, there lays a large disparity between synthetic and naturally occurring ways of biomineralization. Lowenstam [1.4] has defined two modes of biomineralization: **(1) Biologically Induced Mineralization (BIM)** which is enacted extracellularly or on the cell surface by many algae and bacterial species [1.7]and organic-matrix mediated mineralization performed by many animals which is now commonly known as **(2) Biologically Controlled Mineralization (BCM)**.

(1) Biologically induced mineralization (BIM)

The secondary precipitation of minerals that occurs as a result of interactions between biological activity and the environment is termed "biologically induced" mineralization. In this situation, cell surfaces often act as causative agents for nucleation and subsequent mineral growth. The biological system has little control over the type and habit of minerals deposited, although the metabolic processes employed by the organism within its particular redox environment mediate pH, pCO_2 and the compositions of secretion products [1.8]. These chemical conditions favor particular mineral types in an indirect way (Figure 1.3).

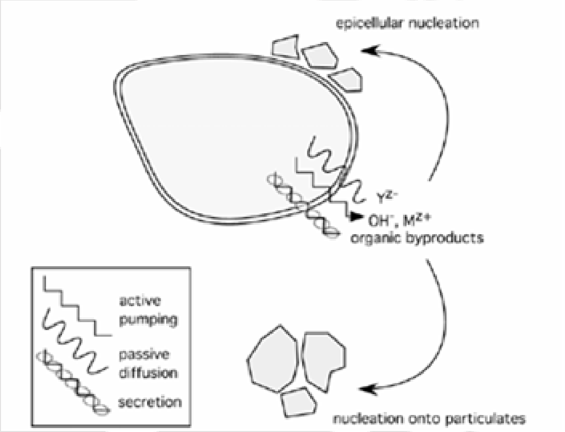

Figure 1.3. Schematic of biologically induced mineralization.

(2) Biologically controlled mineralization (BCM)

In "biologically controlled" mineralization, the organism uses cellular activities to direct the nucleation, growth, morphology and final location of the mineral that is deposited. While the degree of control varies across species, almost all controlled mineralization processes occur in an isolated environment. The results can be remarkably sophisticated, species-specific products that give the organism specialized biological functions. BCM processes can be described as occurring extra-, inter- or intracellularly. In extracellular mineralization (Figure 1.4), the cell produces a macromolecular matrix outside the cell in

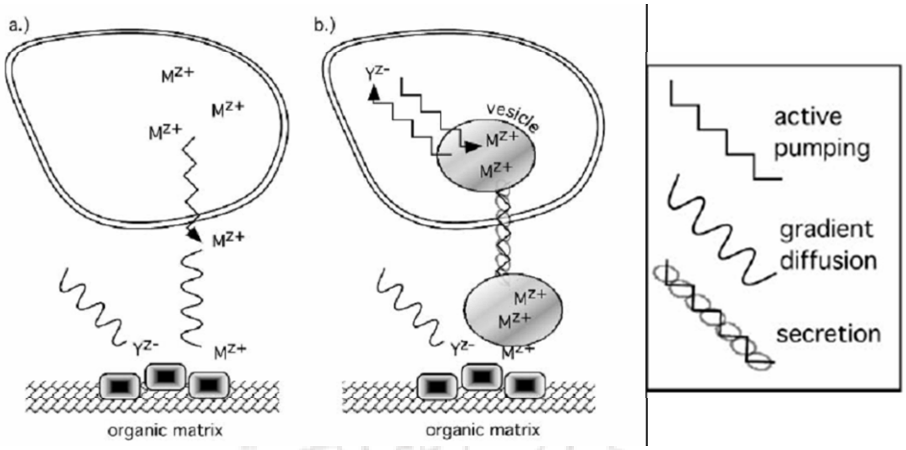

Figure 1.4. Illustrations of biologically controlled extracellular mineralization showing that this process is distinguished by nucleation outside of the cell. (a) Cations are pumped across the cell membrane and move by passive diffusion through extracellular fluids to the site of mineralization. (b) Cations are concentrated intracellularly as aqueous ions into a vesicle that is subsequently secreted. Compartment breakdown at site of mineralization releases cations for biomineral formation.

an area that will become the site of mineralization. The term matrix refers to a group of macromolecules (*viz.* proteins, polysaccharides, glycoproteins) that assemble to form a 3D framework. Biologically controlled intercellular mineralization type of mineralization is not widespread. It typically occurs in single-celled organisms that exist as a community. The epidermis of the individual organisms serves as the primary means of isolating the site of mineralization [1.9]. As shown in Figure 1.5, the epithelial substrate reproducibly directs the nucleation and growth of specific biomineral phases over large areas of cell surfaces. Mineralization between cells can become as extensive as to completely fill the intercellular spaces, thus forming a type of exoskeleton. Biologically controlled intracellular mineralization (Figure 1.6) can occur within specialized vesicles or vacuoles that direct the nucleation of biominerals within the cell.

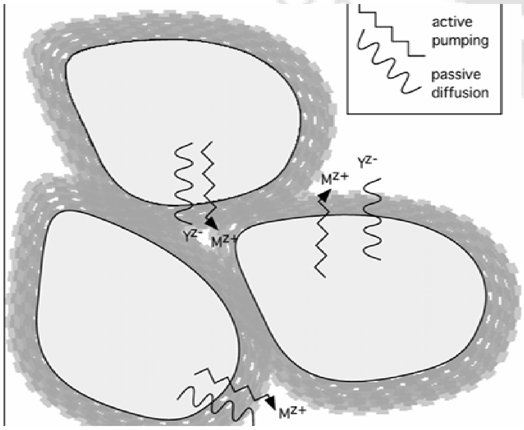

Figure 1.5. In biologically controlled intercellular mineralization, the epithelial surfaces of cells are used as the organic substrate for nucleation and growth with a preferred orientation. Cations are pumped out of the cell and fluid compositions are regulated to maintain control over the biomineral type and extent of growth.

This is a widespread strategy. In this situation, the cell has a high degree of control upon the concentrations of cation and anion biomineral constituents in an environment where an organic matrix may also be active as a nucleating template. Eukaryotic biominerals often show complex hierarchical structure from the nanometer to the macroscopic scale. This structure confers mechanical strength and toughness: despite being highly mineralized, with the organic component constituting not more than a few percent of the composite material, the fracture toughness exceeds that of single crystals of the pure mineral by two to three orders of magnitude [1.8]. The remarkable material properties of bones and teeth results from the activities of proteins that function at the organic-inorganic interface. At this interface, in diverse eukaryotic and prokaryotic biomineralization, there is frequently a carboxyl group. Acidic amino acids or polysaccharides with excess carboxyl groups are the most common and most effective cation-binding chemical species that any organism can assemble to bind mineral precursors and initiate templation. Figure 1.6. shows that nucleation occurs within the cell in a specialized vesicle. a) Biomineral is nucleated (1) within a compartment in the intracellular environment. These growth units may be assembled intracellularly (2) for subsequent secretion (3a) or secreted as an individual unit (3b) for subsequent organization into a higher order growth structures as a massive or organic-mineral composite. b.) In a less frequently used type of mineralization, the biomineral unit remains within the cell (1) as a single growth unit or is organized intracellularly (2) into a higher order structure. As indicated by Table 1.1, calcium is the cation of choice for most organisms. The calcium-bearing minerals comprise about 50% of known biominerals [1.4]. This is because calcium fulfills many fundamental functions in cellular metabolism This dominance of calcium-bearing minerals is what led to the widespread usage of the term calcification.

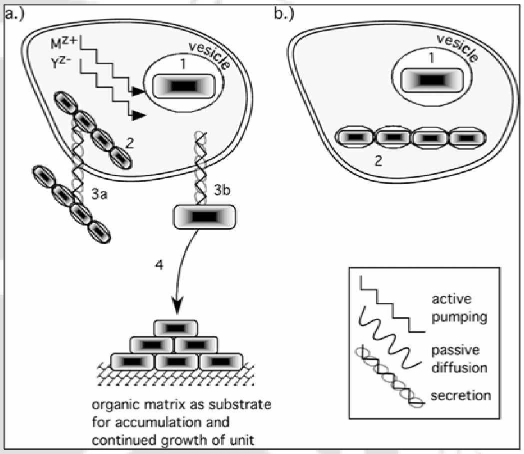

Figure 1.6. Schematics of biologically controlled intracellular mineralization.

1.2 Low-Molecular-Weight Growth Modifier

For last two decades extensive studies have been done on the biomineralization of calcium and barium based minerals [1.8–1.10]. From these studies now it has been established that the biominerals grow on the organic template containing oxygen and nitrogen donor atoms. These structures are stabilized through ion-ion, hydrophobic-hydrophilic interactions etc. which in turn controls the structure and morphology of the crystals. In comparison to the other, additives possessing hard donor groups like carboxylic acid are believed to have greater influence on the nucleation, orientation and growth habit of calcium and barium based minerals. Since these groups can bind to oxophillic hard alkaline earth metals *e.g.* Ca, Ba ions [1.11]. In recent years, mechanism of biomineralization and biomimetic material synthesis has been intensely studied by using various low-molecular-weight soluble, ionic or particle-based additives *e.g.* Mg^{2+} ion, Zn^{2+} ion, mercaptobenzoic acid capped gold particles [1.12], citric/malic acid [1.13], calcium complexing substances [1.14], *i.e.* diethylenetriaminepentaacetic acid (DTPA), ethylenediaminetetraacetic acid (EDTA), pyromellitic acid (PMA), amino-carboxyl-chelating-agent, 1,2-bis (4-aminophenoxy) ethane-tertraacetic acid (4-BAPTA) [1.15], functionalized and non-functionalized α, ω- dicarboxylates have been studied [1.16]. Various acidic amino acids *e.g.* generation of chiral calcite morphologies in the presence of aspartic acid (Asp) enantiomers [1.17] has also been investigated. Manoli *et. al.* has reported that alcohols like ethanol, isopropanol or diethylene glycol also influence the $CaCO_3$ morphology through $CaCO_3$ polymorph selection by preventing the transformation of complex shaped vaterite aggregates to calcite [1.18]. It is proposed that additives have two different functions in mineralization processes [1.19]: (a) they could inhibit crystal growth by binding to the growth sites of the crystal and (b) they could act as a heterogeneous nucleator controlling and stabilizing the precipitating polymorph.

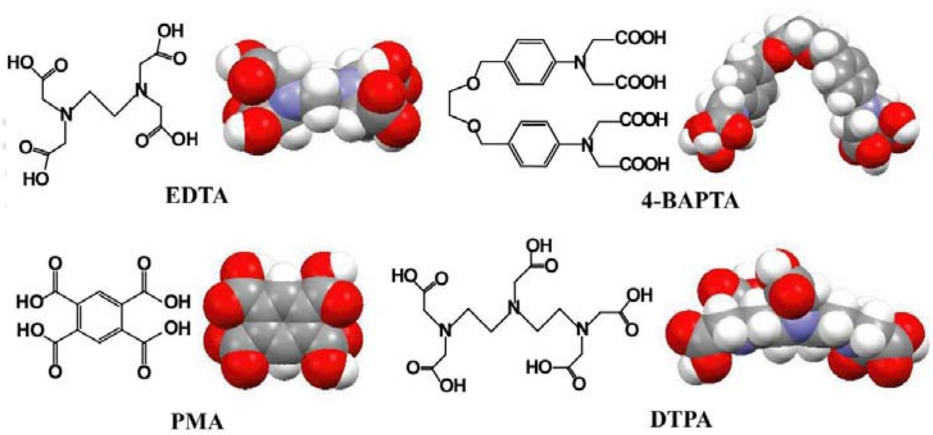

Scheme 1.1. Molecular structure and 3D-spaced filled model of few low-molecular-weight growth modifiers.

Table 1.1. The names and chemical compositions of minerals produced by biologically induced and controlled mineralization processes in order of their anions.

Anions	**Name**	**Chemical formula**
Carbonate	Calcite	$CaCO_3$
	Aragonite	$CaCO_3$
	Vaterite	$CaCO_3$
	Hydrocerussite	$Pb_3(CO_3)_2(OH)_2$
	Monohydrocalcite	$CaCO_3.\ H_2O$
	Protodolomite	$CaMg(CO_3)_2$
Fluoride	Fluorite	CaF_2
	Hieratite	K_2SiF_6
Oxalate	Glushinskite	$MgC_2O_4.\ 4H_2O$
	Weddelite	$CaC_2O_4.\ (2 + x)H_2O\ (\ x < 0.5\ )$
	Whewellite	$CaC_2O_4.\ H_2O$
Oxide	Magnetite	$Fe^{2+}Fe_2^{3+}O_4$
	Amorphous Iron Oxide	Fe_2O_3
	Birnessite	$Na_4\ Mn_{14}O_{27}.\ 9H_2O$
	Ferrihydrite	$5\ Fe_2O_3.\ 9H_2O$
	Goethite	α-FeO(OH)
	Lepidocrocite	γ- FeO(OH)
Phosphate	Brushite	$Ca(HPO_4)_2.\ 2H_2O$
	Carbonate-hydroxylapatite	$Ca_5(PO_4,CO_3)_3(OH)$
	Fluoroapatite (francolite)	$Ca_5(PO_4)_3F$
	Hydroxylapatite	$Ca_5(PO_4)_3(OH)$
	Octacalcium phosphate	$Ca_8H_2(PO_4)_6.\ 5H_2O$
	Struvite	$Mg(NH_4)PO_4.\ 6H_2O$
	Vivianite	$Fe_3^{2+}(PO_4)_2.\ 8H_2O$
	Whitlockite	$Ca_{18}\ H_2(Mg,\ Fe)_2^{2+}(PO_4)_{14}$
Silicate	Hieratite	K_2SiF_6
	Opal	$SiO_2.\ nH_2O$
Sulfates	Barite	$BaSO_4$
	Celestite	$SrSO_4$
	Gypsum	$CaSO_4.\ 2H_2O$
	Jarosite	$K\ Fe_3^{3+}(SO_4)_2\ (OH)_6$
Sulfides	Galena	PbS
	Greigite	$Fe^{2+}Fe_2^{3+}S_4$
	Hydrotroilite	$FeS.\ nH_2O$
	Mackinawite	$(Fe,\ Ni)_8\ S_8$
	Pyrite	FeS_2
	Sphalerite	ZnS
	Wurtzite	ZnS

It is well known that the shape of inorganic crystals is normally related to the intrinsic unit cell structure and the crystal shape is often the outside embodiment of the unit-cell replication and amplification. According to the thermodynamic viewpoint, the crystal morphology depends on the differences of the crystal faces in surface energy and external growth environment [1.20]. The equilibrium morphology of a crystal is defined by the minimum energy resulting from the sum of the products of the surface area of all exposed faces and the relative surface energies. The fast growing faces have high surface energies and they will vanish in the final morphology and vice versa. Although this purely thermodynamic treatment cannot always predict the crystal morphology, as crystallization and the resulting morphology often also rely on kinetic effects as well as on defect structures, it is the basis for the explanation of additive mediated crystal morphology changes in biomimetic mineralization. The surface energy of a crystal face can be lowered by the adsorption of an additive. Therefore, the shape of crystals can be affected by various factors, *i.e.* inorganic ions or organic additives [1.21]. The anisotropic growth of the particles can be explained by the specific adsorption of ions or organic additives to particular faces, therefore inhibiting the growth of these faces by lowering their surface energy. Only the additives that can adsorb on special crystal faces can change the surface energies of the different crystal faces and change the crystallization process and the final morphologies. Small molecular additives such as small inorganic ions, small molecular organic species, and solvents have been found to exert strong influences on the shape of inorganic crystals when they selectively adsorb on special faces of the crystals [1.22].

Colfen *et. al.* has reported that the kinetic crystallization control is based predominantly on the modification of the activation-energy barriers of nucleation, growth, and phase transformation [1.23] (Figure 1.7). In such cases, crystallization often proceeds by a sequential process involving structural and compositional modifications of amorphous precursors and crystalline intermediates through a kinetic effective pathway, rather than a single-step thermodynamic pathway [1.23, 1.24]. How far these phase transformations proceed along a series of increasingly stable intermediates depends on the solubility of the minerals and on the free energies of activation of their inter-conversions, all of which are strongly influenced by additives [1.25]. The corresponding changes in composition and structure usually occur by dissolution–recrystallization processes closely associated with the surface and/or the interior of preformed particles. Kinetically driven crystallization often involves an initial amorphous phase that may be non-stoichiometric, hydrated, and susceptible to rapid phase transformation. Amorphous calcium carbonate (ACC) for instance is highly soluble and rapidly transforms to calcite, vaterite, or aragonite unless kinetically stabilized. In biomineralization, this stabilization is achieved by ions such as Mg^{2+} and PO_4, or by enclosing the amorphous phase in an impermeable sheath of organic macromolecules, such as polysaccharides [1.26] or mixtures of polysaccharides and proteins rich in glutamic acid, threonine, and serine [1.27]. Kinetic control of crystallization can be achieved by modifying the interactions of nuclei and developing crystals with solid surfaces and soluble molecules [1.28]. Such processes influence the structure and composition of the nuclei, particle size, texture, habit and aggregation, and stability of intermediate phases.

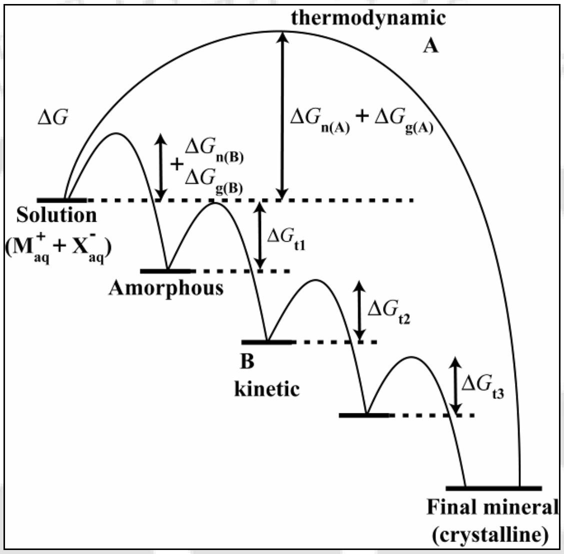

Figure 1.7. Crystallization pathways under thermodynamic and kinetic control. Whether a system follows a one-step route to the final mineral phase (pathway A) or proceeds by sequential precipitation (pathway B), depends on the free energy of activation (ΔG) associated with nucleation (n), growth (g), and phase transformation (t). Amorphous phases are common under kinetic conditions.

1.3 High-Molecular-Weight Matrix

Nature has evolved sophisticated strategies for engineering hard tissues through the interaction of proteins and, ultimately, cells with inorganic mineral phases. Bone and dentin biomineralization are well-regulated processes mediated by extracellular matrix proteins. It is widely believed that specific matrix proteins in these tissues modulate nucleation of apatite nanoparticles and their growth into micrometer-sized crystals via molecular recognition at the protein-mineral interface [1.29]. Although the exact mechanism remains unknown, it is postulated that kinetic control of biomineral crystallization is achieved by interactions between mineral nuclei and soluble or immobilized acidic proteins *e.g.* Dentin matrix protein 1 (DMP1) is an acidic non-collagenous phosphoprotein known to be present in the mineralized matrix of both dentin and bone [1.30]. Similarly Ameloblastin (AMBN) act as a tooth-specific enamel matrix protein secreted only by ameloblast cells [1.31] and also expressed during the development of mesenchymal dental hard tissue [1.32], during trauma-induced reparative dentin formation [1.33], and during the early stages of craniofacial bone formation [1.34]. The function of AMBN protein is unclear, but it has been implicated in enamel biomineralization [1.35] and in interactions between the ameloblasts and the enamel extracellular matrix [1.36]. Ovocleidin-17 (OC17) from *Gallus gallus* is one of the best candidates to control and regulate the deposition of calcium carbonate in the calcified eggshell layer. A study of *in vivo* $CaCO_3$ biominerals of Mollusk shell has revealed the fact that Ca^{2+} binds to polyanionic sites [1.8c]. These protein contains a special kind of sequence that mainly contains L-Aspartic acid and L-Glutamic acid residues [1.10e]. As the α-carboxylic function is involved in peptide bond formation, it is the side chain carboxylic group of Asp and Glu amino acids that forms the base for the nucleation of these biominerals. Depending on the amino acids present at the nucleation center biominerals grow with different morphology [1.10e] that performs various physiological roles. Proteins secreted by living organisms accumulate or induce the formation and precipitation of various inorganic compounds such as phosphates, carbonates and silicates [1.37]. Although biominerals exist in various forms and functions, they are all formed according to the same underlying principle [1.38]. These minerals are formed in the matrix of the bio-macromolecules like proteins, polysaccharides and lipids. Most biominerals are organized hierarchally and ordered at many length scales starting from nano- to micro-scale [1.39] and often have profound physical characteristics. A wide range of *in vitro* biomineralization [1.40] and macroscopic templates as a confined reaction environments for precipitation exist for organizing inorganic materials [1.41]. This includes soluble biopolymers *e.g.* dextran [1.42], polyamino acids *e.g.* poly-α, L-aspartate [1.13], synthetic polymers *e.g.* dendrimers [1.43], double-hydrophilic block copolymer (DHBC) *e.g.* poly(propylene imine) dendrimer modified with long chain alkyl chains [1.44] (Fig. 1.8), poly(ethylene glycol)-block-poly(methacrylic acid) block copolymer (PEG-b-PMAA) [1.45], poly (amido-amine) (PAMAM), Biopolymer gels [1.46] *e.g.* Gelatine, poly(acrylamide) hydrogel etc. as insoluble matrix and some surfactant based systems *e.g.* Langmuir Monolayers of octadecylamine (ODA) [1.47], (CTAB)/*n*-butanol/hexadecane/water microemulsions [1.48, 1.49].

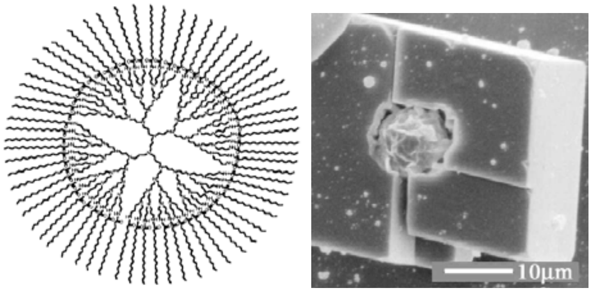

Figure 1.8. Schematic diagram of poly(propylene imine) dendrimer modified with long chain alkyl chains: SEM micrograph of the $CaCO_3$ crystallization assay with octadecylamine doped poly(propylene imine) dendrimers as additive after 14 days [1.44].

1.4 Biomimetic Materials Synthesis

Now a day, a lot of importance has been gained by biomimetic material synthesis. The four stages of biomineralization can be used as biological archetype to design some ways to mimic the naturally occurring biominerals by synthesizing them at the laboratories.

Table 1.2. Functions and Correlation of Biological and Biomimetic principles

Biological Principle	Biomimetic Principle	Function
Supramolecular Preorganization	Host-Guest Chemistry	Delineated reaction sites
Interfacial Molecular recognition	Molecular Blueprinting	Site-specific nucleation
Vectorial Regulation	Crystal Engineering	Crystal growth and termination
Cellular Processing	Molecular Tectonics	Higher order architecture

As shown in Table 1.2, the four biological archetypes can be translated into principles that serve as guidelines for laboratory development. First, the preorganization of supramolecular assemblies in biomineralization can be considered as archetype of a to host-guest approach to the nanoscale synthesis of composites. Second, the concept of interfacial molecular recognition suggests that inorganic material synthesis can be regulated through molecular blueprinting with organic substrates. Third, the crystal engineering of materials can be viewed from the perspective of vectorial regulation with concomitant concepts such as templating, directed growth, and microstructural fabrication. Finally, the paradigm of cellular processing of biominerals can be used to develop methods to the controlled architectural assembly of preformed particles or crystals with tailored properties – an approach that extends all the way from molecule to crystal techonics [1.2]. Scheme 1.2 schematizes the connection between these strategies with materials properties and processes for the fabrication of inorganic materials and composites. Three main thrusts in biomimetic material chemistry are currently being developed within the context of biomineralization (Scheme 1.3). First, the specific chemical and structural properties of biomolecules involved in biomineralization processes can be utilized in synthetic reactions *e.g.*: nanoscale synthesis of ferritin, shell protein in the control of the texture and morphology of calcite crystals [1.50], polysaccharides as dispersants in ceramic processing [1.51], and small biopeptides in the formation of CdS clusters [1.52]. Second, living organisms such as bacterial culture [1.53] or red abalone [1.54] have been utilized as intact biosystems for the fabrication of highly ordered composites.

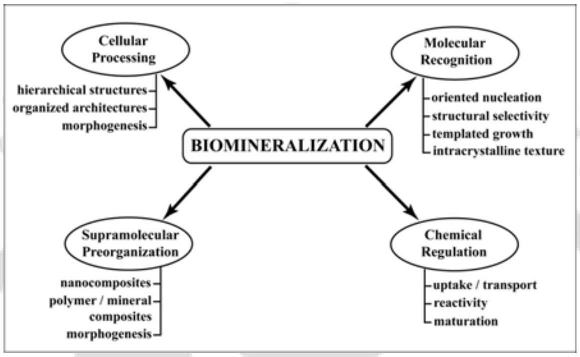

Scheme 1.2. Constructional processes in biomimetic material chemistry.

The third possibility is the use of bioconcepts as source of inspiration for new idea in the synthesis of inorganic materials exhibiting uniform particle size, polymorph selectivity, tailored morphology, oriented nucleation and organized assembly [1.2].

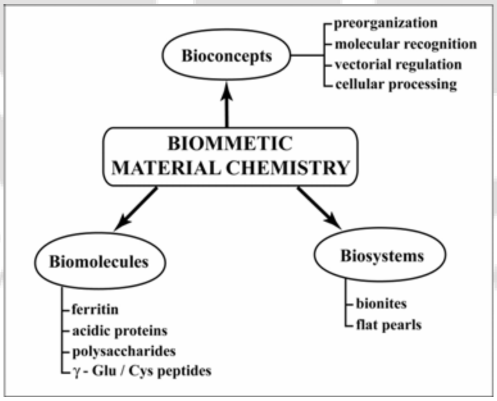

Scheme 1.3. Areas of biomimetic material chemistry with regard to biomineralization.

1.5 Precursor Synthesis and application of inorganic minerals

The fabrication of assemblies of perfect nano to micrometer scale crystallites identically replicated in unlimited quantities is the ultimate challenge of materials research with outstanding fundamental and potential technological prospects [1.55]. Precursor synthesis is one of the well established solid-state methods to prepare inorganic mineral. Crystalline precursor complexes transform to other known crystalline mineral phases at higher temperatures *via* calcination-reconstruction method. Precursor-complex controlled mineral synthesis is a versatile tool toward inorganic mineral crystal morphogenesis and understanding of the self-assembly of solid-state superstructures in the formation of inorganic minerals. Among the various inorganic materials, metal oxides have attracted increasing technological and industrial interest. They are widely used in ceramics, electronics, optics, chemical and pharmaceutical industries and in the production of magnetic tapes.

Wide band gap II–VI smart semiconductor ZnO is very important in the fields of optical device technology *viz.* visual display, high-density optical memory, transparent conductors, solid-state laser devices, solar cell [1.56]. A narrow band gap *p*-type semiconductor CuO is an important material in catalysis, batteries, magnetic storage media, solar energy conversion, gas sensing, field emission, high-temperature superconductivity and semi-conducting anti-ferromagnetism [1.57]. NiO is a stable wide band gap transparent *p*-type semi-conducting material, which is well known as an electrode material for super-capacitor, alkaline battery and electro-catalysis [1.58]. Co_3O_4 demonstrate high lithium storage capacity and good cycle-ability. The ferric hydrous oxides are used as pigments, catalysts, coatings, fillers and in the production of magnetic tapes and in magnetic materials technology [1.59]. The polymorphs of Mn_2O_3 have been proposed as cheap, environmental-friendly catalysts for carbon monoxide and organic pollutants oxidation, nitrogen oxide decomposition and also used to produce soft magnetic materials such as manganese zinc ferrite [1.60]. Chromium oxide has been used as protective coatings in digital magnetic recorders [1.61], as electrodes in Li solid-state batteries [1.62], as resistant coatings on wires and as thermal barrier layers [1.63]. A number of different fabrication techniques were reported for these transition metal oxides [1.60,1.64]. Macroporous materials are of particular interest for applications such as separation and purification processes, supported catalysis, drug delivery, heavy metal trapping, smart fillers, etc. There are two main synthetic approaches that generally are used for the synthesis of macroporous materials [1.65]. In the first method, structure directing agents, typically in the form of supramolecular surfactant aggregates, are used as porogens, and a porous material is obtained after removal of the surfactant by combustion or by ion-exchange. In the second method, porous solid molds are used as sacrificial templates. Inorganic condensation reaction occurs in those pores or on the outer surface of the mold, and subsequently the mold is selectively removed in order to generate the porosity.

Spinel of the type $M^{2+}M_2^{3+}O_4$ attract the research interest because of their versatile practical applications [1.66]. In the case of M^{3+} = Fe, the resulting cubic spinel structured ferrites having a general chemical composition of $MO{\cdot}Fe_2O_3$ (M=Fe, Mn, Co, Ni, Zn) are among the most frequently used systems to understand fundamental aspects of nanomagnetism [1.67] and have been widely applied as magnetic materials. Spinel compounds have also been proved as important oxides in gas sensors, and have been investigated for the detection of reducing gases [1.68]. They have also been used in high-density magnetic recording, microwave devices and magnetic fluids [1.69]. There is a strong interest in the potential utilization of magnetic nanoparticles in biomedical and diagnostic applications, including magnetic resonance imaging (MRI) as a contrast enhancement agents, hyperthermia tumor treatment, and separation of DNA, cell separation and site-specific gene and drug delivery [1.70]. Soft magneto-elastic materials such as $ZnFe_2O_4$ are also extensively used as the key components in many industries such as aerospace, nuclear power plant, telecommunication etc. for controlling vibrations [1.71]. Copper ferrites are very important for theoretical understanding in all of spinel ferrites. Polycrystalline nickel zinc ferrite has variety of applications in microwave control components such as circulators, isolators, and phase shifters [1.70b]. $CoFe_2O_4$ with its high coercivity (Hc) and moderate saturation magnetization (Ms) as well as remarkable chemical stability and mechanical hardness, makes it a good candidate for the future magneto-optical (MO) recording material [1.72]. The substance $MnFe_2O_4$, one of the most important magnetic materials, has been widely used in electronic applications [1.73] and contrast enhancement agents in magnetic resonance imaging (MRI) technology [1.74], in addition to recording media. Various preparation methods have been developed to obtain ferrites, such as hydrothermal synthesis [1.75], coprecipitation [1.76], sol–gel [1.77], spray drying [1.71a], solid-state, microemulsion processes [1.71b, 1.78], and mechanical alloying [1.79].

In recent years, the design, synthesis, and application of nano to microsized biocompatible magnetic materials has opened up new perspectives of biological and biomedical applications. Currently, there are few magnetic materials used as magnetic micro and nanocarriers in biomedical and biotechnological applications. Fe-oxide and especially Magnetite, Fe_3O_4 is an extensively studied material due to its several interesting properties like a great chemical stability, biocompatibility and the heating ability in presence of a field, which made it an interesting candidate for hyperthermia treatment [1.80] and are mostly used either as a background material for magnetic fluids or as magnetic particles, covered with a thin layer of polymer or other biocompatible materials [1.81]. Amorphous magnetic materials, both as micro and nanoparticles, could be successfully used as magnetic carriers because of their specific magnetic properties [1.82]. They are also used in cell separation and magnetohyperthermia of tumor cells. In particular, biocompatible magnetic fluids (BMFs) have played a key role as a material basis for magnetic-active drug delivery systems. BMFs are composed of magnetic nano to microparticles surface-coated with organic molecules and dispersed as a stable colloid in physiological medium [1.83]. Many methods for the synthesis have been developed like sol–gel process, microemulsion, sputtering, thermal decomposition [1.84] etc. With this variety of method has been obtained particles with different morphologies such as spheres, rods, wires and tubes [1.85].

References:

[1.1] J. W. Steed, J. L. Atwood, Supramolecular Chemistry John Willey & Sons Ltd. (2000) 450.

[1.2] (a) S. Mann, Biomimetic Materials Chemistry VCH Publishers (1996), pp 1, (b) E. Baeuerlein Biomineralization Wiley-VCH (2000). (c) M. Frédéric, L. Gilles, C. R. Palevol 3 (2004) 469.

[1.3] A. Boskey, J. Cell. Biochem., Suppl. 30-31 (1998) 83.

[1.4] (a) H. A. Lowenstam, S. Weiner, On Biomineralization, Oxford University Press, New York (1989), (b) H. A. Lowenstam, Science 211 (1981) 1126, (c) K. Simkiss, D. Allemand, In Biomineralization, 93rd ed., Musee Oceanographique, Monaco (1993).

[1.5] G. Krampitz, G. Graser, Angew. Chem. 27 (1988) 1145.

[1.6] (a) J. Aizenberg, S. Albeck, S. Weiner, L. Addadi, J. Crystal Growth 142 (1994) 156, (b) J. D. Hartgerink, E. Beniash, S. I. Stupp, Science 294 (2001) 1684.

[1.7] K. O. Konhauser, FEMS Microbiology Reviews 20 (1997) 315.

[1.8] (a) T. McConnaughey, Geochim Cosmochim Acta 53 (1989) 151, (b) D. Fortin, F. G. Ferris, T. J. Beveridge, Rev Mineral 35 (1997) 161, (c) R. B. Frankel, D. A. Bazylinski, Rev Mineral Geochem 54 (2003) 95.

[1.9] S. Mann, Biomineralization: Principles and Concepts in Bioinorganic Materials Chemistry. Oxford University Press, New York (2001).

[1.10] (a) J. Donners, B. R. Heywood, E. W. Meijer, R. J. M. Nolte, C. Roman, A. P. H. J. Schenning, N. A. J. M. Sommerdijk, Chem. Commun. (2000) 1937, (b) J. Yu, X. W. Wei, J. Sun, Y. H. Ni, G. C. Zhao, Y. Ye, Chem. Lett. 33 (2004) 1384, (c) J. Yu, J. M. Yu, L. Zhang, L. Wu, Chem. Commun. (2004) 2414, (d) C. M. Niemeyer, C. A. Mirkin, Nanobiotechnology WILEY-VCH Verlag GmbH & Co. (2004) 278, (e) S. E. Aβmann, M. Viertelhaus, A. Heiβ, K. A. Hoetzer, J. Felsche, J. Inorg. Biochem. 91 (2002) 481.

[1.11] E. Dalas, P. Klepetsanis, P. G. Koutsoukos, Langmuir 15 (1999) 8322.

[1.12] I. Lee, S. W. Han, H. J. Choi, K. Kim, Adv Mater 13 (2001) 1617.

[1.13] F. C. Meldrum, J Cryst Growth 231 (2001) 544.

[1.14] K. J. Westin, A. C. Rasmuson, J. Coll. Inter. Sci. 282 (2005) 359.

[1.15] A. J. Xie, Z. W. Yuan, Y. Shen, J. Cryst. Growth 276 (2005) 265.

[1.16] S. Mann, J. M. Didymus, N. P. Sanderson, B. R. Heywood, E. J. A. Samper, J. Chem. Soc. Faraday T rans. 86 (1990) 1873.

[1.17] C. A. Orme, A. Noy, A. Wierzbicki, M. T. McBride, M. Grantham, H. H. Teng, et al. Nature 411 (2001) 775.

[1.18] F. Manoli, E. Dalas, J Cryst Growth 218 (2000) 359.

[1.19] F. Manoli, J. Kanakis, P. Malkaj, E. Dalas, J. Crystal Growth 236 (2002) 363.

[1.20] G. Wulff, Z. Kristallogr. 34 (1901) 449.

[1.21] A. W. Xu, Y. Ma, H. Colfen, J. Mater. Chem. 17 (2007) 415.

[1.22] J. H. Adair, E. Suvaci, Curr. Opin. Colloid Interface Sci. 5 (2000) 160.

[1.23] H. Colfen and S. Mann, Angew. Chem., Int. Ed. 42 (2003) 2350.

[1.24] (a) J. Rieger, E. Hadicke, I. U. Rau, D. Boeckh, Tenside Surfactants Deterg. 34 (1997) 430, (b) O. Sohnel, J. W. Mullin, J. Cryst. Growth 60 (1982) 239.

[1.25] S. Mann, Angew. Chem., Int. Ed. 39 (2000) 3392.

[1.26] H. J. Arnott, M. Omori, N. Watabe, Mechanisms of Biomineralization in Animals and Plants, Tokai University Press, Tokyo, (1980).

[1.27] (a) J. Aizenberg, G. Lambert, L. Addadi, S. Weiner, Adv. Mater. 8 (1996) 222, (b) J. Aizenberg, G. Lambert, S. Weiner, L. Addadi, J. Am. Chem. Soc. 124 (2002) 32.

[1.28] A. Tsortos, S. Ohki, A. Zieba, R. E. Baier, G. H. Nancollas, J. Colloid Interface Sci. 177 (1996) 257.

[1.29] G. He, S. Gajjeraman, D. Schultz, D. Cookson, C. Qin, W. T. Butler, J. Hao, A. George, Biochemistry 44 (2005) 16140.

[1.30] (a) A. George, B. Sabsay, P. A. Simonian, A. Veis, J. Biol. Chem. 268 (1993)12624, (b) C. Qin, S. Xiaoling, J. Jarrod, A. George, A. Ramachandran, P. G. Jeffrey, T. B. William, Eur. J. Oral Sci. 109 (2001) 133, (c) A. George, R. Silberstein, A. Veis, Connect. Tissue Res. 33 (1995) 67.

[1.31] (a) P. H. Krebsbach, S. K. Lee, Y. Matsuki, C. A. Kozak, R. M. Yamada, Y. Yamada, J. Biol. Chem. 271 (1996) 4431, (b) R. Cerny, I. Slaby, L. Hammarstrom, T. Wurtz, J. Bone Mineral Res. 11 (1996) 883.

[1.32] C. D. Fong, R. Cerny, L. Hammarstrom, I. Slaby, Eur. J. Oral Sci. 106 (1998) 324.

[1.33] A. Spahr, S. P. Lyngstadaas, I. Slaby, B. Haller, C. Boeckh, F. Tsoulfidou, L. Hammarstroem, Clin. Oral. Invest. 6 (2002) 51.

[1.34] A. Spahr, S. P. Lyngstadaas, I. Slaby, G. Pezeshki, Eur. J. Oral Sci. 114 (2006) 504.

[1.35] (a) T. Uchida, C. Murakami, N. Dohi, K. Wakida, T. Satoda, J. Histochem. Cytochem. 45 (1997) 1329, (b) S. J. Brookes, J. Kirkham, R. C. Shore, S. R. Wood, I. Slaby, C. Robinson, Arch. Oral Biol. 46 (2001) 201.

[1.36] (a) M. L. Paine, H. J. Wang, W. Luo, P. H. Krebsbach, M. L. Snead, J. Biol. Chem. 278 (2003) 19447, (b) S. Fukumoto, T. Kiba, B. Hall, N. Iehara, T. Nakamura, G. Longenecker, P. H. Krebsbach, A. Nanci, A. B. Kulkarni, Y. Yamada, J. Cell Biol. 167 (2004) 973.

[1.37] S. Stocks-Fischer, J. K. Galinat, S. S. Bang, Soil Biol Biochem 31 (1999) 1563.

[1.38] G. Krampitz, G. Graser, Angew. Chem. Int. Ed. Engl 27 (1988) 1145.

[1.39] S. Mann, Nature 365 (1993) 499.

[1.40] (a) L. Addadi, S. Weiner, Angew. Chem. Int. Ed. 31 (1992) 153, (b) J. Aizenberg, A. Tkachenko, S. Weiner, L. Addadi, G. Hendler, Nature 412 (2001) 819, (c) S. Mann, Biomineralization: Principles and

Concepts in Bioinorganic Materials Chemistry, Oxford University Press: New York, (2002), (d) S. R. Whaley, D. S. English, E. L. Hu, P. F. Barbara, A. M. Belcher, Nature 405 (2000) 665.

[1.41] (a) G. S. Attard, P. N. Bartlett, N. R. B. Coleman, J. M. Elliott, J. R. Owen, J. H. Wang, Science 278 (1997) 838, (b) C. J. Brinker, Curr. Opin. Colloid Interface Sci 3 (1998) 166, (c) C. T. Kresge, M. E. Leonowicz, W. J. Roth, J. C. Vartuli, J. S. Beck, Nature 359 (1992) 710, (d) P. V. Braun, S. I. Stupp, Science 277 (1997) 1242.

[1.42] V. V. Hardikar, E. Matijevic, Colloids Surf A 186 (2001) 23.

[1.43] (a) K. Naka, Y. Tanaka, Y. Chujo, Langmuir 18 (2002) 3655, (b) M. Sedlak, H. Colfen, Macromol Chem Phys. 202 (2001) 587, (c) K. Kaluzynski, J. Pretula, G. Lapienis, M. Basko, Z. Bartczak, A. Dworak, et al. J Polym Sci Part A Polymer Chem. 39 (2001) 955, (d) L. B. Gower, D. J. Odom, J Cryst Growth 210 (2000) 719.

[1.44] F. C. Meldrum, Int. Mater. Rev. 48 (2003) 187

[1.45] H. Colfen, L. M. Qi, Progr. Colloid Polym. Sci. 117 (2001) 200.

[1.46] H. Colfen, Curr. Opin.Colloid. Inter. Sci. 8 (2003) 23.

[1.47] S. Mann, B. R. Heywood, S. Rajam, J. B. A. Walker, J. Phys., D: Appl. Phys. 24 (1991) 154.

[1.48] M. L. Rock, L. J. Tranchitella, R. S. Pilato, Colloid Polym. Sci. 275 (1997) 893.

[1.49] S. Kewalramani, G. Evmenenko, C.J. Yu, K. Kim, J. Kmetko, P. Dutta, Surface Science 591 (2005) L286.

[1.50] A. Berman, L. Addadi, S. Weiner, Nature 331 (1988) 546.

[1.51] N. Pellerin, J. T. Staley, T. Ren, G. L. Graff, D. R. Treadwell, I. A. Aksay, Mater. Res. Soc. Symp. 218 (1991) 123.

[1.52] C. T. Dameron, R. N. Reese, R. K. Mehra, A. R. Kortan, P. J. Carroll, M. L. Steigerwald, L. E. Brus, D. R. Winge, Nature 338 (1989) 596.

[1.53] N. H. Mendelson, Science 258 (1992) 1633.

[1.54] M. Fritz, A. M. Belcher, M. Radmacher, D. A. Walters, P. K. Hansma, G. D. Stucky, D. E. Morse, S. Mann, Nature 371 (1994) 49.

[1.55] H. F. Janos, Nanoparticles and Nanostructured Films, Preparation, Characterization and Applications, Wiley/VCH, Weinheim, (1998).

[1.56] (a) I. R. Cpllins, E. S. Taylor, J. Mater. Chem. 2 (1992) 1277, (b) L. Spanhel, M. A. Anderson, J. Am. Chem. Soc. 113 (1991) 2826.

[1.57] (a) M. Frietsch, F. Zudock, J. Goschnick, M. Bruns, Sensors Actuat. B 65 (2000) 379, (b) T. Maruyama, Sol. Energy Mater. Sol. Cells 56 (1998) 85, (c) J. T. Zhang, J. F. Liu, Q. Peng, X. Wang, Y. D. Li, Chem. Mater. 18 (2006) 867.

[1.58] Y. Z. Zheng, M. L. Zhang, Mater. Lett. 61 (2007) 3967.

[1.59] M. Sorescu, D. M. Tarabasanu, L. Diamandescu, Appl. Phys. Lett. 72 (1998) 2047.

[1.60] Y. Chen, Y. Zhanga, Q. Z. Yao, G. T. Zhou, S. Fu, H. Fan, J. Solid State Chem. 180 (2007) 1218.

[1.61] M. Catti, G. Sandrone, G. Valerio, R.Dovesi, J. Phys. Chem. Solids 57 (1996) 1735.

[1.62] P. Norby, A. Norlund, H. Christensen, M. Fjellvac, J. Nielsen, Solid State Chem. 94 (1991) 281.

[1.63] G. Contoux, F. Cosset, A. Celerier, J. Machet, Thin Solid Films 292 (1997) 75.

[1.64] (a) Z. P. Sun, L. Liu, L. Zhang, D. Z. Jia, Nanotechnology 17 (2006) 2266, (b) H. M. Xiao, L. Ping Zhu, X. M. Liu, S. Y. Fu, Solid State Commun. 141 (2007) 431, (c) Z. Yuan, F. Huang, C. Feng, J. Sun, Y. Zhou, Mat. Chem. and Phys. 79 (2003) 1.

[1.65] J. H. Smatt, N. Schuwer, M. Jarn, W. Lindner, M. Linden, Micropor. Mesopor Mat. (2007) doi:10.1016/j.micromeso.2007.10.003.

[1.66] (a) M. Sugimoto, J. Am. Ceram. Soc. 82 (1999) 269, (b) K. Raj, B. Moskowitz, R. Casciari, J. Magn. Magn. Mater. 149 (1995) 174.

[1.67] Z. Sun, L. Liu, D. Z. Jia , W. Pan, Sens. Actuators B 125 (2007) 144.

[1.68] A. Goldman, Modern Ferrite Technology, Van Nostrand Reinhold, New York, (1990).

[1.69] (a) B. M. Berkovsky, V. F. Medvedev, M. S. Krakov, Magnetic Fluids: Engineering Applications, Oxford University Press, Oxford, (1993), (b) S. Rana, A. Gallo, R. S. Srivastava, R. D. K. Misra, Acta Biomaterialia 3 (2007) 233.

[1.70] (a) L. Satyanarayana, K. M. Reddy, V. M. Sunkara, Mater. Chem. Phys. 82 (2003) 21, (b) J. D. Adam, S. V. Krishnaswamy, S. H. Talisa, K. C. Yoo, J. Magn. Magn. Mater. 83 (1990) 419, (c) F. X. Cheng, Z. Y. Peng, C. S. Liao, Z. G. Xu, S. Gao, C. H. Yan, D. J. Wang, J. Wang, Solid State Commun. 107 (1998) 471.

[1.71] (a) H. F. Yu, A. M. Gadalla, J. Mater. Res. 11 (1996) 663, (b) N. Moumen, P. Veillet, M. P. Pileni, J. Magn. Magn. Mater. 149 (1995) 67.

[1.72] J. G. Lee, J. Y. Park, C. S. Kim, J. Mater. Sci. 33 (1998) 3965.

[1.73] B. Gillot, Eur. Phys. J. Appl. 4 (1998) 243.

[1.74] B. Gillot, M. Laarj, S. Kacim, J. Mater. Chem. 7 (1997) 827.

[1.75] (a) M. Rozman, M. Drofenik, J. Am. Ceram. Soc. 78 (1995) 2449, (b) M. Sisk, I. Kilbride, A. J. Barker, J. Mater. Sci. Lett. 14 (1995) 153.

[1.76] (a) K. Kaneko, T. Katsura, Bull. Chem. Soc. Jpn. 52 (1979) 747, (b) Y. Tamaura, U. Rasyid, T. Katsura, J. Chem. Soc., Dalton Trans. 53 (1980) 2125.

[1.77] (a) S. G. Christoskova, M. Stoyanova, M. Georgieva, Appl. Catal. A 208 (2001) 235, (b) C. S. Kim, Y. S. Yi, K. T. Park, H. Namgung, J. G. Lee, J. Appl. Phys. 85 (1999) 5223.

[1.78] N. S. Kommareddi, M. Tata, V. T. John, G. L. McPherson, M. F. Herman, Y. S. Lee, O. J. O'Connor, J. A. Akkara, D. L. Kaplan, Chem. Mater. 8 (1996) 801.

[1.79] (a) J. Ding, T. Reynolds, W. F. Miao, P. G. McCormick, R. Street, Appl. Phys. Lett. 65 (1994) 3135, (b) J. Ding, P. G. McCormick, R. Street, J. Magn. Magn. Mater. 171 (1997) 309, (c) Y. Shi, J. Ding, X. Liu, J. Wang, J. Magn. Magn. Mater. 205 (1999) 249.

[1.80] Y. K. Sun, M. Ma, Y. Zhang, N. Gu, Colloids Surfaces A 245 (2004) 15.

[1.81] W. Moller, K. Scheuch, J. Sommer, J. Magn. Magn. Mater. 225 (2001) 8.

[1.82] (a) H. Chiriac, A. E. Moga, G. Jacob, J. Magn. Magn. Mater. 293 (2005) 28, (b) L. Han, S. Li, Y. Yang, F. Zhao, J. Huang, J. Chang, J. Magn. Magn. Mater. 313 (2007) 236.

[1.83] (a) T. Matsunaga, R. Sato, S. Kamiya, et al. J. Magn. Magn. Mater. 194 (1999) 126, (b) A. C. Tedesco, D. M. Oliveira, Z. G. M. Lacava, et al. J. Magn. Magn. Mater. 272 (2004) 2404, (c) C. Bergemann, D. M. Schulte, J. Oster, et al. J. Magn. Magn. Mater. 194 (1999) 45.

[1.84] (a) B. J. Palla, D. O. Shah, P. Garcia Casillas, J. Matutes-Aquino, J. Nanoparticle Res. 2 (1999) 215, (b) A. Lijuan, L. Zhaoqiang, L. Wei, N. Yaru, C. Zhimin, W. Yanping, Y. Bai, J. Magn. Magn. Mater 303 (2006) 127.

[1.85] (a) J. Matutes-Aquino, P. Garcıa Casillas, O. Ayala-Valenzuela, S. Garcıa-arcıa, Mater. Lett. 38 (1999) 173, (b) M. P. Ocana, M. P. Morales, P. Tartaj, N. Nunez, C. J. Serna, Nanotechnology 15 (2004) S190, (c) T. H. Wong, C. G. Mool, C. H. Garcia, Nanotechnology 18 (2007) 135705.

Chapter - 2

Biomineralization in presence of Low-Molecular-Weight growth modifier

2.1 Biomineralization in presence of Low-Molecular-Weight Poly-Carboxylate ligand derived from naturally occurring amino acids

An *in vitro* study of biomineralization provides useful information for the design of organic templates. Model systems, in which low-molecular-weight organic additives are used to study the effect of crystal growth modification on inorganic mineralization, are providing insights into the possible mechanism operating in biology. In recent years, mechanism of biomineralization and biomimetic material synthesis has been intensely studied by using various low-molecular-weight soluble, ionic or particle-based additives *e.g.* Mg^{2+} ion, Zn^{2+} ion, citric acid, malic acid [2.1], soluble biopolymers *e.g.* dextran [2.2], synthetic polymers *e.g.* dendrimers [2.3] and also various proteins [2.4]. It is proposed that additives have two different functions in mineralization processes [2.5]: (a) they could inhibit crystal growth by binding to the growth sites of the crystal and (b) they could act as a heterogeneous nucleator controlling and stabilizing the precipitating polymorph. In comparison to the other, additives possessing hard donor groups like carboxylic acid are believed to have greater influence on the nucleation, orientation and growth habit of $CaCO_3$. Since these groups can bind to oxophillic hard calcium ions in solution efficiently [2.6]. Low-molecular-weight chiral poly-carboxylate ligands derived from naturally occurring L-α-amino acids have been used as model systems to study the effect of molecular level aggregation as well as coordination behavior on crystal growth modification. The idea behind this work is that, from various *in vitro* and *in vivo* studies on the biomineralization of calcium minerals as mentioned in the chapter-1, now it has been established that they grow on the proteins or acidic polypeptides containing a special kind of sequence that mainly contains L-Aspartic acid and L-Glutamic acid residues [2.7]. Depending on the amino acids present at the nucleation center biominerals grow with different morphology. As in the literature it is already reported *in vitro* biomineralization of calcium minerals by using amino acid as a growth modifier [2.8], here we have demonstrated the modified, efficient, one pot synthesis of some low-molecular-weight chiral poly-carboxylate ligands derived form naturally occurring L-amino acids. These chiral poly-carboxylate ligands act as a growth modifier. As shown in the scheme 2.1, the energy minimized 3D space filled model has two distinct surfaces: (i) Hydrophilic (red balls) and (ii) Hydrophobic (grey balls). Presence of the amphiphilic surfaces in these molecules is important to act as a nucleation center in water. It is expected that they will form self-assembled supramolecular aggregates when dissolved in water. These aggregates can help the growth modification of the calcium and barium minerals by acting as a template.

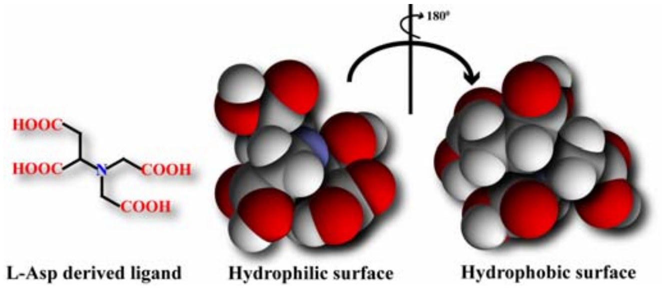

Scheme 2.1. Energy minimized 3D space filled model of polycarboxylate ligands.

2.1.1. Materials and Methods

All the organic additives and inorganic salts were analytically pure and purchased from Aldrich. All the solvents used were of HPLC grade. The water used in the experiment was the Milli-Q water. Optical micrograph images were taken in *Zeiss-Axio Cam-MRc* microscope fitted with the digital camera of air-dried samples on glass micro slides. Scanning electron micrograph (SEM) images were obtained by means of a *LEO-1430 VP* electron microscope on samples glued on an aluminum stub and gold sputtered. FT-IR analysis was carried out on air-dried minerals samples. All spectra recorded at 4 cm^{-1} resolution with 10 scan with a *Perkin Elmer-Spectrum One FT-IR Spectrometer* from 4000 to 450 cm^{-1}. A background spectrum was measured for pure KBr. To confirm the crystalline nature of the mineral sample powder X-ray diffraction (PXRD) data were recorded with *Seifert powder X-ray diffractometer (XRD 3003TT)* with CuK_{α} source (λ = 1.54 Å) on glass surface of air-dried sample. In order to determine presence of organic matrices, water of crystallization and nature of polymorphs in the obtained mineral crystals, the samples were analyzed thermally from 25 to 1000 ^{o}C using a *DT-40 thermal analyzer*. The temperature was increased at a rate of 2 ^{o}C/min.

The intensity data for single crystal were collected using a Bruker SMART APEX-II CCD diffractometer, equipped with a fine focus 1.75 kW sealed tube MoK_{α} radiation (λ = 0.71073 Å) at 273(3) K, with increasing ω (width of 0.3° per frame) at a scan speed of 3 s/frame. The SMART software was used for data acquisition. Data integration and reduction were undertaken with SAINT and XPREP [2.9] software. Multi-scan empirical absorption corrections were applied to the data using the program SADABS [2.10]. Structures were solved by direct methods using SHELXS-97 and refined with full-matrix least squares on F^2 using SHELXL-97 [2.11]. All non-hydrogen atoms were refined anisotropically. The hydrogen atoms were located from the difference Fourier maps and refined. Structural illustrations have been drawn with ORTEP-3 for Windows [2.12].

2.1.2. General synthesis of ligands L_{1-16}

An aqueous solution of chloro acetic acid was added to the solution of L-α amino acid in Milli-Q water (~1mM) in a round bottom flask and stirred for ~15 minutes at RT to make the solution homogeneous following scheme 2.2. The resulting solution was refluxed by continuous maintaining the pH of the solutions above the isoelectric point of the corresponding amino acids. Different equivalents of chloro acetic acids were added depending on the number of replaceable amine hydrogen present in the amino acids used. The resulting solution is then concentrated to about half of the original volume in reduced pressure. On cooling precipitate of NaCl starts forming. The precipitate was filtered and filtrate was acidified with dilute hydrochloric acid and kept overnight for re-crystallization. Crystals started growing in the solution, which was then dried in *vacuo*. The results are summarized in Table 2.1. Yields were not too high as the amino acids are water soluble and we are also doing the recrystallization in aqueous medium. It is particularly low for highly water soluble amino acids like glycine, alanine, lysine etc.

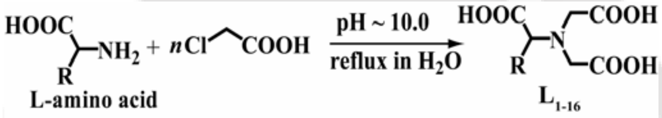

Scheme 2.2. Synthesis of polycarboxylate ligands.

Table 2.1. Synthesis of ligands L_{1-16}.

L	α-amino acid	*n*	Time	Yield [a](%)	L	α-amino acid	*n*	Time	Yield [a](%)
1	L-Alanine, Ala	2	5 hrs	32	2	L-Phenylalnine, Phe	2	6 hrs	65
3	L-Aspartic acid, Asp	2	8 hrs	37	4	L-Lysine, Lys	4	10 hrs	32
5	Glycine, Gly	2	8 hrs	34	6	L-Leucine, Leu	2	5 hrs	39
7	L-Isoleucine, Ile	2	5 hrs	41	8	L-Serine, Ser	3	7 hrs	35
9	L-Threonine, Thr	3	7 hrs	38	10	L-Tyrosine, Tyr	3	8 hrs	52
11	L-Glutamic acid, Glu	2	6 hrs	57	12	L-Asparagine, Asn	2	7 hrs	48
13	L-Glutamine, Gln	2	7 hrs	42	14	L-Histidine, His	2	7 hrs	51
15	L-Tryptophane, Trp	2	6 hrs	46	16	L-Arginine, Arg	2	5 hrs	34

[a] Isolated Yields

2.1.3. Characterization ligands L_{1-16}

The results of FT-IR analysis were shown in Table 2.2. It was found that the N-H stretching frequency which are predominant in the starting amino acids (~1400 cm^{-1} and ~3000 cm^{-1}) were absent in the product. The intensity of O-H stretching frequency bands at ~3400 cm^{-1} has increased in the product compared to the starting amino acids. The broad peak due to O-H vibration can be attributed to the extensive intermolecular or intramolecular hydrogen bonding that can be present due to the presence of many carboxylic groups. The C=O stretching frequency peak for the carboxylic groups comes at around ~1630 cm^{-1}(a broad peak for asymmetric C-O vibration) and ~1400 cm^{-1} (a shoulder for C-O symmetric vibration). This can be explained that the carboxylic acid groups are present mainly as carboxylate anions [2.13] at the neutral pH (pH at which crystals were grown). From this we can predict that *N*,*N*-dialkylation at the α-amine nitrogen is complete and there is insertion of few more carboxylic groups in the product. A representative FT-IR spectrum is given in Figure 2.1.

Table 2.2. FT-IR and melting points of ligands $\mathbf{L_{1\text{-}16}}$ derived from amino acids.

L	IR peaks (in cm^{-1})	Melting Points/ Decomposition Temp. (°C) of	
		product	amino acid
1	3449, 1631, 1412, 1115, 950	198-202	297
2	3451, 3071, 3023, 1741, 1574, 1457, 1048, 1036	208-211	283
3	3448, 3021, 1731, 1639, 1405, 1243, 1094	195-197	270-271
4	3433, 1634, 1406, 1101	244-246	224
5	3457,1721,1598,1419,1148,1076	192-195	233
6	3450, 1634, 1071	281-283	293-295
7	3448, 1634, 1116	279-281	284
8	3460,1638,1406,1096	198-201	228
9	3456, 1637, 1406, 1080	289-292	255-257
10	3447, 1634, 1408, 1170, 1053	310-312	342-344
11	3442, 1730, 1639, 1405, 1235, 1090	225-229	160
12	3448, 1608, 1379, 1271, 1187	299-302	234-235
13	3454, 1608, 1426, 1231	204-207	185-186
14	3436, 1632, 1397, 1170, 1070	269-272	287
15	3452, 1628, 1407, 1072	290-293	289
16	3444, 1603, 1447, 1015	245-248	244

Out of all the sixteen synthesized ligands, we have selected four which represents different types of amino acids *viz*: aliphatic nonpolar ($\mathbf{L_1}$), aromatic nonpolar ($\mathbf{L_2}$), acidic polar ($\mathbf{L_3}$) and basic polar ($\mathbf{L_4}$).

L_1 [2-(Bis-carboxymethyl-amino)-propionic acid]: Analysis – Calcd. for $C_7H_{11}NO_6$: C, 40.98; H, 5.40; N, 6.83%. Found: C, 41.27; H, 5.96; N 7.14%; ^{1}H NMR (400 MHz, D_2O, 25°C, TMS) δ (ppm): 1.4 (*d*, 3H), 3.3 (*s*, 4H), 3.7 (*qt*, 1H), ^{13}C NMR (100 MHz, D_2O, 25°C, TMS) δ (ppm): 17.4, 56.2, 61.4, 175.2, 177.1.

L_2 [2-(Bis-carboxymethyl-amino)-3-phenyl-propionic acid]: Analysis – Calcd. for $C_{13}H_{15}NO_6$: C, 55.51; H, 5.38; N, 4.98%. Found: C, 55.82; H, 5.96; N 5.23%; ^{1}H NMR (400 MHz, D_2O, 25°C, TMS) δ (ppm): 2.9 (*m*, 2H), 3.3 (*s*, 4H), 4.1 (*t*, 1H), 7.1-7.3 (*m*, 5H), ^{13}C NMR (100 MHz, D_2O, 25°C, TMS) δ(ppm): 41.7, 56.3, 61.8, 127,4, 129.7, 131.2, 140.9, 179.3, 184.3.

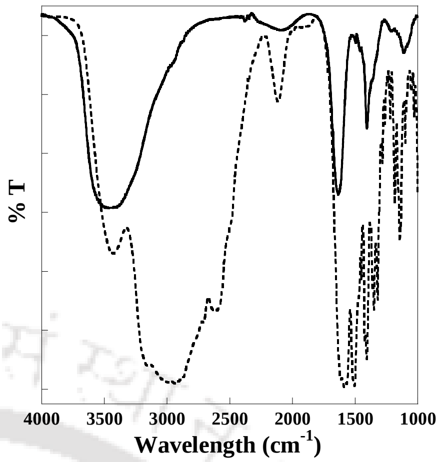

Figure 2.1. A comparative FT-IR spectra of starting amino acid, Lys (dashed line) and product, L_4 (solid line).

L_3 [2-(Bis-carboxymethyl-amino)-succinic acid]: Analysis – Calcd. for $C_8H_{11}NO_8$: C, 38.56; H, 4.45; N, 5.62%. Found: C, 39.07; H, 4.87; N 5.31%; ^{1}H NMR (400 MHz, D_2O, 25°C, TMS) δ (ppm): 2.6 (*d*, 2H), 3.5 (*s*, 4H), 4.0 (*t*, 1H), ^{13}C NMR (100 MHz, D_2O, 25°C, TMS) δ(ppm): 34.5, 58.3, 61.8, 179.3, 184.3.

L_4 [2,6-Bis-(bis-carboxymethyl-amino)-hexanoic acid]: Analysis – Calcd. for $C_{14}H_{22}N_2O_{10}$: C, 44.45; H, 5.86; N, 7.40%. Found: C, 45.11; H, 6.07; N 7.21%; ^{1}H NMR (400 MHz, D_2O, 25°C, TMS) δ(ppm): 1.3 (*m*, 2H), 1.7 (*m*, 2H), 2.1 (*m*, 2H), 3.2 (*m*, 2H), 3.4 (*s*, 8H), 4.2 (*t*, 1H), ^{13}C NMR (100 MHz, D_2O, 25°C, TMS) δ(ppm): 23.2, 28.5, 30.2, 41.4, 56.2, 59.1, 175.3, 180.4.

Growing of the crystals

The reaction systems were divided into two different groups: Milli-Q water system (control), and poly-carboxylate ligand system. In a typical experiment, 0.0005 M ligand solution mixed with 0.001 M $CaCl_2$ solution in Milli-Q water and kept at RT for 12 hrs without stirring. Then 0.001 M Na_2CO_3 or Na_2SO_4 solution was added slowly without much mechanical disturbance. The solution was kept at 25±2 °C for several days without any mechanical disturbance. When there was a large number of crystals present in the reaction vessel, the crystalline products were collected, vacuum-filtered and washed with Milli-Q water several times to remove the organic additives and then finally with anhydrous ethanol. The crystals were air-dried and kept in desiccator for 24 h before analysis.

2.1.4. Results and discussion

Crystallization of Calcium Carbonate

These low-molecular-weight poly-carboxylate ligands are efficient growth modifier (Scheme 2.3). The $CaCO_3$ crystal formation in the solution can be observed as an increase in the turbidity of the solution with time. Crystallization of $CaCO_3$ in the presence of ligand derived from L-Lysine (**L_4)** with five pendant carboxylic acid groups resulted in the formation of perfect octahedron shape of $CaCO_3$ crystals (Figure 2.2a to 2.2c) after 5 days. Time dependent formation of $CaCO_3$ crystal shows that each octahedron is formed by four parts of equal shape. Each part is of 200 μm in length. In the presence of this low-molecular-weight organic additive, further washing of the crystals with water did not change the crystal morphology. Elemental analysis (EDX) shows the presence of Ca, C and O (Figure 2.3).

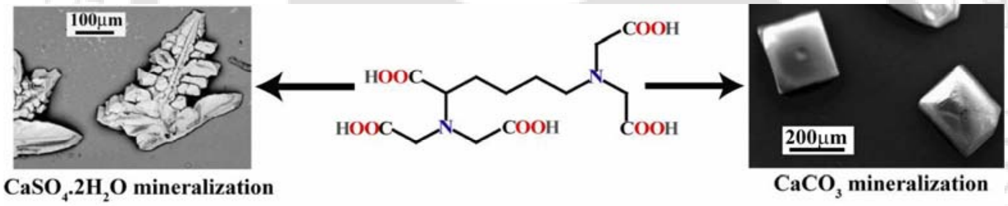

Scheme 2.3. Growth modification of calcium mineral

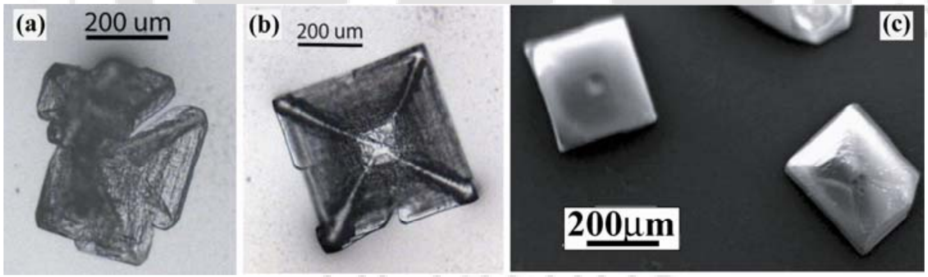

Figure 2.2. Optical micrograph images of $CaCO_3$ in presence of **L_4**. (a) after 2 days and (b) after 5 days and (c) SEM micrograph.

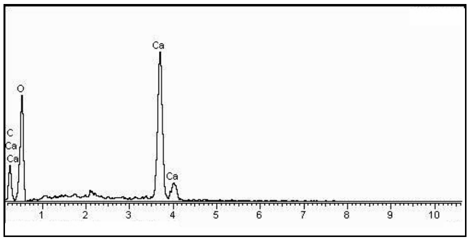

Figure 2.3. EDX of $CaCO_3$.

The precipitation of $CaCO_3$ in absence of additive was carried out under the same conditions as a control. In contrast to the above observations, instant bulk precipitation took place without any definite structures (Figure 2.4).

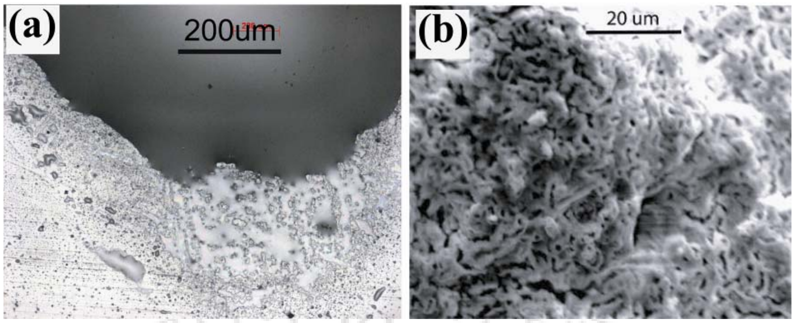

Figure 2.4. (a) Optical micrograph and (b) SEM micrograph of $CaCO_3$ in absence of growth modifier.

Thermo gravimetric analysis (TGA) profile of $CaCO_3$ shows the mass loss of 44 % (calc. 43.94 %) of the initial mass (Figure 2.5). This corresponds to the evolution of CO_2. Endothermic peak at 750^0C, and evolution of CO_2 prove the decomposition of $CaCO_3$ to CaO.

$$CaCO_3 \xrightarrow[700^0]{-\,CO_2} CaO + CO_2\uparrow$$

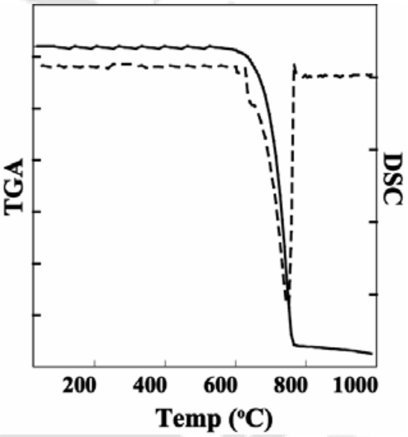

Figure 2.5. TGA-DSC plot of Calcite.

The FT-IR spectra of $CaCO_3$ crystals shows peaks at 1084, 876, 745 and 712 cm^{-1}(Figure 2.6a).
These peaks show the co-existence of both the calcite and vaterite phase in $CaCO_3$ crystals. This observation was reinforced by PXRD data. The PXRD pattern (Figure 2.6b) shows the diffraction peaks from calcite as well as vaterite phase. The assignment of polymorphs to calcite or vaterite was carried out by comparison of the literature data with their PXRD patterns. The absolute contents of $CaCO_3$ polymorphs *viz.* calcite and

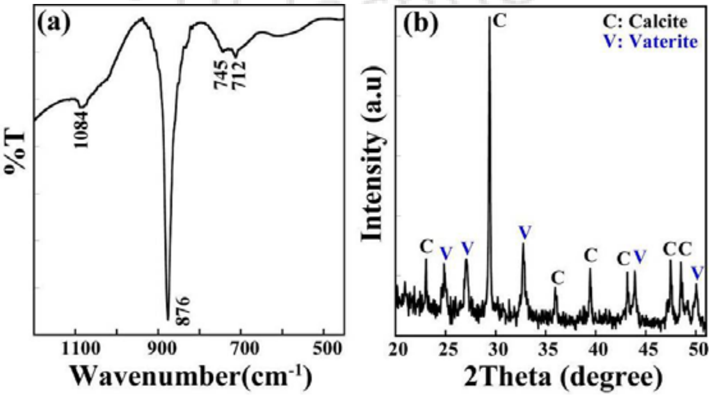

Figure 2.6. (a) FT-IR spectrum and (b) PXRD pattern of $CaCO_3$ crystals.

vaterite was found to be 80% and 20% respectively. By addition of ligand **L_3** derived from L-aspartic acid formation of plate type crystal was observed (Figure 2.7a). These plates also stacked to give octahedron structure with time. Each side of the octahedron is 200 μm in length. Similarly in presence of **L_2** and **L_1** we again got octahedral calcite (Figure 2.7b, 2.7c). The crystal phase is confirmed by FT-IR and PXRD.

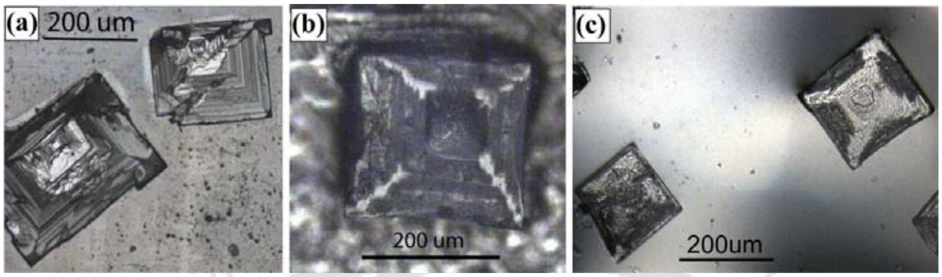

Figure 2.7. Optical micrograph images of $CaCO_3$ in presence of (a) **L_3,** (b) **L_2** and (c) **L_1.**

Crystallization of Calcium Sulfate

Similar crystal growth modification is followed for the formation $CaSO_4$ crystals. In presence of ligand **L_4** it forms leaf structures (Figure 2.8a, 2.8b). Time dependent studies show the formation of leaf structures with stacked plates of varying length (200 – 600 μm). Matured crystals show the formation of solid leaf structures (Figure 2.8c).

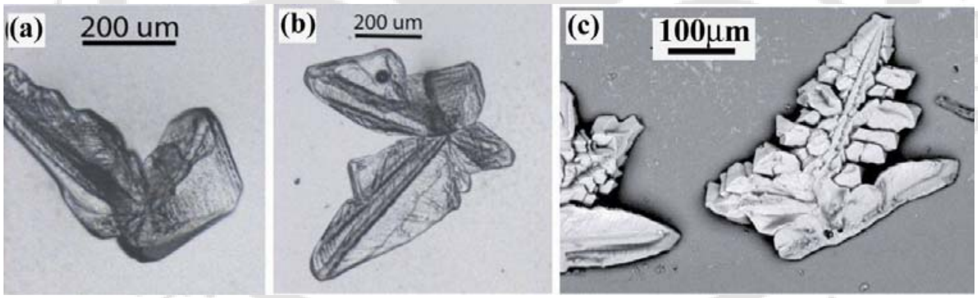

Figure 2.8. Optical micrograph images of Gypsum in presence of **L_4**. (a) after 3 days, (b) after 7 days and (c) SEM micrograph after 15 days.

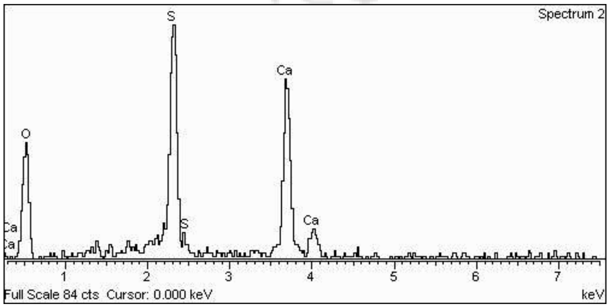

Figure 2.9. EDX of $CaSO_4$.

EDX shows the presence of Ca, S and O (Figure 2.9). The precipitation of $CaSO_4$ in absence of additive was also carried out under the same conditions as a control. Like $CaCO_3$ mineralization in absence of any additives, instant bulk precipitation took place without any definite structures (Figure 2.10). The crystal phase of the obtained $CaSO_4$ was pure gypsum ($CaSO_4.\ 2H_2O$) confirmed by FT-IR (Figure 2.11a) and PXRD pattern (Figure 2.11b). TGA analysis shows (Figure 2.11c) the loss of two water molecules at 150^0C (mass loss of 20.98 %) and DSC analysis shows an endothermic peak centered on 150^0C. The overall course of the reaction is

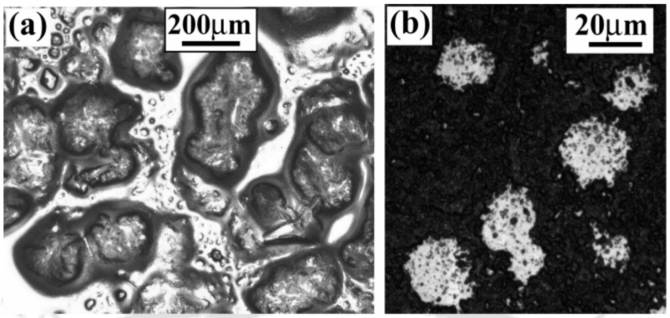

Figure 2.10. (a) Optical micrograph and (b) SEM micrograph of $CaSO_4$ in absence of any additive.

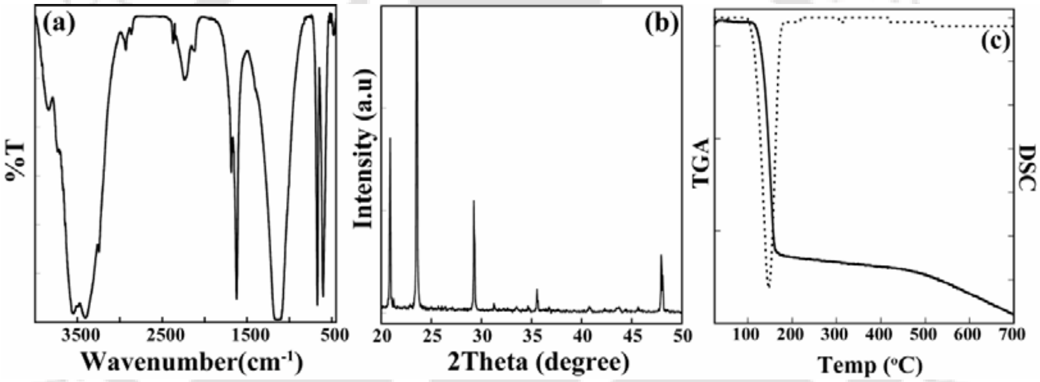

Figure 2.11. (a) FT-IR spectrum, (b) PXRD analysis of Gypsum in the presence of $\mathbf{L_4}$ and (c) TGA-DSC plot of Gypsum crystals.

$$CaSO_4.2H_2O \xrightarrow[150^{0}]{-\,2H_2O} CaSO_4 + 2H_2O$$

In presence of ligand $\mathbf{L_3}$, $CaSO_4$ takes the shape of non-uniform broken leaf (Figure 2.12a). These non-uniform leaf structures are formed by stacking the plate crystals even after sufficient growing time. The crystal phase is also confirmed to be gypsum in this case. In the case of $CaSO_4$ formation both the ligands $\mathbf{L_{1\text{-}2}}$ show the same trends as $\mathbf{L_3}$ and forms the non-uniform broken leaf structures as shown in Figure 2.12b and 2.12c respectively.

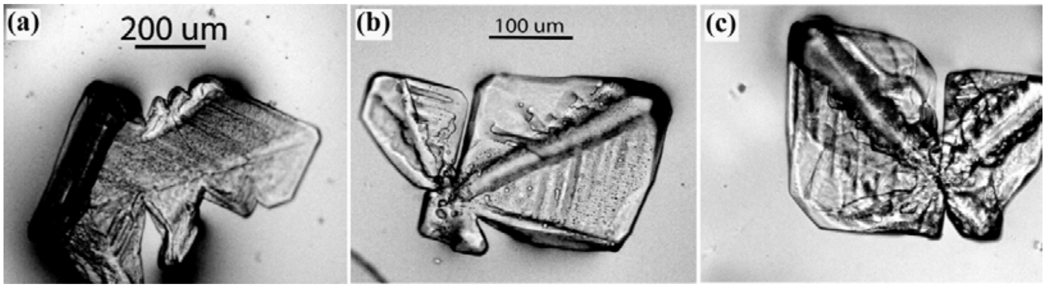

Figure 2.12. Optical images of Gypsum in presence of (a) $\mathbf{L_3}$ and (b) $\mathbf{L_2}$ and (c) $\mathbf{L_1}$ after 10 days.

2.1.5. Summary

Sixteen low-molecular-weight poly-carboxylate chiral ligands derived form naturally occurring L-α-amino acids has been synthesized. These chiral ligands when used as an additive, influences the growth of some common calcium minerals. Ligand $\mathbf{L_4}$, derived from L-lysine bearing five pendant carboxylic acid groups proved to be the best matrix for crystal growth modifier among these four ligands. Non-polar side chain containing amino acid derivatives were also acted as a growth modifier in the mineralization processes.

2.2 Polymorphism in $CaCO_3$

The control of size, shape, and assembly of crystalline materials is a hallmark of biomineralization processes [2.14]. Biominerals are often hierarchically organized on a scale from angstroms to millimeters. Calcium based minerals are the most abundant minerals out of more than 60 inorganic minerals found in living organisms. It is needed to form bones, teeth and is also required for blood clotting, transmission of signals in nerve cells, and muscle contraction. The importance of calcium for preventing osteoporosis is probably its most well-known role [2.15]. Most calcium supplements contain calcium carbonate [2.16]. In organisms, calcium carbonate has polymorphs of calcite (rhombohedra), aragonite (needles), vaterite (polycrystalline spheres) and to a lesser extent crystalline mono and hexahydrate [2.17]. The amorphous form is the least stable phase of calcium carbonate (ACC), which is supposed to be used as reservoirs of $CaCO_3$ during the animal molting period [2.18]. The recent progress in carbonate precipitation with complex shapes mainly concerns $CaCO_3$ due to its importance for industry (e.g. pigment, filler and scale formation) and biomineralization. Two general approaches were pursued for the morphogenesis of $CaCO_3$. One approach predominately employs soluble polymeric additives. These soluble additives lead to the formation of micro-particles with complex shapes and even hybrid of two different crystal polymorphs. The second method employs macroscopic templates as a confined reaction environments for precipitation [2.19].

Organic acids can serve different purpose as ligand as well as additives, which in turn gives different results (Scheme 2.4).

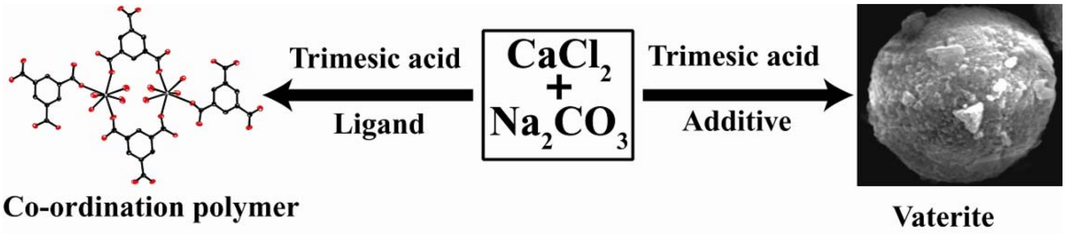

Scheme 2.4. Variation in the role of organic acids.

For crystallization, the ions that will form the crystal lattice must come together with the right orientation to form a stable structure. This stable structure resembles the crystal phase being deposited [2.20]. The crystal morphology depends on the differences of the crystal faces in surface energy and external growth environment. The surface energy of a crystal face can be lowered by the adsorption of an additive. Therefore, the shape of crystals can be affected by various factors, *i.e.,* inorganic ions or organic additives [2.21]. The presence of divalent ions in the solutions from which calcium carbonate polymorphs precipitate, are very important both for the determination of the polymorphs formed and for the development of structural imperfections [2.22]. In calcite the Ca^{2+} cations can be substituted by other especially isovalent inorganic impurities like Mg^{2+} and Zn^{2+} and the process are energetically favorable [2.23]. The impurity ions can enter into the host lattice by entering the exact position of Ca site. Relaxing the environment around the defect causes further stabilization of the crystal and inhabitation of the growth of the most stable polymorph. This is in agreement with the experimental findings [2.24].

In this section, we have studied the influence of organic and inorganic additives in $CaCO_3$ polymorph synthesis and shown the growth of vaterite, thermodynamically the least stable polymorph of $CaCO_3$ in presence of various low-molecular-weight organic as well as inorganic additives in polar non-aqueous solvents *viz*: MeOH, *n*-Propanol and DMSO. Although non-aqueous solvents are not biologically relevant, but to understand the mechanism of polymorph synthesis and effect of different external parameters *viz.* nature of additives, types of solvents, temperature on polymorph synthesis we have carried out these experiment in non-aqueous medium. The selected polar non-aqueous solvents are highly miscible with water. Again to study the effect of proticity of the polar solvents, we have selected polar protic solvents *viz*: MeOH, *n*-propanol and polar aprotic solvents *viz.* DMSO. The organic additives used were grouped as additives with and without affinity to Ca^{2+} coordination as shown in scheme 2.5 and 2.6 respectively.

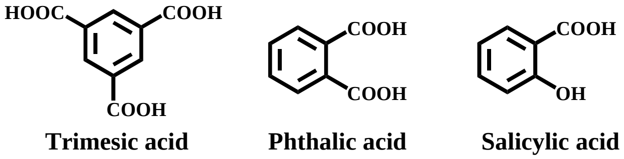

Scheme 2.5. Ligands with affinity to Ca^{2+} coordination.

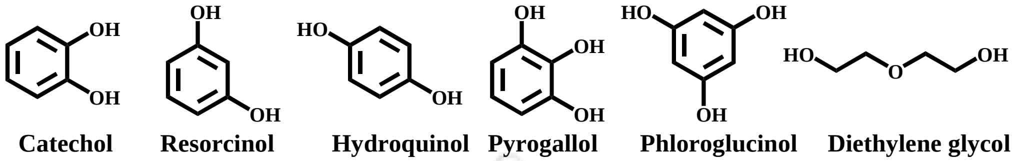

Scheme 2.6. Ligands with no affinity to Ca^{2+} coordination.

Generally, hydrophobic vaterite form more easily in non-aqueous solvents due to acceleration of spontaneous precipitation rate with stabilizer effects for protection of vaterite transformation to calcite [2.25].

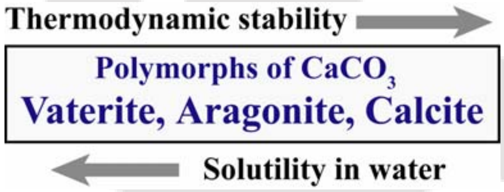

2.2.1. Crystallization Experiments

In a typical experiment, 1 mM of various organic / inorganic additives were mixed with 100 mM of $CaCl_2$ solution in methanol and kept at RT for 12 hrs with constant stirring. Then 100 mM Na_2CO_3 solution in Milli-Q water was added in ten equal steps with constant stirring over 5 hrs. The resulting mixture kept at RT without much mechanical disturbance. The crystal formation in the solution can be observed as an increase in the turbidity of the solution with time. When there was a large number of precipitate present in the reaction vessel, the crystalline products were collected through centrifugation at 5,000 rpm and washed with methanol / acetone several times to remove the organic additives and then finally with diethyl ether. The crystals dried in air for 24 h and kept in desiccators before analysis.

2.2.2. Results and Discussions

Despite the non-physiological nature, as most of the organic compounds are insoluble in water, we have investigated the influence of non aqueous solvents which are miscible with water in the $CaCO_3$ polymorphism. In the absence of any additives in non aqueous solvents, we got aragonite as the major polymorph (characteristic PXRD pattern at $2\Theta = 26.23$ which corresponds to {111} plane) (Figure 2.13a). SEM micrograph in Figure 2.13b shows the formation of spherical aragonite particles of average diameter of 1µm. These particles aggregate to form a 3D spherical arrangement having average diameter of 5 µm. In case of *n*-propanol, sharp aragonite needles has formed (Figure 2.13c), whereas in DMSO we got unique intertwined aragonite rods (Figure 2.13d). From these studies we can tell that non-aqueous solvents play an important role in the polymorphism of $CaCO_3$.

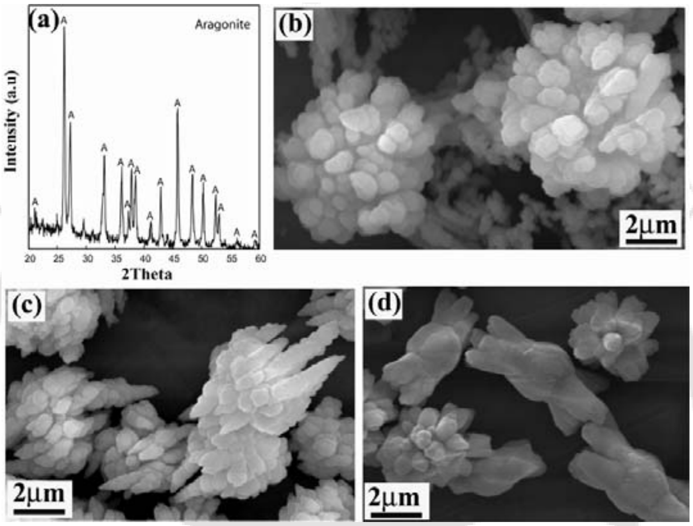

Figure 2.13. (a) PXRD in absence of any additive (aragonite), (b) SEM micrograph of aragonite in methanol, (c) aragonite in *n*-propanol and (d) aragonite in DMSO.

Crystallization with organic additives having affinity to Ca^{2+} coordination

In presence of 1 mM trimesic acid *i.e.*, 100 times dilute than that of $CaCl_2$ (100 mM), we got perfectly spherical $CaCO_3$. A mixture of hexagonal vaterite polymorph (P63/mmc, {1 0 1}) and orthorhombic aragonite (Pmcn, {1 1 1}) (PDF No. 00-033-0268) was confirmed by PXRD analysis (Vaterite 61.41% and Aragonite 38.59%) (Figure 2.14a) [2.26]. Characteristic FT-IR bands corresponding to mixture of vaterite as well as aragonite were found to be at 1086, 876, 852, 745 and 712 cm^{-1} (Figure 2.14b) [2.27] The SEM micrographs Figure 2.15a shows polycrystalline spherical vaterite having diameter in the range of 3 – 4 µm. The surface of these spheres are not smooth and small particles of 50-200 nm size assemble together to form these micron scale spheres. When trimesic acid used in stoichiometric amount *i.e.* 1:1 molar ratio with $CaCl_2$ and allowed for further growth, we got single crystals in the dimension of 20-30 µm (Figure 2.15b). The crystal morphology does not match with any of the known $CaCO_3$ polymorph.

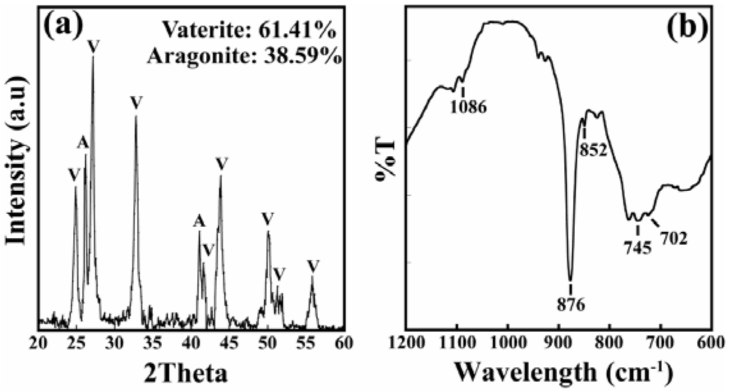

Figure 2.14. (a) PXRD of $CaCO_3$ and (b) FT-IR spectra of $CaCO_3$ (Vaterite & Aragonite) in presence of trimesic acid in MeOH.

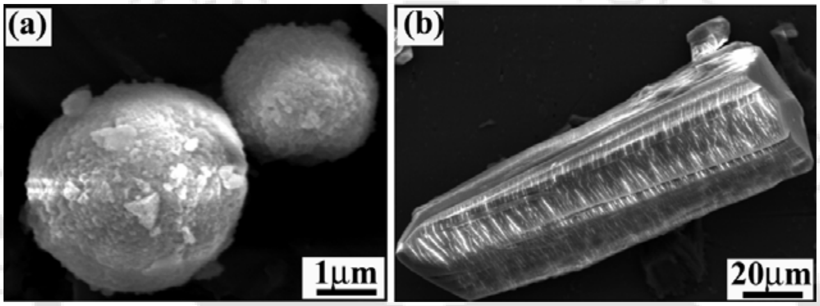

Figure 2.15. SEM micrograph of (a) Vaterite in presence of trimesic acid and (b) Ca-trimesic acid co-ordination polymer.

In this case, trimesic acid is acting as a coordinating ligand instead of an additive. Single crystal X-ray structure analysis of these crystals reveals the formation of calcium co-ordination polymer with trimesic acid. The ORTEP plot shows the formation of seven-coordinated Ca complex in the solid-state (Figure 2.16a). Crystallographic refinement parameters of calcium trimesic acid co-ordination polymer are listed in appendix (Table 2.1A, 2.2A). Similar type of coordination polymeric structure is known [2.28]. Each Ca^{2+} ion is coordinated to seven oxygen atoms in a distorted pentagonal bipyramidal fashion. Four water molecules and one carboxylate oxygen are situated in basal plane. Other two oxygen atom of carboxylic acid occupy the apical positions. Four water oxygen atoms lie exactly on the basal plane. Ca^{2+} ion is deviated 0.377 Å from that plane (Figure 2.16b). The proton H5 bonded to O5 of one of the carboxylate groups forms a strong hydrogen bond O5–H5···O6 linking the tremesic acid anions in chains. All four water molecules are not only involved in the coordination of Ca but also form strong hydrogen bonds to carboxylate oxygen and to the other coordinated water molecules. Overall hydrogen bonding results in the formation of a polymeric layered structure, where trimesic acid unit is packed in alternate up and down fashion (Figure 2.16c).

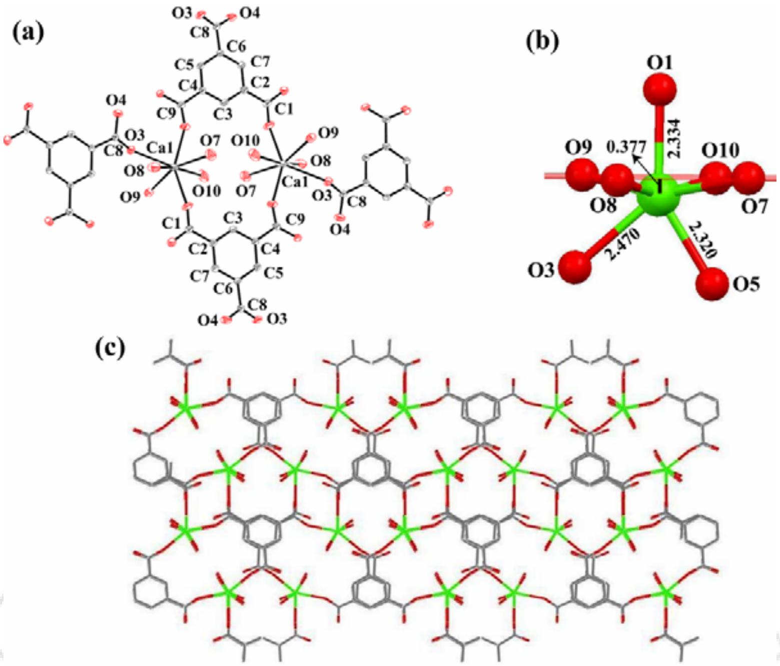

Figure 2.16. (a) ORTEP plot of Ca-trimesic acid complex and (b) schematic representation of Ca^{2+} coordination sphere and (c) Packing diagram of Ca-trimesic acid complex along crystallographic *c*-axis.

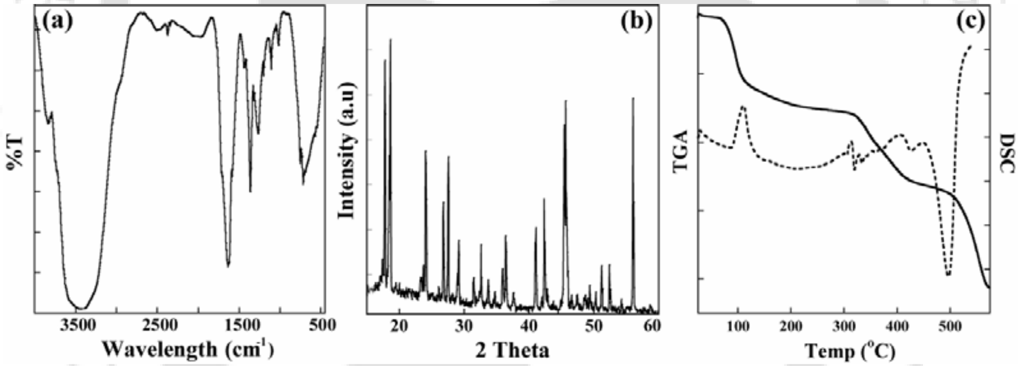

Figure 2.17. (a) FT-IR spectra, (b) PXRD pattern of Ca-trimesic acid coordination polymer before heating and (c) TGA-DSC plot of Ca-trimesic acid.

FT-IR spectra, PXRD pattern and of Ca-trimesic acid coordination polymer before heating is shown in Figure 2.17a and 2.17b respectively. The TGA and DSC profile of Ca-trimesic acid coordination polymer is shown in Figure 2.17c. On heating this co-ordination polymer at 600°C for 6h in a muffle furnace, we got thermodynamically stable calcite having porous structure (Figure 2.18) which resembles to Sea Urchin skeletal plates [2.19]. PXRD analysis of Ca-trimesic acid coordination polymer after thermal decomposition at 600 ^{0}C shows formation of thermodynamically most stable calcite with characteristic pattern at 2Θ = 29 which corresponds to {104} plane (Figure 2.19a). FT-IR spectra also show characteristic stretching frequencies at 1082, 878 and 708 cm^{-1} (Figure 2.19b). Like trimesic acid, phthalic acid also acts as a growth modifier for vaterite polymorph (Vaterite, syn 90.06% and Calcite 9.94%) in methanol which was confirmed by PXRD (PDF No. 01-074-1867) (Figure 2.20a). SEM micrograph in Figure 2.20b shows sphere like and oval shaped vaterite in the dimension of 2–3 µm. High resolution image reveals smooth, uniform surface unlike rough polycrystalline vaterites obtained in presence of trimesic acid.

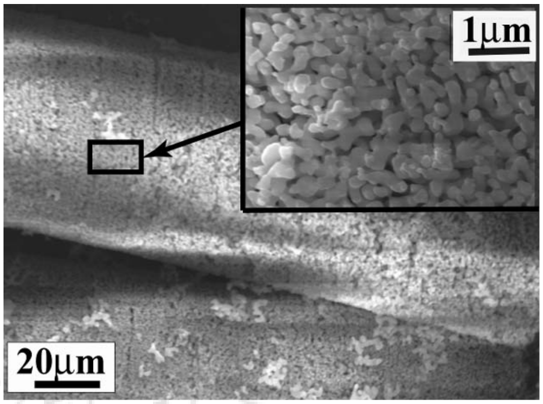

Figure 2.18. SEM micrograph of Ca-trimesic acid co-ordination polymer after heating at 600°C.

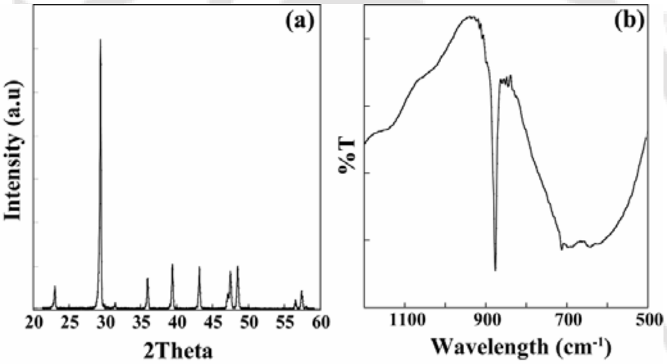

Figure 2.19. (a) PXRD pattern and (b) FT-IR spectra of Ca-trimesic acid coordination polymer after heating at 600 °C.

When we increased the amount of phthalic acid (1:1 molar ratio with, $CaCl_2$), we got calcium co-ordination polymer as reported earlier [2.29]. FT-IR spectra and PXRD pattern and of Ca-phthalic acid coordination polymer before heating is shown in Figure 2.21a and 2.21b respectively. The TGA and DSC profile of Ca-phthalic acid coordination polymer is shown in Figure 2.21c.

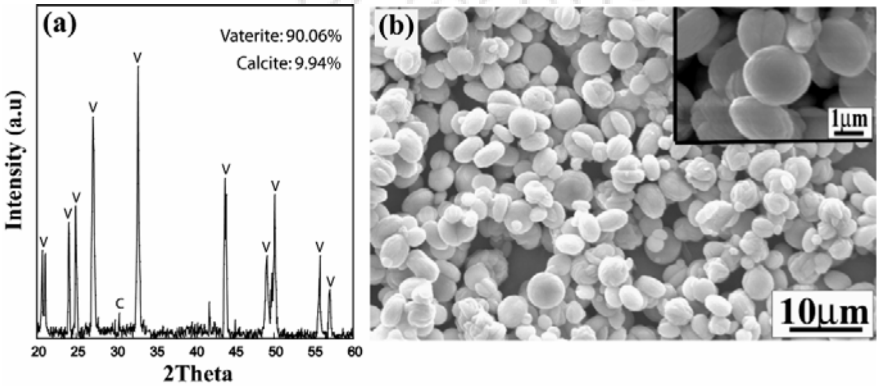

Figure 2.20. (a) PXRD and (b) SEM micrograph of Vaterite in presence of phthalic acid.

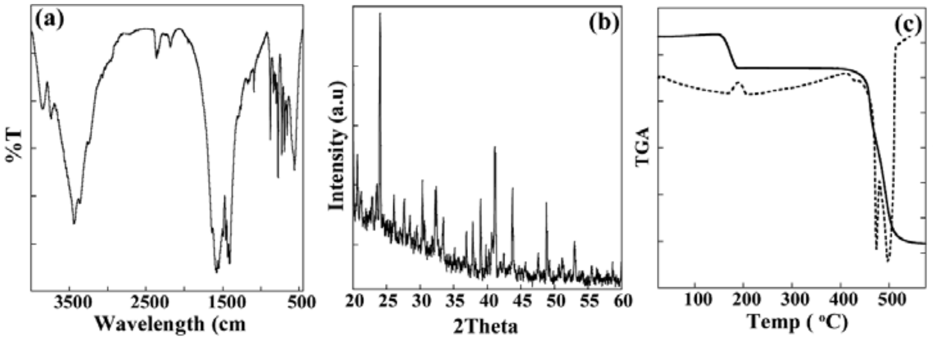

Figure 2.21. (a) FT-IR spectra, (b) PXRD pattern of Ca-phthalic acid coordination polymer before heating and (c) TGA-DSC plot of Ca-phthalic acid.

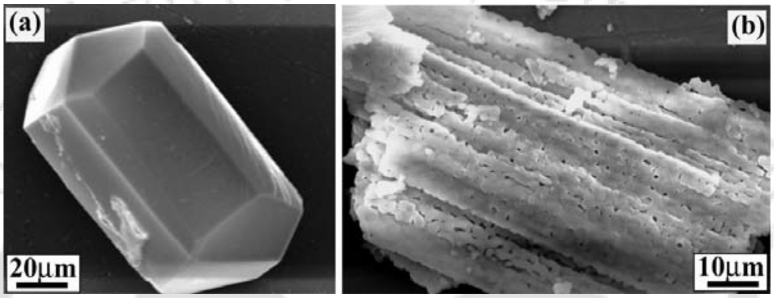

Figure 2.22. SEM micrograph of (a) Ca-phthalic acid co-ordination polymer, (b) after heating at 600°C.

SEM micrograph (Figure 2.22a) also shows single crystalline rhombohedral block of average thickness 20 μm. After heating at 600°C for 5hrs its crystalline nature was lost and we got stacks of porous calcite layers as shown in Figure 2.22b. Characteristic PXRD peaks and FT-IR spectra of Ca-phthalic acid coordination polymer after thermal decomposition at 600 ^{0}C confirms the formation of thermodynamically most stable calcite (Figure 2.23). Salicylic acid also inhibits the growth of calcite phase in methanol. It helps in the formation of vaterite as the major polymorph (Vaterite, syn 76.37% and Aragonite 23.63%) which is confirmed by PXRD (PDF No. 01-074-1867) (Figure 2.24a). SEM micrograph in Figure 2.24b shows growth of uniformly truncated spherical vaterite, which is formed due to layer by layer growth. Like previous cases, we again got calcium

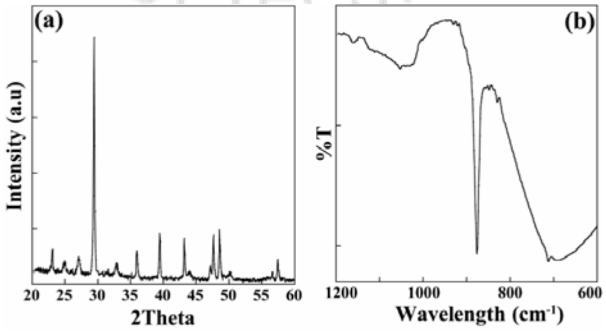

Figure 2.23. (a) PXRD pattern and (b) FT-IR spectra of Ca-phthalic acid coordination polymer after heating at 600 ^{0}C.

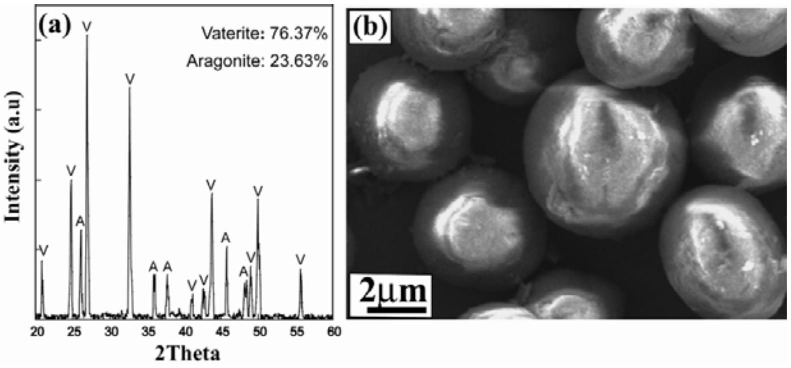

Figure 2.24. (a) SEM micrograph of Vaterite in presence of salicylic acid, (b) PXRD.

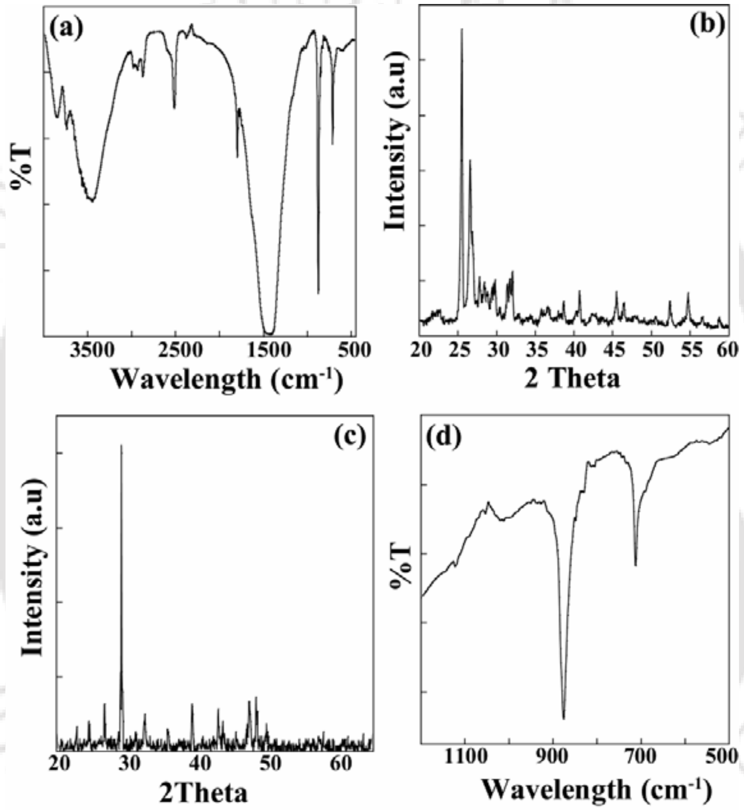

Figure 2.25. (a) FT-IR spectra (b) PXRD pattern of Ca-salicylic acid coordination polymer before heating, (c) PXRD pattern and (d) FT-IR spectra after heating at 600 ^{0}C.

co-ordination polymer with coordination number of Ca^{2+} ion 8, which is similar to that of the reported structure [2.30] when we used salicylic acid and $CaCl_2$ in 1:1 ratio. FT-IR spectra and PXRD pattern of Ca-salicylic acid coordination polymer before heating is shown in Figure 2.25a and 2.25b respectively. The formation of thermodynamically most stable calcite on thermal decomposition of Ca-salicylic acid coordination polymer is confirmed through characteristic PXRD peaks and FT-IR spectra which is shown in Figure 2.25c and 2.25d respectively. Figure 2.26a shows SEM micrograph of single crystalline rectangular block of Calcium-salicylic acid coordination polymer. After heating at 600^{o}C we got porous stacked plates of calcite (Figure 2.26b). The TGA and DSC profile of Ca-salicylic acid coordination polymer is shown in Figure 2.26c. The results of small organic additives with affinity to Ca^{2+} coordination were summarized in the Table 2.3.

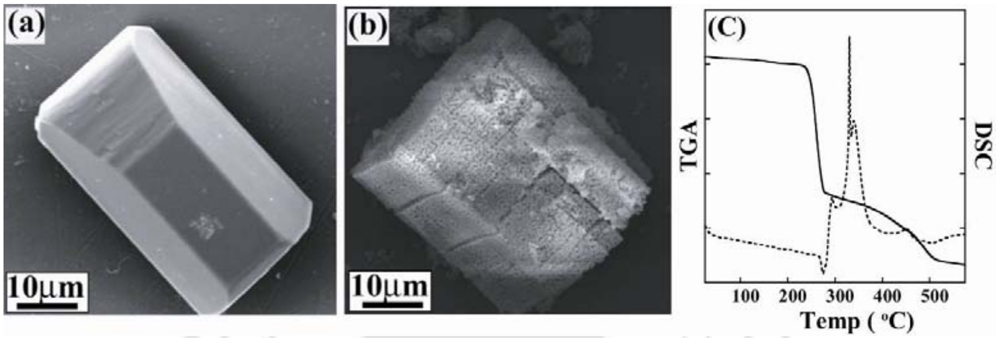

Figure 2.26. SEM micrograph of (a) Ca-salicylic acid precursor salt, (b) after heating at 600°C and (c) TGA-DSC plot of Ca-salicylic acid

Table 2.3. $CaCO_3$ polymorphs in presence of various small organic additives with affinity to Ca^{2+} coordination in MeOH at RT.

Sl. No.	Additive	Nature of additive	Major $CaCO_3$ polymorph	Morphology (size)	PDF no. from PXRD
1.	Trimesic acid	Organic additives with affinity to Ca^{2+} coordination	Vaterite	Spherical, diameter 2-4 μm	[00-033-0268]
2.	Phthalic acid		Vaterite, syn		
3.	Salicyclic acid		Vaterite, syn	Hexagonal P63/mmc	[01-074-1867]

Crystallization with organic additives having no affinity to Ca^{2+} coordination

$CaCO_3$ mineralization in presence of various low-molecular-weight organic additives which does not coordinate to the Ca^{2+} ion has also been carried out at RT in methanol using organic compounds shown in scheme 2.6. Here also we got spherical vaterite polymorphs of different dimensions form as a major polymorph (Figure 2.27). All of which are characterized by PXRD, FT-IR. The results were summarized in Table 2.4.

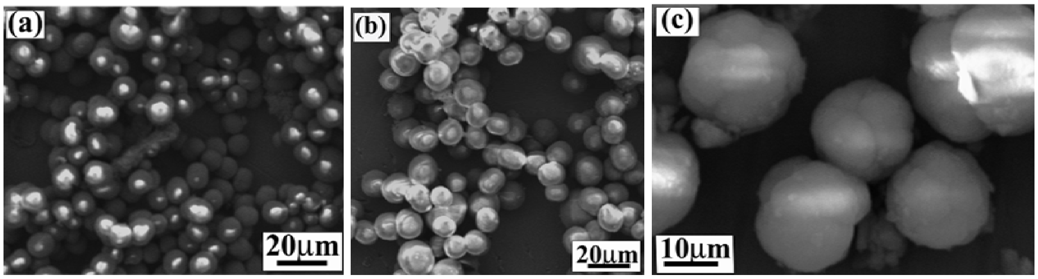

Figure 2.27. Some representative SEM micrograph of Vaterite polymorph in presence of (a) catechol, (b) resorcinol and (c) hydroquinol.

Table 2.4. $CaCO_3$ polymorphs in presence of various small organic additives with no affinity to Ca^{2+} coordination in MeOH at RT.

Sl. No.	Additive	Nature of additive	Major $CaCO_3$ polymorph	Morphology (size)	PDF no. from PXRD
1.	Catechol	Organic additives without affinity to Ca^{2+} coordination	Vaterite, syn	Spherical in the dimension range 2-4 µm Lattice: Hexagonal SG: P63/mmc	[01-074-1867]
2.	Resorcinol				
3.	Hydroquinol				
4.	Pyrogallol				
5.	Phloroglucinol				
6.	Diethylene Glycol				

Effect of inorganic ions as an additive

We have also tested the effect of transition metal ions as an additive in $CaCO_3$ mineralization in methanol. We again obtained spherical vaterites of different dimensions as a major polymorph (Figure 2.28). In presence of non-transition metals we got polycrystalline spherical vaterites. All of which are characterized by PXRD, FT-IR. The results were summarized in Table 2.5.

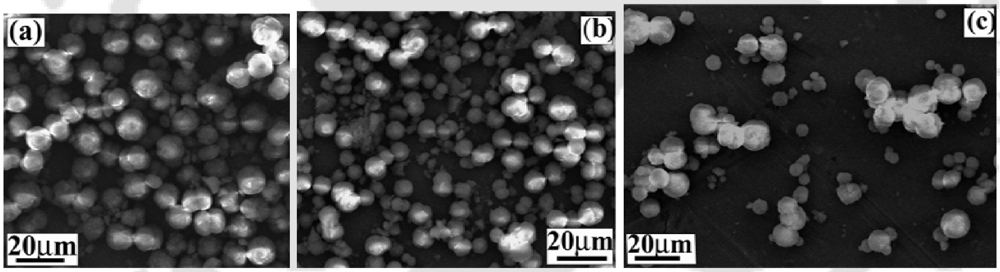

Figure 2.28. Some representative SEM micrograph of Vaterite polymorph in presence of (a) Mn^{2+}, (b) Fe^{3+} and (c) Cu^{2+}.

Table 2.5. $CaCO_3$ polymorphs in presence of metal ions as additives in MeOH at RT.

Sl. No.	Additive	Nature of additive	Major $CaCO_3$ polymorph	Morphology (size)	PDF no. from PXRD
1.	Mn^{2+}	Transition metal ions	Vaterite, syn	Spherical of diameter 2-4 µm Lattice: Hexagonal SG: P63/mmc	[01-072-0506]
2.	Fe^{2+}				
3.	Fe^{3+}				
4.	Co^{3+}				
5.	Ni^{2+}				
6.	Cu^{2+}				
7.	Zn^{2+}				
8.	Mg^{2+}	Non-transition metal ions	Vaterite, syn	Spherical of diameter 2-4 µm Lattice: Hexagonal SG: P63/mmc	[01-072-0506]
9.	Sr^{2+}				
10.	Ba^{2+}				

Effect of solvents in polymorph control at RT

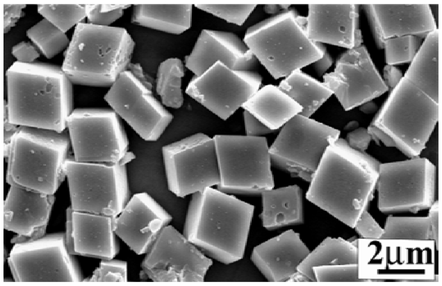

Figure 2.29. SEM micrograph of Calcite.

When we carried out $CaCO_3$ crystallization in presence of various low-molecular-weight organic and inorganic additives in water, we always got thermodynamically most stable calcite polymorph at RT (characteristic PXRD pattern at $2\Theta = 29$ corresponds to {104} plane) (Figure 2.29). The results were summarized in Table 2.6. These results confirm that in water calcite is the most stable polymorph at RT and the nature of additives has no effect on the polymorphism in water.

Table 2.6. $CaCO_3$ polymorphs in presence of small organic / inorganic additives in H_2O at RT.

Sl. No.	Additive	Solvent	Major $CaCO_3$ polymorph	Morphology (size)	PDF no. from PXRD
1.	Trimesic acid	H_2O	Calcite	Rhombohedral	[01-086-2342]
2.	Phloroglucinol				
3.	Fe^{3+}				
4.	Mg^{2+}				
5.	No additive				

Effect of temperature in polymorph synthesis in presence of additives

We have also carried out temperature dependent study of $CaCO_3$ mineralization in presence of various additives in different non-aqueous solvents. The results were summarized in Table 2.7. Different solvents are used to cover the wide temperature range. At extreme low temperature (-190°C) we got calcite as major polymorph irrespective of the nature of additives. But the morphology changes with the type of additive used. At extreme high temperature (189°C) we got calcite as major polymorph along with substantial amount of aragonite. These two extreme temperatures were achieved by using liquid N_2 and boiling point of DMSO respectively. When we carried out $CaCO_3$ crystallization in ice-water mixture (4°C), in boiling MeOH (bp, 65°C) and in boiling *n*-Propanol (bp, 97°C), we got vaterite and aragonite as the most stable polymorph. They are present in different ratio. SEM micrograph of $CaCO_3$ polymorphs in different temperature is shown in Figure 2.30.

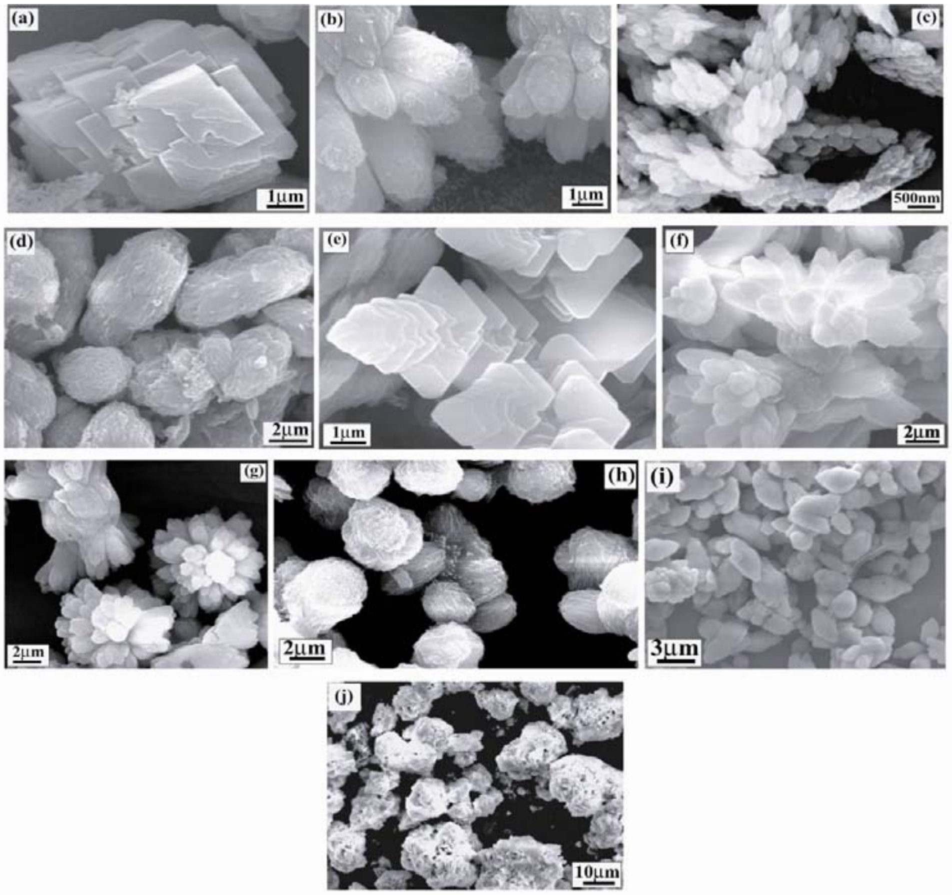

Figure 2.30. SEM micrograph of $CaCO_3$ polymorph in presence of trimesic acid at (a) -190°C, (b) 4°C, (c) 65°C, (d) 97°C, (e) 189°C, (f) -190°C in presence of Mg^{2+}, (g) 4°C in presence of Mg^{2+}, (h) 65°C in presence of Mg^{2+}, (i) 97°C in presence of Mg^{2+} and (j) 189°C in presence of Mg^{2+}.

2.2.3. Summary

Various low-molecular-weight organic as well as inorganic additives in non-aqueous solvents act as a crystal growth modifier for $CaCO_3$ polymorphs. The proticity of the polar non-aqueous solvents has no effect but overall the non-aqueous solvents have effect on morphology and polymorph synthesis. In presence of coordinating and non-coordinating organic additives as well as transition/non-transition metal ions, we got vaterite as the major polymorph. Organic additives with an affinity towards Ca-coordination forms coordination polymer when used as ligand. These single crystals form pure porous calcite polymorph when heated to 600°C. We got only aragonite in non-aqueous solvents in absence of any additives. In water we got only calcite polymorph irrespective of the nature of additive. In aqueous medium, vaterite is thermodynamically least stable but the most soluble polymorph of $CaCO_3$. According to Ostwald's rule [2.31], the least stable phase with the highest solubility is formed preferentially in the solution, and then transformed within a few minutes to calcite, vaterite or aragonite under different conditions [2.32].

Table 2.7. Temperature dependent study of $CaCO_3$ polymorph synthesis.

Sl. No.	Additive	Condition	% of $CaCO_3$ polymorph	Morphology (size)	PDF no. from PXRD
1.	Trimesic acid	-190°C	90.15 % (C) 9.85 % (V)	Layered Rhombohedra, 2 µm	[01-086-2342] [00-033-0268]
2.		4°C	Vaterite, Syn	Flower like aggregates (2 µm) with nano fibers on the surface	[01-074-1867]
3.		25°C	Vaterite, Syn	Polycrystalline sphere of diameter in the range 3 – 4 µm	[01-074-1867]
4.		65°C	63.42 % (A) 36.56 % (V)	Segmented arrangement of rods with thickness (500-600 nm)	[00-005-0453] [01-074-1867]
5.		97°C	39.72 % (C) 33.92 % (V) 26.36 % (A)	Polycrystalline ellipsoid of diameter 2 µm with rough surface	[01-086-2342] [01-074-1867] [00-005-0453]
6.		189°C	45.22 % (C) 36.42 % (V) 18.36 % (A)	Unique hierarchal arrangement of plates leading to rhombohedron	[01-086-2342] [01-074-1867] [00-005-0453]
7.	Mg^{2+}	-190°C	83.91 % (C) 16.09 % (V)	Flower like aggregation of blocks(2 µm)	[01-086-2342] [01-074-1867]
8.		4°C	56.35 % (A) 43.68 % (V)	Flower like aggregation of blocks(2 µm) with rough surface	[00-005-0453] [01-074-1867]
9.		25°C	Vaterite, Syn	Polycrystalline sphere, 3–4 µm	[01-074-1867]
10.		65°C	56.53 % (A) 43.47 % (V)	Aggregation of thin plates into sphere (2 µm) of rough surface	[00-005-0453] [01-074-1867]
11.		97°C	39.80 % (C) 36.06 % (V) 24.13 % (A)	Uneven hexagonal morphology of average thickness 3 µm	[01-086-2342] [01-074-1867] [00-005-0453]
12.		189°C	46.17 % (C) 33.82 % (A) 20.01 % (V)	Aggregation of thin plates without any uniform structure	[01-086-2342] [00-005-0453] [01-074-1867]

References:

[2.1] F. C. Meldrum, J. Cryst. Growth 231 (2001) 544.

[2.2] V. V. Hardikar, E. Matijevic, Colloids Surf A 186 (2001) 23-31.

[2.3] (a) K. Naka, Y. Tanaka, Y. Chujo, Langmuir 18 (2002) 3655, (b) M. Sedlak, H. Colfen, Macromol Chem Phys. 202 (2001) 587, (c) L. B. Gower, D. J. Odom, J. Cryst. Growth 210 (2000) 719.

[2.4] G. Falini, M. Gazzano, A. Ripamonti, Chem. Commun. (1996) 1037.

[2.5] F. Manoli, J. Kanakis, P. Malkaj, E. Dalas, J. Cryst. Growth 236 (2002) 363.

[2.6] E. Dalas, P. Klepetsanis, P.G. Koutsoukos, Langmuir 15 (1999) 8322.

[2.7] F. Manoli, E. Dalas, J. Cryst. Growth 218 (2000) 359.

[2.8] C. A. Orme, A. Noy, A. Wierzbicki, M. T. McBride, M. Grantham, H. H. Teng, et al. Nature 411 (2001) 775.

[2.9] *SMART, SAINT and XPREP*, Siemens Analytical X-ray Instruments Inc., Madison, Wisconsin, USA, 1995.

[2.10] G. M. Sheldrick, *SADABS: Empirical Absorption and Correction Software*, University of Gottingen, Institut fur Anorganische Chemieder Universitat, Gottingen, Germany, 1999.

[2.11] G. M. Sheldrick, *SHELXS-97*, University of Gottingen, Germany, 1997.

[2.12] L. J. Farrugia, J. Appl. Crystallogr. 30 (1997) 565.

[2.13] K. Nakamoto, Intrared and Ramman Spectra of Inorganic and Coordination Compounds. 5th Ed. John Wiley & Sons. Inc. New York, (1997).

[2.14] (a) E. Baeuerlein, Biomineralization: From Biology to Biotechnology and Medical Application. Wiley-VCH, Weinheim (2000).

[2.15] K. Gopal, Z. Lu, M. M. deVilliers, Y. Lvov, J. Phys. Chem. B 110 (2006) 2471.

[2.16] J. D. Currey, A. J. Kohn, J. Mater. Sci. 11 (1976) 1615.

[2.17] F. C. Meldrum, Int. Mater. Rev. 48 (2003) 187.

[2.18] S. Raz, O. Testeniere, A. Hecker, S. Weiner, G. Luquet, Biol. Bull. (Beijing) 203 (2002) 269.

[2.19] H. Colfen, Curr. Opini. Colloids Inter. Sci. 8 (2003) 23.

[2.20] A. L. Boskey, J. Cell. Biochem. Suppl. 30/31 (1998) 83.

[2.21] A.-W. Xu, Y. Ma, H. Colfen, J. Mater. Chem. 17 (2007) 415.

[2.22] J.R. Clarkson, T.J. Price, C.J. Adams, J. Chem. Soc. Faraday Trans. 88 (1992) 243.

[2.23] M. Menadakis, G. Maroulis, P.G. Koutsoukos, Comp. Mater. Sci. 38 (2007) 522.

[2.24] R. J. Reeder, G.M. Lamble, P.A. Northrup, Am. Mineral. 84 (1999) 1049.

[2.25] D. K. Keum, H. S. Na, K, Naka, Y. Chujo, J. Cryst. Growth 270 (2004) 655.

[2.26] C.G. Kontoyannis, N.V. Vagenas, Analyst 125 (2000) 251.

[2.27] A. J. Xiea, Y. H. Shena, C. Y. Zhangb, Z. W. Yuanb, X. M. Zhub, Y. M. Yang, J. Cryst. Growth 285 (2005) 436.

[2.28] (a) M. J. Plater, R. A. Howie, A. J. Roberts, Chem. Commun. (1997) 893, (b) Y. Y. Yang, Z. Q. Huang, L. Szeto1, W. T. Wong, Appl. Organometal. Chem. 18 (2004) 97.

[2.29] W. Schuckmann, H. Fuess, J. W. Bats, Acta Cryst. B34 (1978) 3754.

[2.30] M. P. Gupta, A. P. Saha, Ind. J. Phys. 53A (1979) 460.

[2.31] O. Sohnel, J. Garside, Precipitation: Basic Principles and Industrial Applications, Butterworth-Heinemann, Oxford, (1992) 145.

[2.32] H. Elfil, H. Roques, Desalination 137 (2001) 177.

Chapter - 3

Biogenic mineral growth modification in presence of High-Molecular-Weight matrix

3.1. High-molecular-weight acidic proteins as a crystal growth modifier.

Construction of modified inorganic mineral with controlled mineralization analogous to nature is a current interest for material chemists to seek industrial and technological applications. Morpho-synthesis strategies give access to a wide range of fascinating and useful crystalline meso or nano-structures. The remarkable range of morphologies exhibited by Ca and Ba minerals has inspired the biomimetic synthesis of inorganic materials with complex form [3.1]. A wide range of templating [3.2] methods exist for organizing inorganic materials at a wide range of length scales. This research is inspired by the fascinating mechanical and optical properties of minerals, their complex forms, and the exquisite control of crystallization over several length scales in mineralization processes [3.3]. The resulting biogenic minerals typically differ from geological or synthetic inorganic minerals in crystal size, shape, orientation, and crystalline structure, apparently defying the requirements of symmetry and thermodynamic stability inherent to the crystal lattice.

We were interested in exploring the utility of natural high-molecular-weight proteins as crystal growth modifier because the complex nanostructured biominerals that are supported by acidic proteins have excellent mechanical properties [3.4]. Citrus fruits (Lemon, Oranges, Mandarins, and Grapefruits etc.) are among the most widely produced fruits all over the world. Lemon (*Citrus Lemon*) contains various organic acids, along high molecular weight water-soluble proteins out of which 82, 63 and 46 kDa protein occurs exclusively in the lemon juice which are fully characterized [3.5]. The section describes the role of naturally occurring high-molecular-weight water-soluble acidic proteins of the lemon extract to regulate the crystal growth of some Ca and Ba minerals. Carboxylic acids are known to bind Ca^{2+} and Ba^{2+} ion that can potentially either nucleate the growth of a given mineral or interact strongly and specifically with growing crystal faces, thus altering the morphology of the crystals in a controlled fashion.

3.1.1. Experimental Section

Crystal Characterization

Scanning electron micrograph (SEM) images were obtained by means of a *LEO-1430 VP* electron microscope on samples glued on an aluminum stub and gold sputtered. FT-IR analysis was carried out on air-dried minerals samples. Because of the importance of knowing the polymorphs associated to crystalline structure, FT-IR measurements performed. All spectra recorded at 4 cm^{-1} resolution with 10 scan with a *Perkin Elmer-Spectrum One FT-IR Spectrometer* from 4000 to 400 cm^{-1}. A background spectrum was measured for pure KBr. To confirm the crystalline nature of the mineral sample PXRD data were recorded with *Seifert powder X-ray diffractometer (XRD 3003TT)* with CuK$_\alpha$ source (λ = 1.54 Å) on glass surface of air-dried sample. In order to determine presence of organic matrices, water of crystallization and nature of polymorphs in the obtained mineral crystals, the samples were analyzed thermally from 25 to 600 °C using a *DT-40 thermal analyzer*. The temperature was increased at a rate of 2 °C/min. The calcium binding affinity of the protein mixtures present in LAB extracts was analyzed using dynamic light scattering (DLS) instrument (HORIBA LB-550, Japan).

Extraction of acidic high-molecular-weight proteins from Lemon

The freeze-dried lemons (*Citrus Limon*) were divided into peel and edible part. The edible part, which consisted of juice sac and segment epidermis, was grounded and extracted with minimum known amount of Milli-Q water. The extract was filtered initially through high vacuum suction pump using 2.0 µm filter, the filtrate was centrifuged at 10,000 rpm for 20 min to get a transparent colorless solution. After that the clear colourless solution was dialyzed against water using a 12,000 MWCO dialysis bag (Sigma, USA) to remove all the lower molecular weight components (<12 kDa) leaving behind only the water soluble high-molecular-weight proteins as shown in scheme 3.1. The protein content, estimated by the standard Bradford method [3.6] was found to be 45.7 µg /ml. Standard acid base titration allowed us to measure the acid contents of the protein extract and was estimated to be 0.5 M. This extract was used further for mineralization experiments.

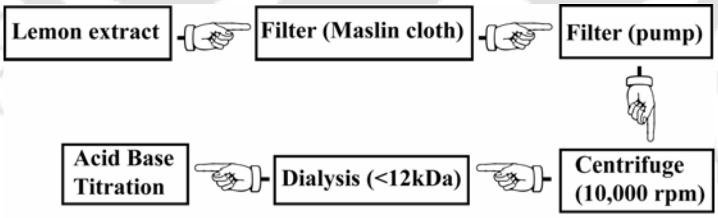

Scheme 3.1. Extraction of high-molecular-weight protein from lemon pulp extract.

Crystallization Experiments

The reaction systems divided into two different groups: Milli-Q water system (control) and high-molecular-weight protein solution from Lemon extract. The negative control conditions consisted of no added protein solution. In a typical experiment, 5 x 10^{-4} M protein solution from lemon extract mixed with 0.001 M $CaCl_2$ / $BaCl_2$ solution in Milli-Q water and kept at RT for 12 hrs without stirring. Then 0.001 M Na_2CO_3 solutions were added very slowly without much mechanical disturbance. Two parallel experiments performed simultaneously for each mineral. The solutions kept at 25±2 °C for several days without any mechanical disturbance. When there was a large number of crystals present in the reaction vessel, the crystalline products were collected, vacuum-filtered and washed with Milli-Q water several times to remove the organic additives and then finally with anhydrous ethanol. The crystals dried in air for 24 h and kept in desiccators before analysis.

3.1.2. Results and Discussions

High-molecular-weight acidic proteins from Lemon extracts act as a polymeric acidic organic growth modifier, which initially forms a weak and flexible complex with the Ca^{2+} / Ba^{2+} ions. Addition of anions (*viz.* CO_3^{2-}, SO_4^{2-} etc.), which can coordinate strongly to the Ca^{2+} / Ba^{2+}, reorganizes the structure of the whole complex at the molecular level. The reorganization processes depends on the chemical nature of the anions as well as their bonding interactions with the loosely bound Ca^{2+} / Ba^{2+} ion. This reorganized labile complex in turn acts as a nucleus for the crystal growth. The following sections shows crystal nucleation and growth of a few Ca and Ba minerals in aqueous solution of proteins extracted from lemon.

Crystallization of Calcium Carbonate

The crystal formation in the solution can be observed as an increase in the turbidity of the solution with time. Crystallization of $CaCO_3$ in the presence of high-molecular-weight acidic proteins from lemon extracts resulted in the formation of perfect hollow sphere of average diameter of 9 µm (Figure 3.1a). Closer look at the structure revealed that each of the micron scale sphere is made out of $CaCO_3$ nano-spheres (Figure 3.1b), which are nothing but calcite spherulites. The presence of the only Calcite polymorph (PDF No. 01-086-2342) in highly crystalline bulk sample was confirmed by PXRD analysis (Figure 3.1c). Characteristic FT-IR bands corresponding to calcite crystal found to be at 1080, 879 and 706 cm^{-1} [3.7]. When we performed the time dependent FT-IR analysis (Figure 3.1d) of calcite spherulite formation, after 5 minutes we got two characteristic humps (1425 cm^{-1} and 1385 cm^{-1}) corresponds to amorphous calcium carbonate (ACC). The presence of these characteristic humps became smaller after an hour and diminishes completely after 2hrs. Hence, it can conclude that the formation of calcite spherulite is via formation and expense of metastable ACC. This result also supports the Ostwald's rule [3.8] which states that, the least stable phase with the highest solubility is formed preferentially in the solution, and then transformed within a few minutes to thermodynamically most stable polymorph. The sizes of the $CaCO_3$ nano-spheres are found to be in the range 100 – 350 nm from the particle size distribution plots and most of the spherical crystallites are of the size of 150 nm (Figure 3.2a). TGA analysis shows the loss of one molecule of CO_2 at 750 ^{o}C and DSC analysis shows an endothermic peak centered around 750 ^{o}C corresponding to the removal of one mole CO_2 (Figure 3.2b).

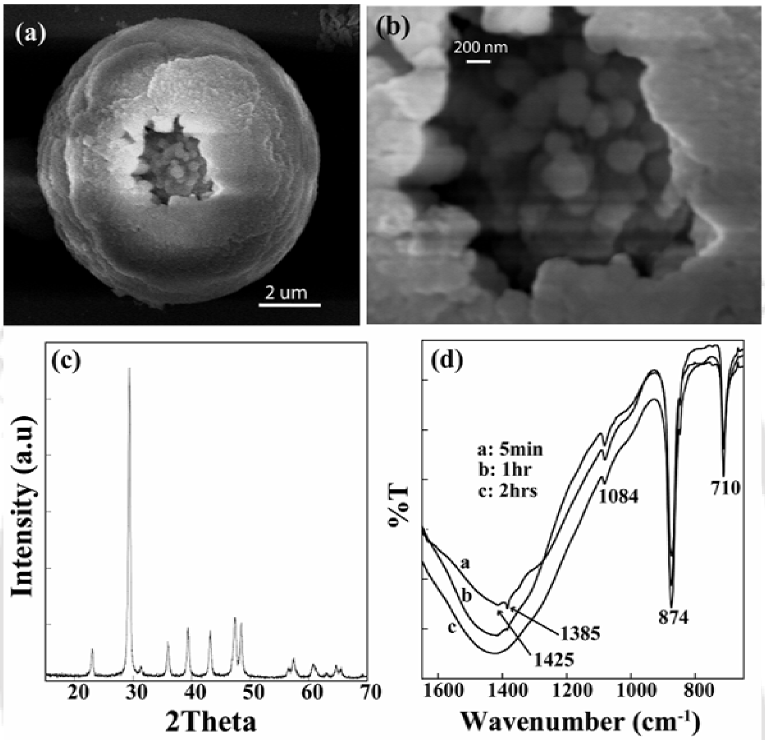

Figure 3.1. SEM micrographs of (a) hollow spherulitic Calcite, (b) Calcite nano-spherulites, (c) PXRD pattern of Calcite crystals and (d) time dependent FT-IR analysis of spherulitic Calcite formation.

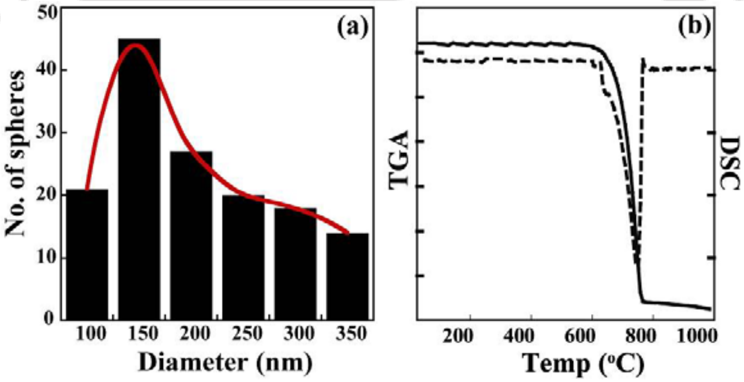

Figure 3.2. (a) Particle size distribution plot and (b) TGA-DSC plot of Calcite crystals.

Crystallization of Calcium Sulfate

Calcium sulfate form plate-like structures (Figure 3.3a) from high-molecular-weight acidic protein from lemon pulp extract. These thinner plates are very fragile compare to that of earlier one from lemon extract. The crystal phase is confirmed to be Gypsum ($CaSO_4$. $2H_2O$) (PDF No. 01-076-1746) by PXRD pattern (Figure 3.3b).

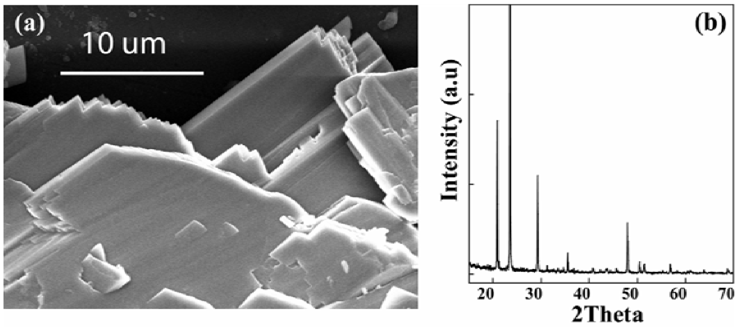

Figure 3.3. (a) SEM micrograph of Gypsum plates from in high-molecular-weight acidic proteins from lemon extract and (b) PXRD pattern of Gypsum crystals.

FT-IR spectrum shows the ν_3 band at 1150 cm^{-1} (ν_s) and ν_4 bands at 666 cm^{-1} (s), 600 cm^{-1} (s) corresponds to the SO_4^{-2} ion [3.9] (Figure 3.4a). The average average thickness of the $CaSO_4$. $2H_2O$ was found to be 200 nm from the particle size distribution plots (Figure 3.4b). TG analysis shows removal of two water molecules between the ranges of 100°C to 160°C, loss of 20.98% (calculated 20.93%), which is in good agreement with the gypsum structure. The DSC-plot shows an endothermic peak at 150°C due to the release of water molecules (Figure 3.4c).

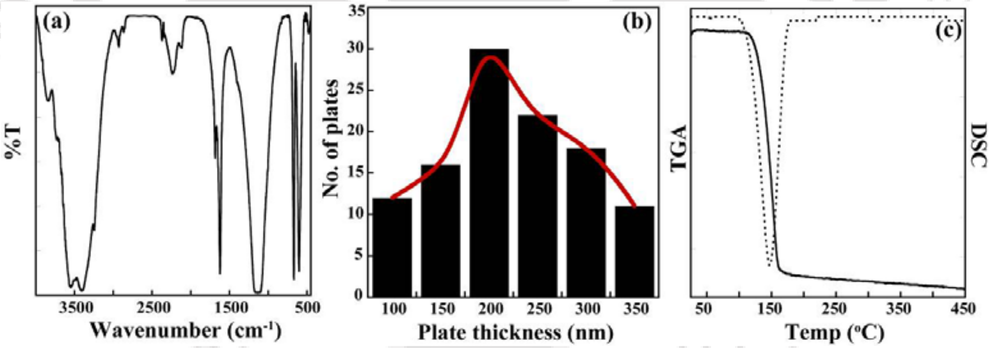

Figure 3.4. (a) FT-IR spectrum, (b) Particle size distribution plot and (c) TGA-DSC plot of Gypsum crystals.

Crystallization of Calcium Oxalate

Calcium oxalate crystals take the shape of rhombohedral plates (Figure 3.5a) in proteins extracted from lemon. The plates are more elongated in the length. The PXRD pattern (Figure 3.5b) confirms the crystal phase to be Whewellite (PDF No. 01-077-1160), CaC_2O_4. H_2O. FT-IR analysis shows peaks at 1618, 1325, 783, 665, 517 cm^{-1} characteristics of coordinate oxalate ion and calcium oxalate monohydrate (COM) [3.9] (Figure 3.6a). The thickness of these plates is in the range of 0.6 – 0.9 µm and maximum

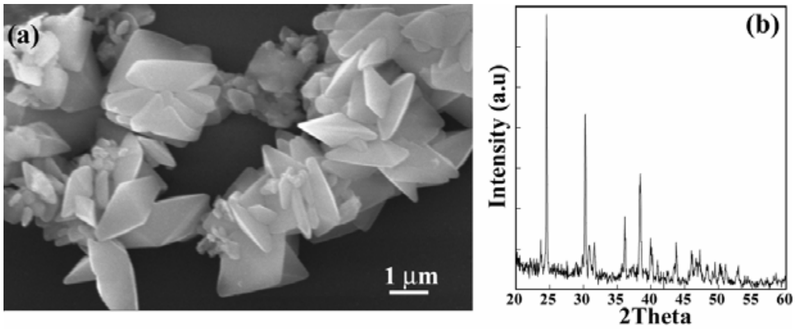

Figure 3.5. (a) SEM micrograph of Whewellite from proteins extracted from lemon and (b) PXRD pattern of Whewellite crystals.

plates have thickness of 0.8 μm (Figure 3.6b). TG analysis shows two sequential loss of 12.40% (calculated 12.32%) and 22.74% (calculated 21.87%) in the range of 120°C to 200°C and 400°C to 520°C respectively, which corresponds of the removal of one H_2O and one CO molecules. The residual mass corresponds to the $CaCO_3$. DSC profile shows an endothermic peak at nearly 180 °C and another exothermic peak at 480°C (Figure 3.6c).

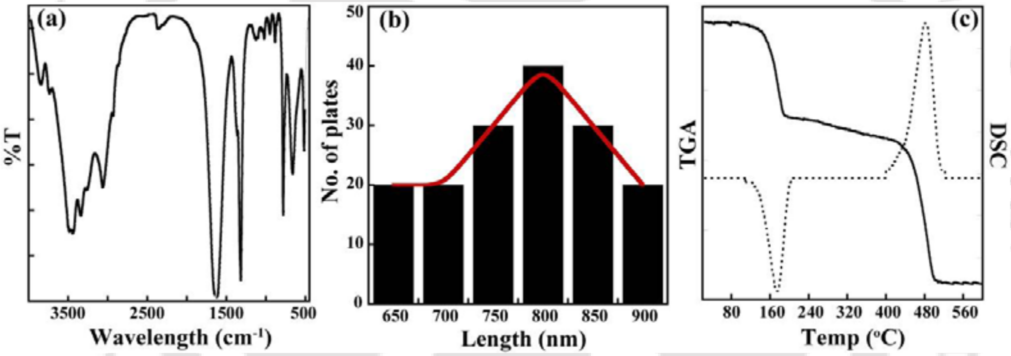

Figure 3.6. (a) FT-IR spectrum, (b) Particle size distribution plot and (c) TGA-DSC plot of Whewellite crystals.

Crystallization of Calcium Hydrogen Phosphate

Calcium hydrogen phosphate form elongated rods of length in the range of 8 – 10 μm (Figure 3.7a and 3.7b) proteins from lemon extract. PXRD pattern confirm the crystal phase to be Brushite, $CaHPO_4.\ 2H_2O$ (PDF No. 01-072-0713) (Figure 3.7c). FT-IR analysis shows a broad band centered around 3450 cm^{-1} is due to intermolecular and weakly H bonded OH because of water of crystallization [3.10] (Figure 3.8a). The weak absorptions at 2375 cm^{-1} is due to HPO_4^{2-} [3.11]. The H-O-H bending gives rise to absorption at 1651 cm^{-1}. The absorptions at 1210 and 1140 cm^{-1} are due to P = O associated stretching vibrations. Whereas, the absorption at 1068 cm^{-1} is due to P = O stretching vibrations. The P-O-P asymmetric stretching vibrations give rise to absorptions at 987 and 874 cm^{-1}. The absorptions at 577 and 525 cm^{-1} are again due to acid phosphates. Particle size distribution plot reveals that the average thickness of these rods is 150 nm (Figure 3.8b). The TG analysis shows that hydrated calcium phosphate becomes anhydrous at 287ºC, loss of 21.1% (calculated 20.9%), thereafter, at 540ºC it turns into calcium pyrophosphate ($Ca_2P_2O_7$) with loss of 7.0% (calculated 6.6%). DSC analysis shows an endothermic peak and an exothermic peak respectively (Figure 3.8c).

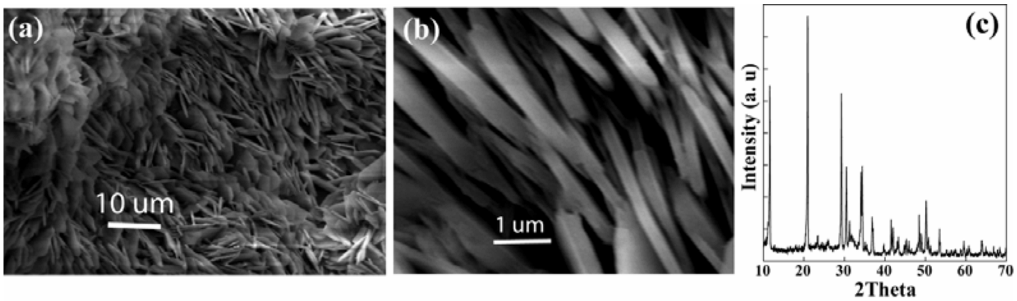

Figure 3.7. SEM micrographs of (a) Brushite micro rods, (b) higher magnifies image and (c) PXRD pattern of Brushite crystals.

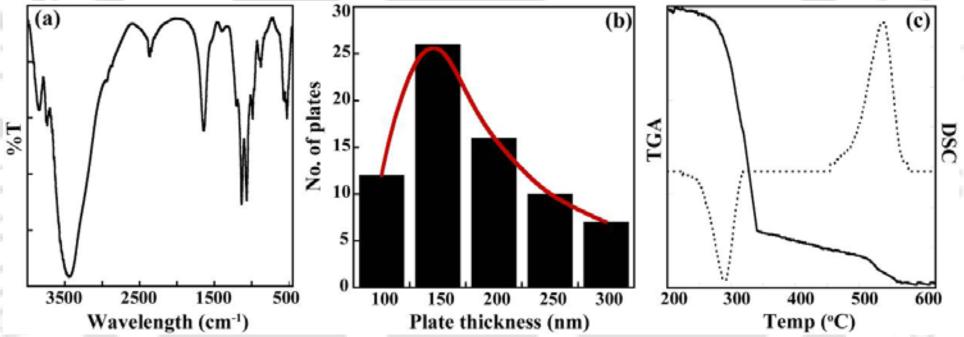

Figure 3.8. (a) FT-IR spectrum, (b) Particle size distribution plot and (c) TGA-DSC plot of Brushite.

Crystallization of Barium Carbonate

Barium Carbonate forms plates of average thickness of 100 nm within one day (Figure 3.9a) in proteins extracted from lemon. These plates have a common point of origin. Mature crystals form a beautiful flower like structure (Figure 3.9b) in ten days.

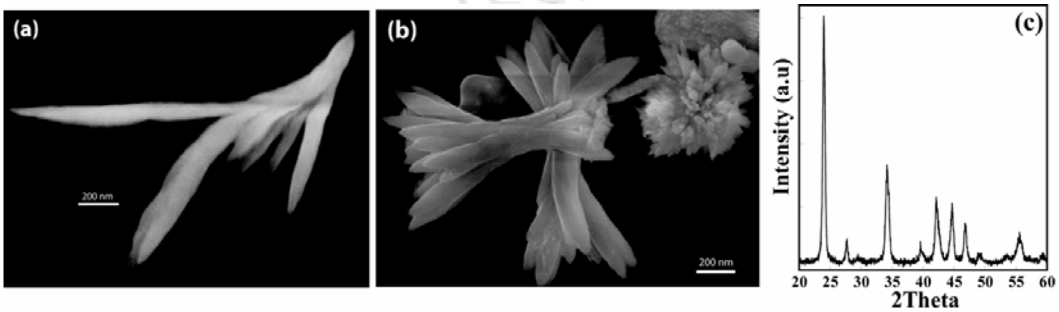

Figure 3.9. SEM micrographs of (a) Witherite plates after 1 day, (b) Witherite plates after 10 days and (c) PXRD pattern of Witherite.

The petals are made of plates of thickness range 200 – 250 nm. PXRD pattern shows that product is crystalline in nature and phase of the mineral is found to be as Witherite (PDF No. 01-071-2394) (Figure 3.9c). Characteristic stretching frequencies of Witherite are found to be 1450(υ_3), 1063(υ_1), 680 (υ_4) cm^{-1} in FT-IR spectra (Figure 3.10).

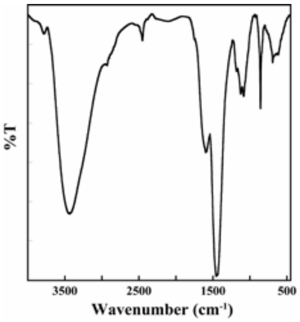

Figure 3.10. FT-IR spectrum of Witherite crystals.

Crystallization of Barium Sulphate

Barium Sulphate forms seed like structure having average size in the range 0.30 – 0.45 µm (Figure 3.11a). PXRD pattern confirms the mineralogical phase to be Barite (PDF No. 01-089-7357) (Figure 3.11b). FT-IR spectrum shows υ_3 band at 1110 and 1085 cm^{-1} and υ_4 band at 640 and 660 cm^{-1} corresponding to sulphate (Figure 3.11c).

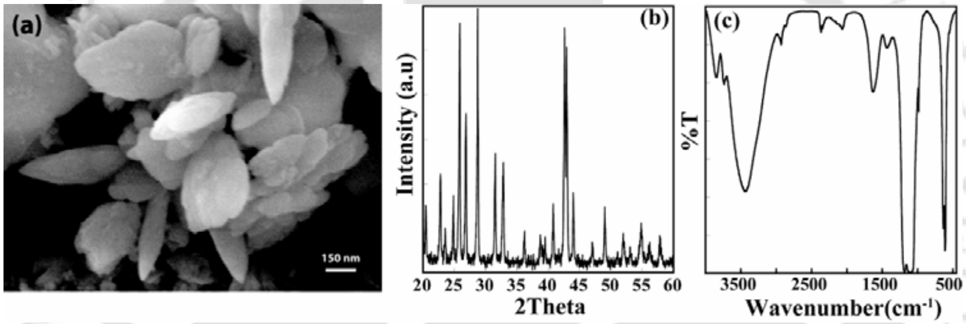

Figure 3.11. (a) SEM micrograph, (b) PXRD pattern and (c) FT-IR spectrum of Barite crystals.

Crystallization of Barium Oxalate

Barium Oxalate crystals agglomerate into spheres of varying dimensions (Figure 3.12a) from protein extracted from lemon. High-resolution image shows that these spheres are made with rods of 0.30 µm in thickness (Figure 3.12b). PXRD pattern confirms the phase to be as Barium oxalate hemi hydrate *i.e.* $Ba(C_2O_4)$. 0.5 H_2O (PDF No. 00-020-0134) (Figure 3.12c).

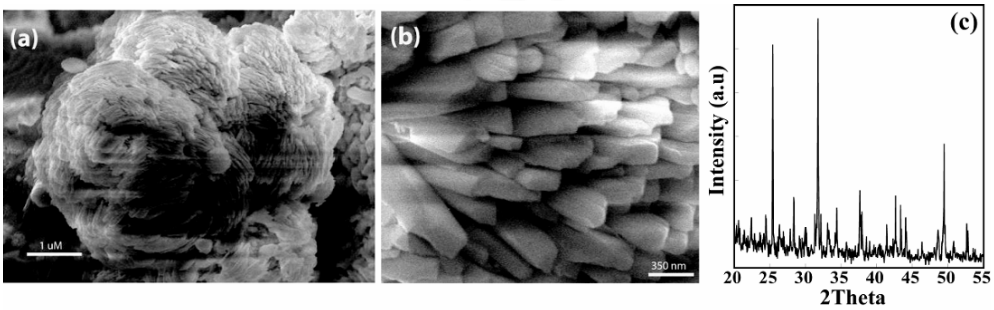

Figure 3.12. SEM micrograph of (a) Ba-oxalate in proteins extracted from lemon, (b) Ba-oxalate nano rods and (c) PXRD pattern of Barium oxalate hemi hydrate.

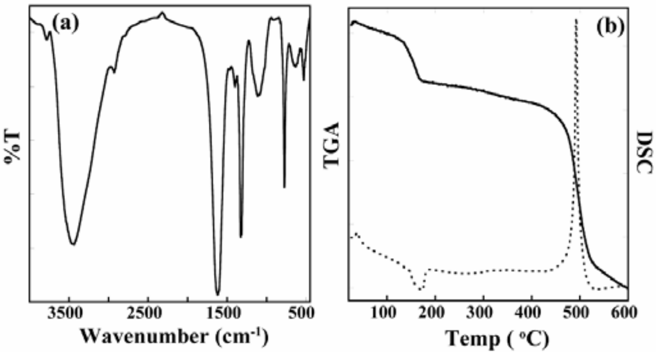

Figure 3.13. (a) FT-IR spectrum and (b) TGA-DSC plot of Barium oxalate hemi hydrate.

FT-IR analysis shows the presence of peaks at 3590, 1620 (υ_a), 1320 (υ_s), 840, 720 cm^{-1} which are the characteristics of coordinated oxalate ions and barium oxalate hemi hydrate [3.9] (Figure 3.13a). TG analysis shows two sequential loss of 4.01% (calculated 3.84%) and 13.12% (calculated 12.43%) in the range of 120^{o}C to 160^{o}C and 440^{o}C to 520^{o}C respectively, which corresponds of the removal of 0.5 H_2O and one CO molecules, which is in good agreement with the $Ba(C_2O_4)$. 0.5 H_2O structure. The residual mass corresponds to the $BaCO_3$. DSC profile shows an endothermic peak at nearly 160^{o}C and another exothermic peak at 490^{o}C (Figure 3.13b).

Crystallization of Barium Phosphate

In proteins extracted from lemon, barium phosphate plates agglomerates into spheroids (Figure 3.14a) with average length of 0.80 μm. PXRD pattern shows that the phase of the mineral is found to be as Barium Hydroxide Phosphate [$Ba_5(OH)(PO_4)_3$] (PDF No. 00-001-0811) (Figure 3.14b). The FT-IR analysis shows characteristic stretching frequencies of barium phosphate are at 3550, 1065, 980, 880 cm^{-1} corresponding to the OH^- and phosphate ion respectively (Figure 3.14c).

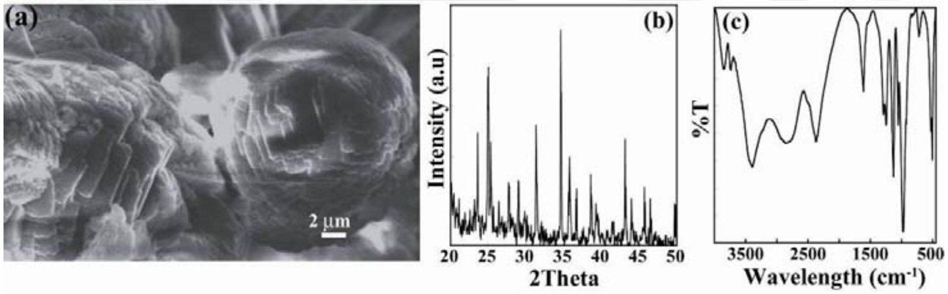

Figure 3.14. (a) SEM micrograph, (b) PXRD pattern and (c) FT-IR spectrum of Barium Hydroxide Phosphate.

Effect of the cation concentration

Five different solutions were made of 0.5, 0.1, 0.01, 0.001 and 0.0001 M of $CaCl_2$ (or $BaCl_2$) and corresponding concentration of counter anions for these experiments. It was observed that when the concentration was high, immediate precipitation took place without any modification on the crystal morphology. Formation of labile complex with bio-macromolecules does not take place. Crystallization was so fast that it was difficult to clearly distinguish between processes occurring during nucleation, growth and ripening stages. As we decrease the concentration, formation of the minerals took more time but crystal nature become more prominent. Best result was obtained in 0.001 M $CaCl_2$ / $BaCl_2$ and the counter anions concentrations.

Effect on the Sequence of addition

To see the effect on the sequence of addition on the crystal morphology, reverse addition was done. It is speculated that calcium ion forms a weak complex with the acidic organic matrix, which in turn acts as a flexible nucleus. Addition of counter anion *i.e.* CO_3^{2-} before the cation does not help to form the nucleus. In the reverse addition experiment, after a week, it was observed that a thick emulsion was formed instead of amorphous and/or crystalline materials. After washing couple of times with Milli-Q water, thick paste remains, which forms lumps of solid after drying in desiccators (Figure 3.15).

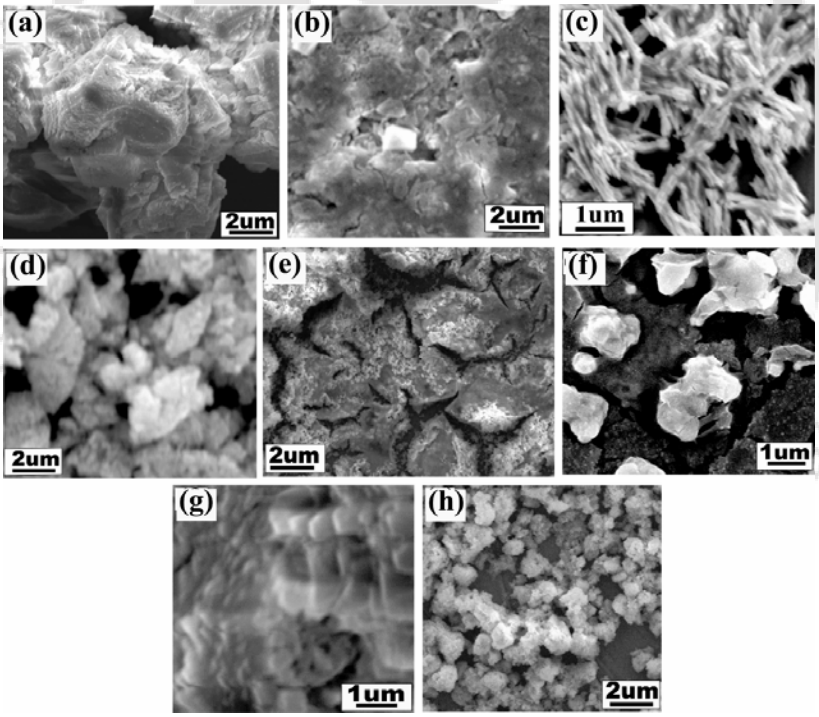

Figure 3.15. SEM images of (a) Calcite, (b) Gypsum, (c) Whewellite, (d) Brushite, (e) Witherite, (f) Barite, (g) Ba-oxalate and (h) Barium Hydroxide Phosphate reverse addition.

3.1.3. Summary

In summary, biological macromolecules (mass > 12 kDa) from the lemon extract act as a soluble organic additive and influence the growth of the minerals. An extensive study of this matrix in the crystallization of common calcium as well as barium minerals has been tested. Here we have also demonstrated the role of an amorphous precursor phase in biomineralization, and time dependent formation of spherulitic $CaCO_3$ structures via a one pot solution route, in which amorphous microparticles in the presence of a small amount of acidic macromolecules are sequentially transformed into thermodynamically stable hollow calcite spherulite. Moreover, understanding the formation mechanism of the remarkable architecture should develop chemistry for manufacturing micron- and nanoscale functional materials in solution systems. Large-scale preparation of these materials is now in progress in our laboratory.

3.2. Lactic Acid Bacterial (LAB) extract as a growth modifier of minerals

Biomineralization is a universal and well documented geological phenomenon among living systems (*e.g.* egg and mollusk shells sponge spicules, pearls, corals, bones, and teeth) [3.12]. Proteins secreted by living organisms accumulate or induce the formation and precipitation of various inorganic compounds such as phosphates, carbonates and silicates [3.13]. The formation of minerals and mechanisms by which bacteria could control the formation of minerals in natural habitats is now of current interest for material scientists to have an insight of the mechanism of *in vivo* mineralization, as well as to seek industrial and technological applications.

Bacterial biomineralization is a diverse and widespread phenomenon that results from cellular mediated physiological process. Since the beginning of the century it has been known that bacteria are involved in the formation of carbonates and natural phosphate deposits [3.14]. Among the biominerals precipitated by bacteria, the carbonates have gained great importance, especially due to the large number of species being able to precipitate them. $CaCO_3$ precipitation is a widespread phenomenon in bacteria, since, under suitable conditions, all bacteria can form crystals of calcium carbonate. Secondly, the role of bacteria in the precipitation of carbonates in different natural habitats (soils, freshwater and saline habitats) has been established [3.15]. It has been suggested that this precipitation could be related to the formation of marine calcareous skeletons, carbonate sediments and deposits of carbonates in soils [3.16]. The mechanisms involved in the bacterial mediation are, however, still debated. Biologically induced mineralization is the dominant process among bacteria, with biominerals commonly generated as secondary events from interactions between the activity of the microorganisms and their surrounding environment [3.17]. Lactic acid bacteria (LAB) enjoy a GRAS (generally regarded as safe) status and have been reported to have many beneficial effects on human health. LABs have also been used to study the formation of gold, silver and gold-silver alloy crystals and it was shown that the crystals accumulate within the cells [3,18].

We report here the crystal growth modification of some common biologically important calcium and barium minerals in presence of homogenous high molecular weight protein extract secreted from three different LAB strains *viz*. *Lactobacillus plantarum* MTCC 1325, *Lactobacillus acidophilus* MTCC 4495 and *Pediococcus acidilactici* CFR K7 grown in MRS (deMan, Rogosa and Sharp) medium at room temperature. To the best of our knowledge, this is the first report on the formation different micron-scale to nano architecture of minerals using the high molecular weight secreted protein from the LAB strains. The influence of these bacterial extracts on the crystallization behavior was investigated in details to test the basic coordination behavior of the acidic protein. In this report, varied architecture of the mineral crystals obtained in presence of high molecular weight protein extracts of three different LAB strains has been discussed. The role of native form of high molecular weight bacterial protein extracts in the generation of nucleation centers for crystal growth was clearly established. A model for the formation of organic matrix-cation complex and the subsequent events leading to crystal growth is proposed. Synthesis of high purity $Ca(OH)_2$ achieved from the calcite crystal via the formation of CaO.

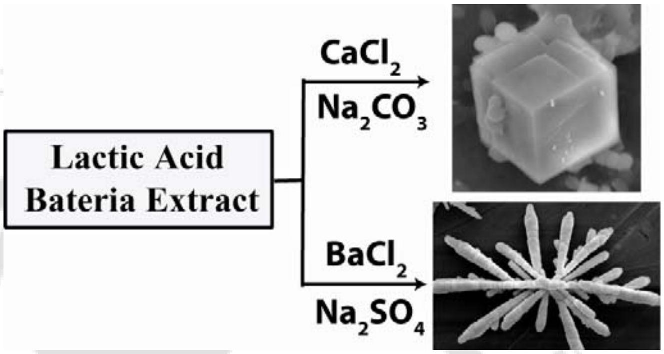

Scheme 3.2. Growth modification of calcium and barium minerals in presence of high-molecular-weight acidic proteins extracted from LAB strains.

3.2.1. Experimental Section

Bacterial strains and materials

All the metal salts used were analytically pure. In all the experiments ultra pure Milli-Q water was used. Reference strains of LAB used in the present investigation are Lactobacillus plantarum MTCC 1325, Lactobacillus acidophilus MTCC 4495 (from Microbial Type Culture Collection Centre, Chandigarh, India) and Pediococcus acidilactici CFR K7 [3.19]. The strains were stored as 10% milk-glycerol stocks at -20°C and subcultured every fortnight. LAB strains were grown in deMan, Rogosa and Sharpe (MRS) medium (HiMedia, Mumbai, India) at 37°C under static condition for 16 h and used as inoculum for subsequent experiments.

Preparation of protein extract for mineralization experiments

Stock cultures of *Pediococcus acidilactici* CFR K7, *Lactobacillus plantarum* MTCC 1325 and *Lactobacillus acidophilus* MTCC 4495 were grown in 5 ml MRS medium and incubated at 37°C under static condition for 16h. The strains were reinoculated at 1% level into 50 ml MRS medium and incubated at 37°C for 48 h. The cells were separated in a refrigerated centrifuge (Sigma 3K30, Germany) set at 8000 rpm for 5 minutes at 4°C. The cell free supernatant (CFS) was collected. A 5.0 ml aliquot of the cell free supernatant (CFS) from CFR K7, MTCC 1325 and MTCC 4495 cultures was extensively dialyzed against water using a 12,000 MWCO dialysis bag (Sigma, USA). Dialysis removed all the lower molecular weight components such as organic acid *i.e.* primarily lactic acid and all other organic and inorganic components retaining only the water-soluble high molecular weight proteins (Scheme 3.3). This extract was used further for mineralization experiments. The protein content, estimated by the standard Bradford method [3.20] in the MTCC 1325 and CFR K7 extract was found to be 7.2 µg/ml and 7.8 µg /ml respectively. Standard acid base titration allowed us to measure the acid contents of the protein extract. Protein profile of dialyzed CFS was analyzed by SDS-PAGE.

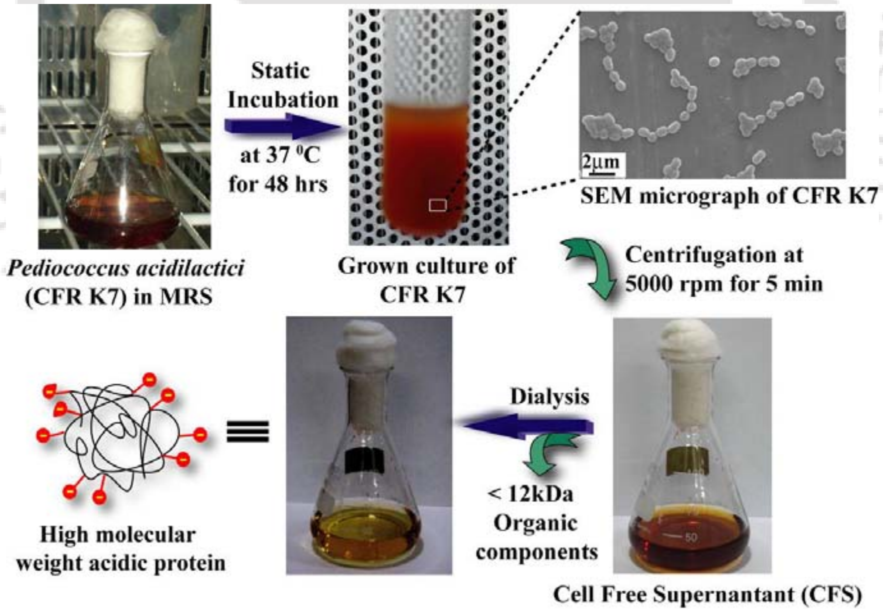

Scheme 3.3. Extraction of high-molecular-weight acidic proteins from CFR K7 in MRS.

Protein profile of dialyzed CFS

A 250 µl aliquot of the dialyzed CFS was lyophilized (Alpha 1-4 LD, Christ, Germany). The sample was resuspended in 25 µl of sample loading buffer (12 mM Tris-HCL pH 6.8, 5% glycerol, 0.4% SDS, 2.88 mM 2-mercaptoethanol, 0.02% bromophenol blue) and subjected to electrophoresis on a 10% SDS-polyacrylamide gel. Dialyzed and freeze-dried MRS medium was used as control. The protein bands were visualized by staining the gel in Coomassie Brilliant Blue R 250 solution. The molecular weight of the proteins was estimated by comparing the mobility with a molecular weight standard marker. (Bangalore Genei, Bangalore, India). The number of protein bands obtained for CFR K7 was more compared to MTCC 1325 probably indicating that the strain CFR K7 bears efficient secretion machinery and excretes larger number of extracellular proteins following 16 h of growth.

Mineralization in the presence of LAB extract

In a typical experiment, $1x10^{-3}$ N (concentration determined from acid-base titration) LAB extract was mixed with 0.001 M $CaCl_2$ / $BaCl_2$ solution in Milli-Q water and kept at RT for 12 hrs without stirring. Then 0.001 M Na_2CO_3 solution was added intermittently for a period of 6 hrs without much mechanical disturbance. Control reactions were also setup with only water, with lactic acid and MRS medium, respectively, devoid of the LAB culture for each combination of cation and anion. Three more parallel experiments were performed simultaneously with solution of other counter anions *viz.* Na_2SO_4, $Na_2C_2O_4$ and Na_2HPO_4 respectively. The solutions were kept at 25±1 °C for several days without any mechanical disturbance. When there was a large number of crystals present in the reaction vessel, the crystalline products were collected, vacuum-filtered and washed with Milli-Q water several times to remove the organic additives and then finally with anhydrous ethanol. The crystals were air dried for 24 h and kept in desiccators before analysis.

Sample preparation for dynamic light scattering

The calcium binding affinity of the protein mixtures present in LAB extracts was analyzed DLS. The protein mixture-Ca^{2+} solutions contained stoichiometric ratios of protein to Ca^{2+}, with a protein concentration of 0.072 mg/ml and 0.1-0.6 mM Ca^{2+} ion. Solutions of LAB extracts without the addition of Ca^{2+} ion were used as control. Samples were loaded into 20 ml quartz cuvette, and then placed into the dynamic light scattering instrument (HORIBA LB-550, Japan). The instrument performance was calibrated by measuring the DLS of standard suspensions of polystyrene bead (R_H=68 nm). Approximately 100 measurements were collected for each of three to four independently prepared samples at 25°C. The measuring range was from 1 nm to 6 µm, and the light source was a 650-nm Laser diode of 5 mW. The data was analyzed to obtain the hydrodynamic radius (R_{H}) values for each sample. The reported R_{H} values are the mean size of the dominant peak. The temperature during all the measurements was kept fixed at 30^{o}C. These measurements were calibrated against reference polystyrene beads with R_H=68 nm. However, measurement of standard suspensions of polystyrene beads revealed a diameter of 72 (±0.14%) nm. This indicated the error range of the instrument performance is around 6%.

3.2.2. Results and Discussions

In this section we have proposed and experimentally verified that high molecular weight (> 12kDa) acidic proteins secreted by different LAB strains act as soft, flexible nucleation centre for the mineralization of some common calcium and barium minerals (Scheme 3.4). They also inhibit crystal growth by binding to the growth sites of the crystal. For crystallization, the ions that will form the crystal lattice must come together with the right orientation to form a stable structure. This stable structure resembles the crystal phase being deposited [3.21]. The crystal morphology depends on the differences of the crystal faces in surface energy and external growth environment. The surface energy of a crystal face can be lowered by the adsorption of an additive. Although LABs are not related to biological mineralization processes, however, as the acidic proteins are known to form matrix for biomineralization, we have tested these fundamental coordination aspect with acidic LAB extracts.

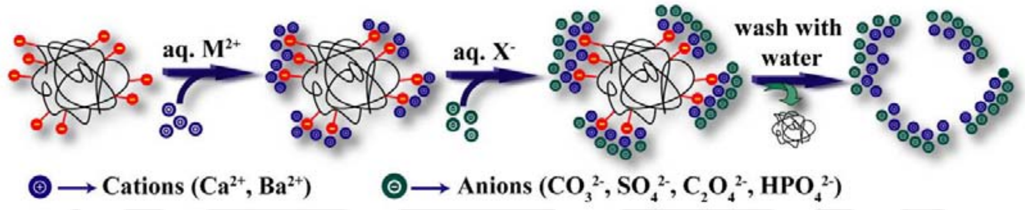

Scheme 3.4. Proposed mechanism of template action of protein extract.

Analysis of protein profile of dialyzed CFS

To check the purity of the protein extract and the nature of the proteins CFS was analyzed by SDS-PAGE. Protein bands from MRS medium alone were not visualized in lane 4 (Figure 3.16) indicating that the bands obtained in lane 2 (CFR K7) and lane 3(MTCC

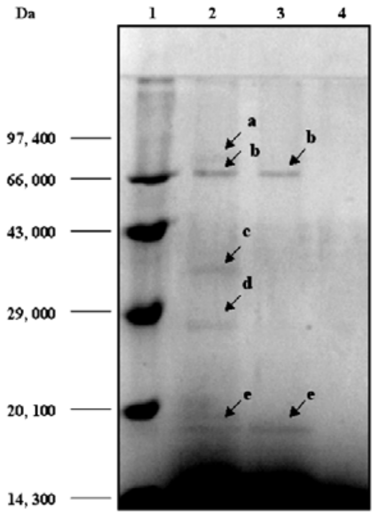

Figure 3.16. SDS-PAGE analysis of proteins present in dialyzed CFS of LAB cultures. Lane 1: Molecular weight standard marker proteins (Bangalore Genei, India); Lane 2: *Pediococcus acidilactici* CFR K7; lane 3: *Lactobacillus plantarum* MTCC 1325; Lane 4: MRS medium.

1325) were indeed secreted by LAB strains and not contributed from the media. The protein profile obtained from CFR K7 included closely migrating proteins having high molecular mass of 80, 70 kDa (bands a and b) and additional proteins of approximately 37, 21.0 and 10 kDa respectively (bands c-e). Interestingly, the 70 and 10 kDa protein bands were also seen for strain MTCC 1325. Presumably, both these proteins are secreted proteins commonly encountered in LAB strains.

Effect of concentration of organic matrix

To examine the effect of acid concentration of the organic matrix on the crystallization, experiments were perform at concentration range of 0.0015 (without dilution), $1.5\text{x}10^{-4}$, $1.5\text{x}10^{-5}$ and $1.5\text{x}10^{-6}$ M of bacterial extract from CFR K7. At lowest concentration ($1.5\text{x}10^{-6}$ M) bulk amorphous precipitate of $CaCO_3$ form instantly without any definite structures. Formation of a weak organic matrix-metal ion complex is necessary for the nucleation to start (Scheme 3.4). Presumably extremely low concentration of organic matrix is sub-optimal and thus precludes the nucleation for subsequent crystal growth. On the other hand, solution having highest concentration (0.0015 M) took a relatively long time to form any visible crystalline materials and very less amount of product was obtained even after sufficient incubation time. This is because all the studied minerals are soluble in acidic medium, wherein crystal formation is inhibited. Concentration of $1.5\text{x}10^{-4}$ M gives best results. The experiment was repeated with other counter anions *viz*: SO_4^{2-}, $C_2O_4^{2-}$ and HPO_4^{2-} and the result followed the same trends. Similarly experiments were repeated with other LAB extracts. In the crystallization experiment, at the onset of nucleation, the entire solution was centrifuged for 5 min at 5000 rpm. A white colored amorphous pellet was obtained and clear supernatant indicate the complete precipitation of the mineral formed in the solution. Sedimentation of soluble proteins is possible only by ultra-centrifugation. Hence, at the speed employed, uncoordinated proteins remained in the solution. The pellet was re-suspended in buffer, and protein content was estimated using the Bradford method. The estimation revealed that 65% of protein was incorporated in the pellet and the remaining 35% was left in the supernatant as uncoordinated protein. These results support the formation of weak complex in the nucleation stage as proposed in Scheme 3.4.

Effect of the ion concentration

Five different concentrations: 0.5, 0.1, 0.01, 0.001 and 0.0001 M of Ca^{2+}/Ba^{2+} and corresponding concentration of counter anions was used in $1.5\text{x}10^{-4}$ M CFS. At high

Ca^{2+}/Ba^{2+} concentration immediate precipitation took place without any crystal growth modification. Formation of labile protein-metal ion complex did not take place because of the rapid formation of water insoluble compound. Hence, it was difficult to clearly delineate the processes occurring during nucleation, growth and ripening stages. As the concentration of cations decreased, formation of the minerals took more time but crystal morphology became more prominent. Best result was obtained in 0.001 M $CaCl_2$ / $BaCl_2$ and counter anions concentrations.

Influence of ions addition sequence

To study the effect of the sequence of ion addition on the crystal morphology, counter anion was added prior to cation in CFS. In scheme 3.4, it is proposed that Ca^{2+}/Ba^{2+} ion forms a weak complex with the acidic organic matrix, which in turn acts as a flexible nucleus. Addition of anion prior to cation does not help to form the nucleus. In the reverse addition experiment, after a week, it was observed that a thick emulsion was formed instead of amorphous and/or crystalline materials. After washing couple of times with water, thick paste remains, which forms solid lumps after drying in vacuum. This observation also supports our proposed hypothesis as depicted in Scheme 3.4.

Formation of protein-metal ion complex

In solution, dynamic light scattering is a method for measuring particle size distribution (PSD) in the submicron range [3.22].

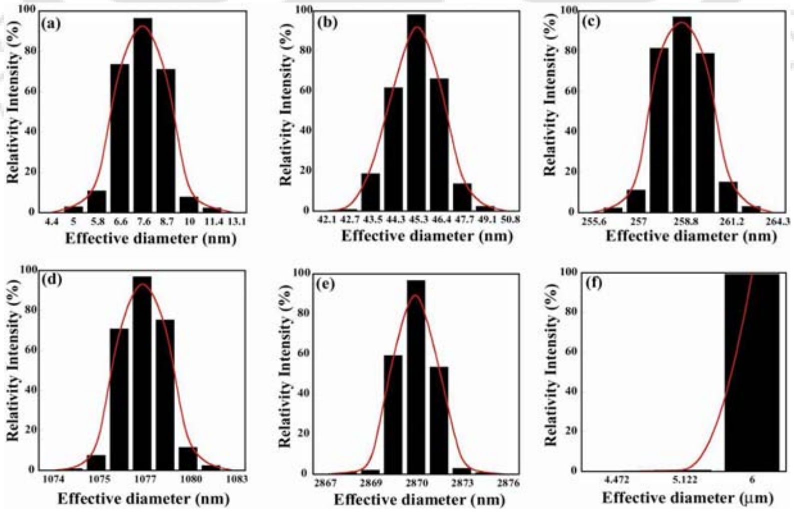

Figure 3.17. Particle size distribution of secreted protein extracts from *L. Plantarum* MTCC 1325. (a) Protein extract only, (b) protein extract + 0.1 mM Ca^{2+} ion, (c) protein extract + 0.2 mM Ca^{2+} ion, (d) protein extract + 0.35 mM Ca^{2+} ion, (e) protein extract + 0.5 mM Ca^{2+} ion and (f) in presence of large excesses of Ca^{2+} ion.

Table 3.1. DLS results of CFR K7 LAB extract with Ca^{2+} ion.

Sr. No.	Condition	Average radius
1	Only protein extract	10 nm
2	protein Extract + 0.1 mM Ca^{2+} ion	33.8 nm
3	protein Extract + 0.2 mM Ca^{2+} ion	139.0 nm
4	protein Extract + 0.35 mM Ca^{2+} ion	434.87 nm
5	protein Extract + 0.5 mM Ca^{2+} ion	989.00 nm
6	in presence of large excesses of Ca^{2+} ion	6000 nm

Aggregation behavior of the protein extract in water and the calcium binding affinity of the protein mixtures present in LAB extracts was analyzed using dynamic light scattering (DLS). It is generally recognized that amphiphilic high molecular weight proteins tend to self-associate in water and form various kinds of aggregates because of the large repulsive segmental interactions and solubility differences between blocks. The particle size distribution results of *Lactobacillus plantarum* (MTCC 1325) and *Pediococcus acidilactici* (CFR K7) LAB extract with Ca^{2+} ion are shown in the Figure 3.17 and Table 3.1 respectively. The overall particle size (R_H) of the LAB extract obtained from MTCC 1325 and CFR K7 using DLS was found to be 7.6 nm and 10 nm respectively. This result indicates that the sizes of all folding intermediates are close in single distribution. The uniformity of the diameters can be considered as evidence for a quasi-static-like process and is a necessary criterion for preventing precipitation. Acid base titration revealed that the highly acidic in nature of LAB protein extracts. Therefore, in physiological pH (7.4) these proteins will carry large number of anionic carboxylate groups on their hydrophilic surface. Excessive charge on the surface will prevent them to form larger aggregates. Ca^{2+} ion in the solution forms complex with these anionic sites and reduces the effective charge on the surface of these proteins. Hence, they can form larger aggregates and the size of hydration radius of these proteins increases exponentially with the increasing Ca^{2+} concentration (Figure 3.18). The observation of uniform PSD of each of the aggregated structures suggested that they reached

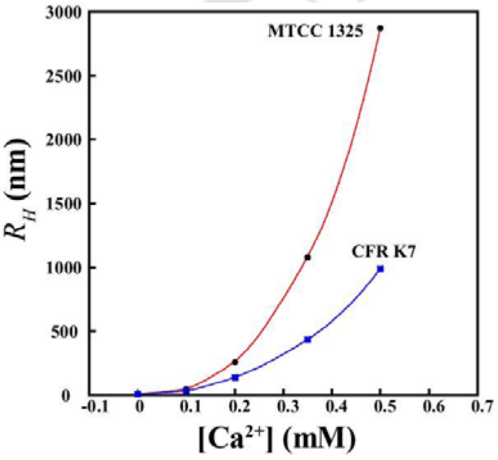

Figure 3.18. Effect of Ca^{2+} ion concentration on R_H of LAB protein extract.

equilibrium under each Ca^{2+} ion concentration. With large excess of cation in the solution, large aggregates of 6 µm were formed. These results also support the formation of protein-metal ion complex in the nucleation stage as postulated in the mineralization scheme (scheme 3.4).

Crystallization of calcium minerals

After an incubation period of 2 days in all the three LAB extracts small rhombohedral calcite crystals of ~ 3 µm in size were obtained (Figure 3.19a, 3.19b and 3.19c). Formation of similar crystal morphology in all three LAB extract also proves the similar surface characteristics of the proteins secreted from LAB. Figure 3.18d shows an early stage of crystal growth. It shows a number of rounded particles, which are nothing but the metastable vaterite. Elemental analysis (EDX) shows the presence of Ca, C and O (Figure 3.20a). The presence of the only Calcite polymorph (PDF No. 01-086-2342) was confirmed by PXRD analysis (Figure 3.20b). From the PXRD analysis of an early stage of crystal growth, it can be concluded that the calcite grows on expense of the metastable precursors (Figure 3.20c). This result also supports the Ostwald's rule [3.23] which states that, the least stable phase with the highest solubility is formed preferentially in the solution, and then transformed within a few minutes to thermodynamically most stable polymorph. Easy, reproducible, highly pure crystalline polymorph synthesis is one of the major advantages of these methods. With a similar type of organic matrix pure mineral phase was difficult to obtain [3.24].

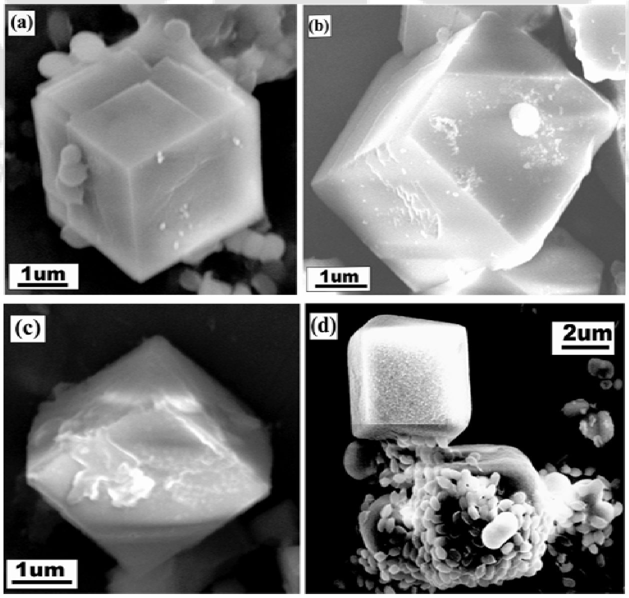

Figure 3.19. SEM micrograph of Calcite rhombohedra from (a) CFR K7 extract (b) MTCC 1325 extract, (c) MTCC 4495 extract and (d) CFR K7 extract in early stages.

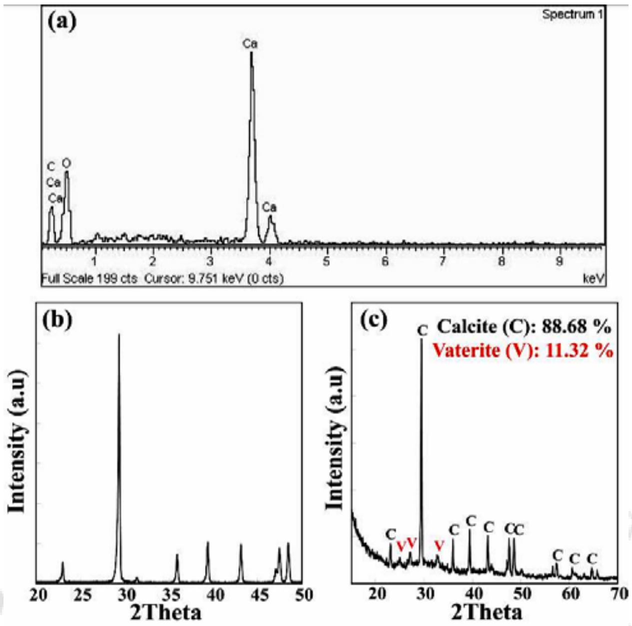

Figure 3.20. (a) EDX of $CaCO_3$, (b) PXRD pattern of calcite and (c) PXRD of early stage of $CaCO_3$ formation in CFR K7.

Calcium sulfate form rod-like structures (Figure 3.21a) with average thickness of 800 nm in CRF K7 extract, while the average thickness of the single rods are less than 300 nm which agglomerates into a bigger rod in case of MTCC 1325 extract (Figure 3.21b). In case of MTCC 4495, calcium sulfate form plate-like structures (Figure 3.21c), the average thickness of these plates are 250 nm. Elemental analysis (EDX) shows the presence of Ca, S and O (Figure 3.21d). The crystal phase was confirmed to be pure Gypsum ($CaSO_4$. $2H_2O$) (PDF No. 01-076-1746) (Figure 3.21e).

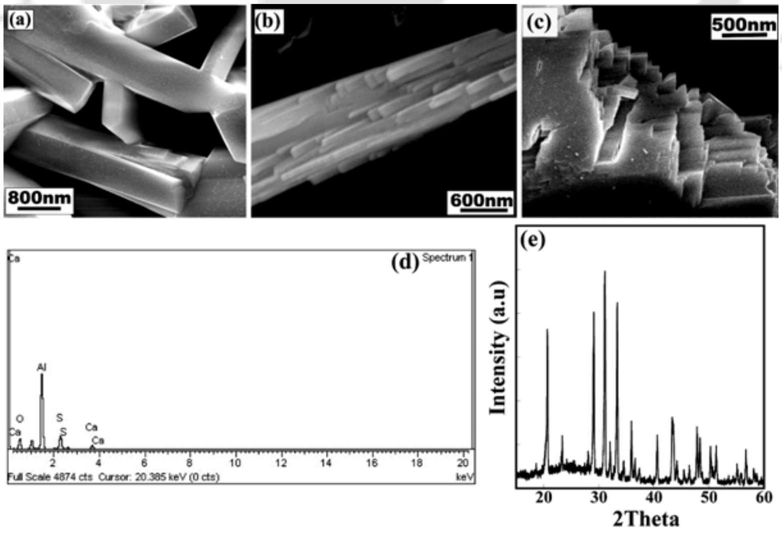

Figure 3.21. SEM micrograph of (a) Gypsum rods from CFR K7 extract, (b) Gypsum rods from MTCC 1325 extract, (c) Gypsum plates from MTCC 4495 extract, (d) EDX and (e) PXRD pattern of Gypsum.

Calcium oxalate crystals take the shape of hollow hexagon (Figure 3.22a) in CFR K7 extract. The thickness of these plates is in the range of 0.6 – 0.8 µm. In MTCC 1325 extract, calcium oxalate forms uniform rhombohedra (Figure 3.22b) having thickness range 0.8-0.9 µm. From MTCC 4495 extract, calcium oxalate takes the shape of solid hexagon (Figure 3.22c) with average thickness of 1.0 µm. Elemental analysis shows the presence of Ca, C and O (Figure 3.22d). The PXRD pattern confirms the crystal phase to be only Whewellite CaC_2O_4. H_2O (PDF No. 01-077-1160) (Figure 3.22e).

Calcium hydrogen phosphate form elongated rods of length in the range of 4 – 5 µm and average thickness of 750 nm in CFR K7 extract (Figure 3.23a). In presence of MTCC 1325 extracts rod like structure (Figure 3.23b) of same length was formed while average thickness was 1 µm. Calcium hydrogen phosphate forms elongated plates in MTCC 4495 extract having average thickness 350 nm (Figure 3.23c). Elemental analysis shows the presence of Ca, P and O (Figure 3.23d). PXRD pattern confirmed the crystal phase to be Brushite, $CaHPO_4$. $2H_2O$ (PDF No. 01-072-0713). Presence of two water molecules was confirmed by thermal studies (Figure 3.23e).

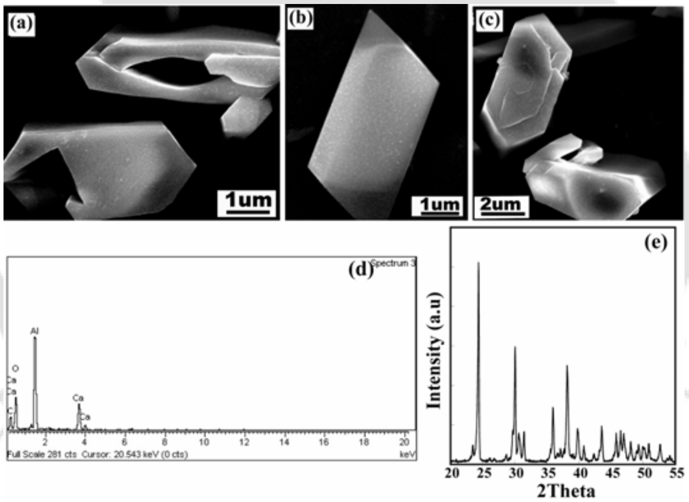

Figure 3.22. SEM micrograph of (a) Whewellite hexagon from CFR K7 extract, (b) Whewellite rhombohedra from MTCC 1325 extract, (c) Whewellite hexagon from MTCC 4495 extract, (d) EDX and (e) PXRD pattern of Whewellite.

Crystallization of barium minerals

Barium carbonate forms rods of average thickness ~250 nm. Originating from a common point, it ultimately assumes a flower like morphology (Figure 3.24a) in presence of CFR K7 extract. From MTCC 1325, structure having similar shape and dimensions were observed (Figure 3.24b). In case of MTCC 4495, elongated flower life morphology was observed (Figure 3.24c). The petals are made of plates of thickness range 150 – 200 nm, which stack together on top of each other. Similar shapes of these minerals also confirm the similar surface property of all the protein extract. Elemental analysis shows the presence of Ba, C and O (Figure 3.24d). PXRD pattern shows that bulk product is crystalline in nature and phase of the mineral is found to be as Witherite (PDF No. 01-071-2394). Here also the formation of pure mineral polymorph is observed (Figure 3.24e).

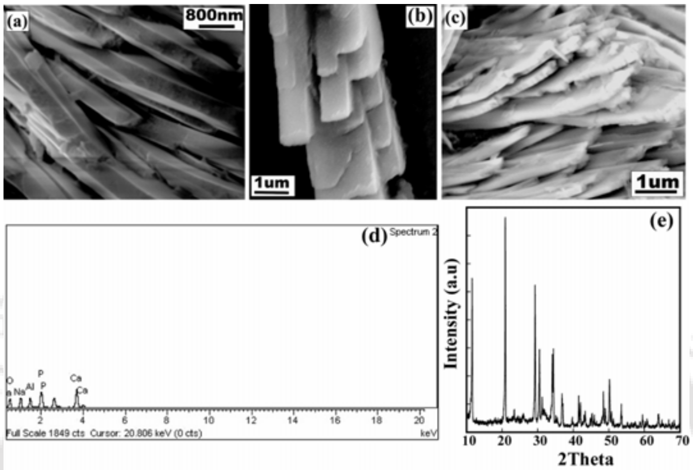

Figure 3.23. SEM micrograph of (a) Brushite rods from CFR K7 extract, (b) Brushite rods from MTCC 1325 extract, (c) Brushite plates from MTCC 4495 extract, (d) EDX and (e) PXRD pattern of Brushite.

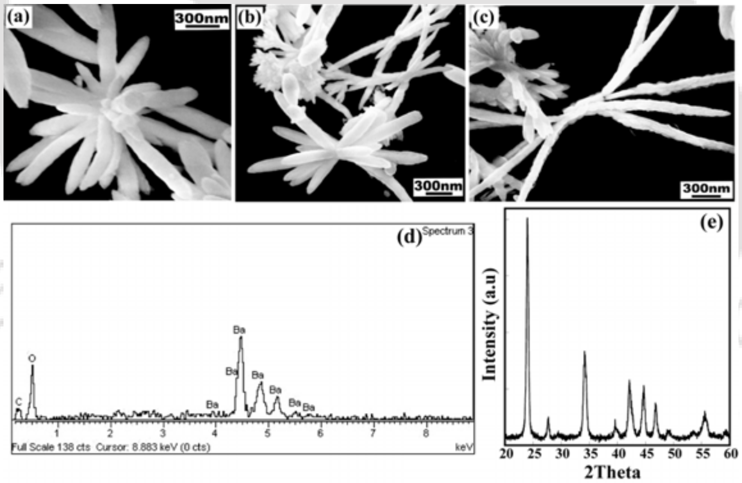

Figure 3.24. SEM micrograph of (a) Witherite from CFR K7 extract, (b) Witherite from MTCC 1325 extract, (c) Witherite from MTCC 4495 extract, (d) EDX and (e) PXRD pattern of Witherite.

The SEM image shows unique dendritic architectures of barium sulphate (Figure 3.25a) with a length of 2-7 μm along the trunk from CFR K7 extract. Further observation reveals that the individual $BaSO_4$ dendrite is composed of a long central trunk with secondary and tertiary sharp branches having width in the range of 200 nm – 500 nm (Figure 3.25b). It is interesting that the secondary branches are parallel to each other and emerge at an angle of 60^o with respect to the central trunk. Similar projection phenomena are also found for the tertiary branches. In MTCC 1325 extract, this type of highly symmetrical dendritic growth is less prominent (Figure 3.25c). In contrast to the former structure, the branches are rectangular and not segmented. The size of these rectangular plates varies from 200 to 500 nm. However, from MTCC 4495 extract, barium sulphate forms sharp needles of thickness between 200 to 400 nm (Figure 3.25d). Elemental analysis shows the presence of Ba, S and O (Figure 3.26a). PXRD pattern confirms the mineralogical phase to be Barite (PDF No. 01-089-7357) (Figure 3.26b).

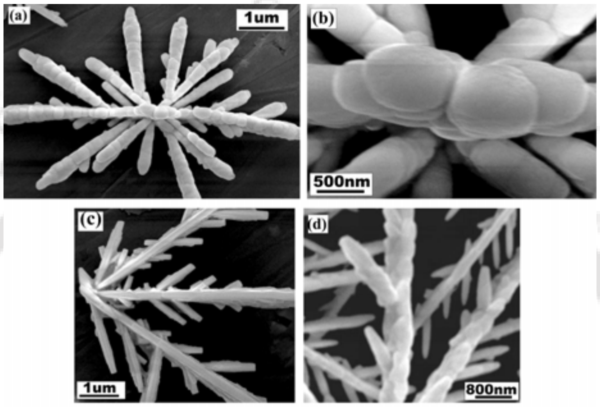

Figure 3.25. SEM micrograph of dendritic Barite (a) and (b) from CFR K7 extract, (c) from MTCC 1325 extract and (d) from in MTCC 4495 extract.

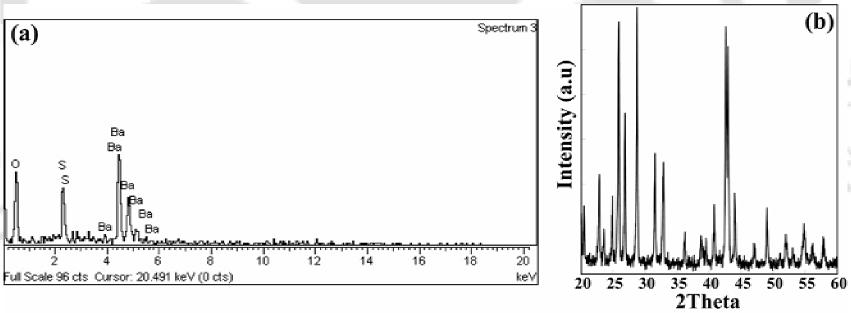

Figure 3.26. (a) EDX of Barite and (b) PXRD pattern of Barite.

Barium Oxalate crystals took the shape of uniform rod of thickness in the range 0.5 to 1.0 μm (Figure 3.27a) from CFR K7 extract. Whereas in MTCC 1325, Barium oxalate rods of average thickness 1.0 μm agglomerate to form a sphere (Figure 3.27b). In presence of MTCC 4495 extract also rod are formed of average thickness 0.8 μm (Figure 3.27c). Elemental analysis shows the presence of Ba, C and O (Figure 3.27d). Barium oxalate hemi hydrate *i.e.* $Ba(C_2O_4)$. 0.5 H_2O (PDF No. 00-020-0134) mineral phase is confirmed by PXRD. Removal of 0.5 H_2O and one CO_2 was supported by thermal analysis (Figure 3.27e).

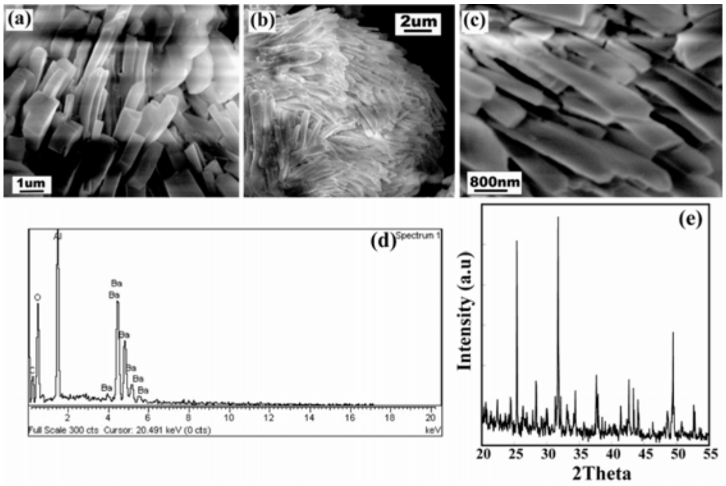

Figure 3.27. SEM micrograph of (a) Ba-oxalate from CFR K7 extract, (b) Ba-oxalate from MTCC 1325 extract, (c) Ba-oxalate from MTCC 4495 extract, (d) EDX and (e) PXRD pattern of Ba-oxalate.

In CFR K7 extract, plates of barium phosphate of average thickness 0.80 µm stacks into hierarchical order (Figure 3.28a). In MTCC 1325 extract, barium phosphate rectangular blocks of average thickness 1.0 µm (Figure 3.28b), stack in a random manner in 3D. Whereas in MTCC 4495 extract, it forms layered plate like morphology having blunt and rounded edge (Figure 3.28c). The thickness of the layers was found to be in the range 100 to 200 nm. Elemental analysis shows the presence of Ba, P and O (Figure 3.28d). Barium Hydroxide Phosphate [$Ba_5(OH)(PO_4)_3$] (PDF No. 00-001-0811) mineral phase was confirmed by PXRD (Figure 3.28e).

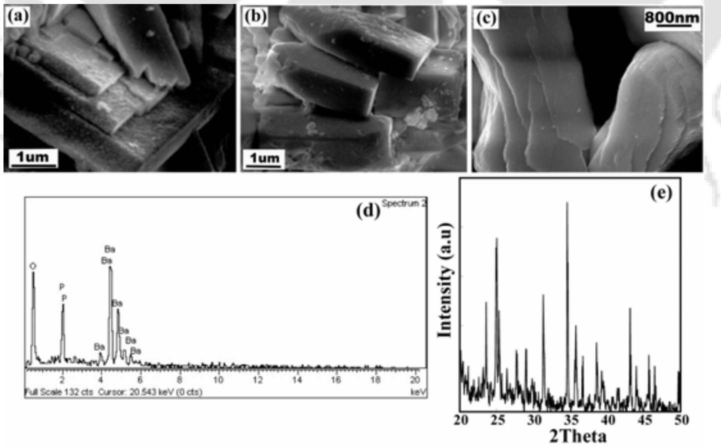

Figure 3.28. SEM micrograph of (a) Barium hydroxide phosphate from CFR K7 extract, (b) Barium hydroxide phosphate from MTCC 1325 extract, (c) Barium hydroxide phosphate from MTCC 4495 extract, (d) EDX and (e) PXRD pattern of Barium hydroxide phosphate.

Control Experiments

We tried the mineralization process in MRS medium in which the LABs were grown, to check the role of the medium ingredients in the process of biomineralization. But in the absence of LAB strains, apart from some bulk aggregates no uniform structure was observed. From these result we can conclude that ingredients of MRS medium is not directly involved in the mineralization process and the presence of high molecular weight proteins are necessary for crystal growth modification. Some of the representative SEM images of control experiments are in the Figure 3.29. When we performed mineralization process with the LAB extracts before dialysis, we got some relatively larger aggregates without any uniform structures. From this observation we can conclude that the presence of low molecular weight organic/inorganic substance in the mixture inhibit the effect of high molecular weight proteins in the crystal growth modification. Figure 3.30 shows SEM pictures of some representative mineral formed in presence of undialyzed LAB extract.

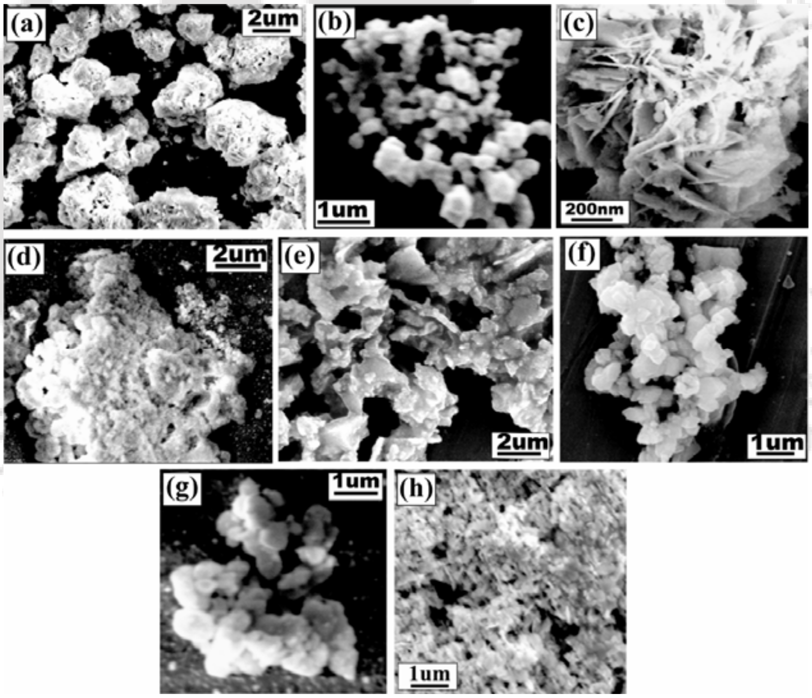

Figure 3.29. SEM images of (a) Calcite, (b) Gypsum, (c) Whewellite, (d) Brushite, (e) Witherite, (f) Barite, (g) Ba-oxalate and (h) Barium Hydroxide Phosphate in MRS medium.

Effect of the native structure of proteins

The effect of the native structure of various high molecular weight (>12 kDa) proteins present in the LAB extracts was examined by denaturing the tertiary structure. Although there are various effective ways of denaturing the 3D structure of proteins (viz: using urea, by varying pH, by adding other bacteria/cleaving agent), but we destroyed the protein 3D structures by heating the dialyzed LAB extracts at 90°C for 3 hrs. This is because use of external denaturing agents may have potential effect in

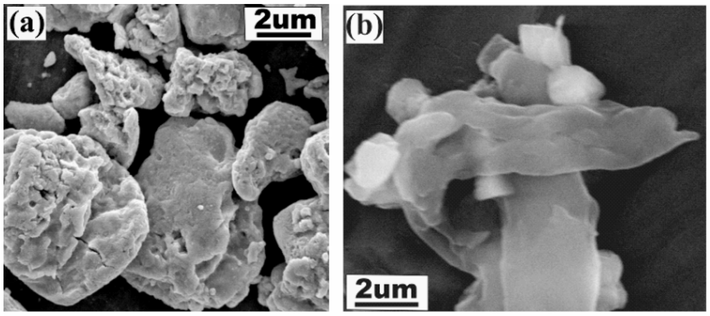

Figure 3.30. SEM images of (a) calcite, (b) gypsum from undialyzed LAB extract.

biomineralization processes by acting as a template. Moreover, during pH variation, especially at lower pH, most of the minerals are soluble and it is difficult to isolate the solid mineral from water. On the other hand, at higher pH, precipitation of $Ca(OH)_2$ / $Ba(OH)_2$ takes place immediately. After denaturing the proteins by heating at 90°C for 3 hrs and then performing the sequence of reactions at hot condition, we did not get any uniform structures of the minerals. Hence, we can conclude that the native structures of high molecular weight proteins play a crucial role in modifying as well as stabilizing the morphologies of the minerals (Figure 3.31).

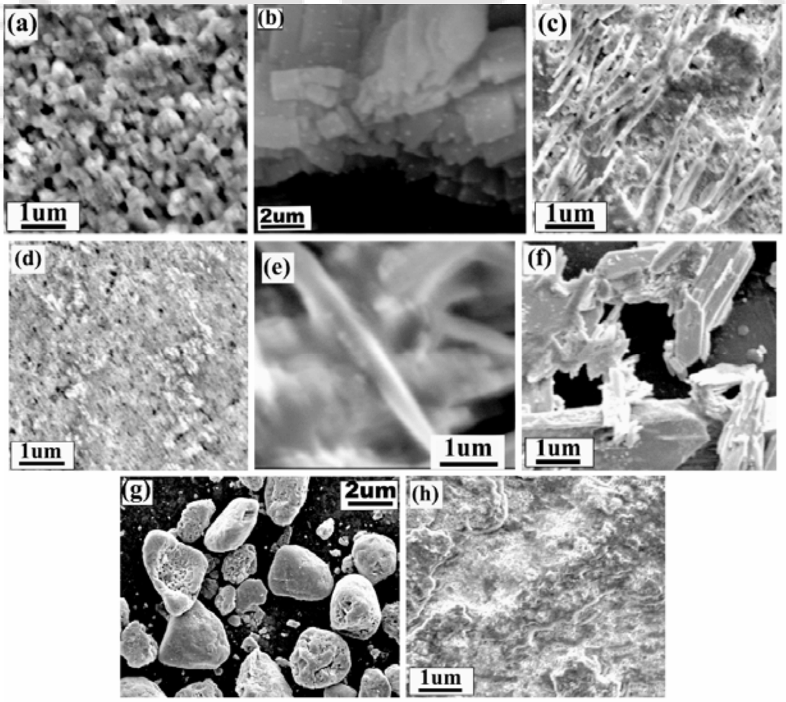

Figure 3.31. SEM images of (a) Calcite, (b) Gypsum, (c) Whewellite, (d) Brushite, (e) Witherite, (f) Barite, (g) Ba-oxalate and (h) Barium Hydroxide Phosphate from denaturized LAB extract.

Formation of High Purity Ca(OH)$_2$

Synthesis of high purity Ca(OH)$_2$ is an important industrial processes as it is largely used in dental compositions and other bio-medical application [3.25]. The calcite rhombohedra were heated to 1000 ^{o}C in N_2 atmosphere for 6h in a silica crucible. The resulting CaO were rapidly cooled to RT, by using P_2O_5 and KOH filled dryers. The PXRD pattern of the formed CaO particles matches with the mineral phase of lime (PDF No. 01-082-1691) (Figure 3.32a). The resulting CaO was re-hydrated in saturated water vapor at 60 ^{0}C for 7 h. To prevent the reaction with atmospheric CO_2, the hydration processes was done under N_2 atmosphere. CaO particles were converted into high purity Ca(OH)$_2$. These CaO particles forms Ca(OH)$_2$ fibers after re-hydration (Figure 3.32b). The average thicknesses of the fibers are <100 nm and length varies from 2 – 6 μm. The mineral phase of the Ca(OH)$_2$ is confirmed to be Protlandite (PDF No. 01-087-0637) from PXRD pattern (Figure 3.32c).

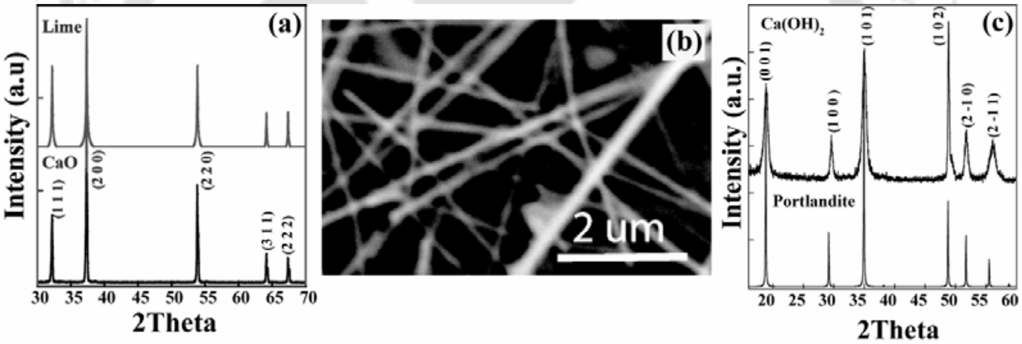

Figure 3.32. (a) PXRD pattern of as prepared CaO particles and standard Lime, (b) SEM micrograph of Ca(OH)$_2$ fibers and (c) PXRD pattern of Ca(OH)$_2$ fibers and standard portlandite.

3.3.3. Summary

The secreted protein extracts from *Pediococcus acidilactici* CFR K7, *Lactobacillus plantarum* MTCC 1325 and *Lactobacillus acidophilus* MTCC 4495 form the organic matrix in mineralization processes and influence the growth of minerals. An extensive study of this matrix in the crystallization of common calcium as well as barium minerals has been conducted. Although LABs are not related to biological materialization processes, however, as the acidic proteins are known to form matrix for biomineralization, we have tested these fundamental coordination aspect with acidic LAB extracts. The present study provided a fundamental understanding of the role of acidic proteins as an organic matrix to facilitate nucleation and crystal growth. Further, the generation of remarkable architecture of minerals has significant implications in developing chemistry for manufacturing micron- to nanoscale functional materials. From our experiments we have demonstrated for the first time that high molecular proteins secreted by food-grade lactic acid bacteria are able to change the crystal morphology. These large biomacromolecules form a matrix and initiate the nucleation. Small bacterial metabolites in the mixture impede the crystal growth. Native structures of the proteins have strong influence on the final morphology of the crystal. We have proposed and experimentally verified that these high molecular weight acidic proteins act as soft, flexible nucleation centre for the minerals. Easy, reproducible, highly pure crystalline polymorph synthesis is one of the major advantages of these methods. We have also synthesized bio-medically important high purity $Ca(OH)_2$ via precursor method in the laboratory scale. Large-scale preparation of these materials is now in progress in our laboratory.

3.3. Modulation of crystal morphology using gel diffusion technique

The remarkable range of morphologies exhibited by biominerals has inspired the biomimetic synthesis of inorganic materials with complex form [3.26]. Different bio-macromolecules including proteins and polysaccharides have been used for the *in vitro* study of controlled crystallization, as they play key roles in biomineralization processes [3.27]. In particular, collagenous matrices, such as cross-linked gelatin xerogels [3.28] and gelatin hydrogels [3.29] have received considerable attention. Among many different techniques used in the *in vitro* studies, gel precipitation methods, used for over a century for the growth of large crystals [3.30]. The main advantage of gel diffusion techniques is to reduce the volume of the precipitation reaction and thus, the quantity of the biomolecule required for characterizing the effects of matrix molecules on mineralization [3.30]. However, there are only few efforts have been made towards the controlled crystallization of calcium and barium minerals in hydrogels formed by polysaccharides [3.31]. It is expected that gels do not directly affect the crystallization and gels just play a role of reaction media that control the diffusion process of ions in the media and hinder the crystal growth when the crystal size reaches the pore size of the gel network. The gelators form various nanostructures such as nanofibers, nanoribbons, nanorods and nanoparticles depending on their molecular structures, solvents, and concentrations [3.32]. The physio-chemical nature of this process more realistically mimics the unique matrix environment of mineralized tissue, compared to non-gel solution studies [3.30]. The system allows study of *de novo* nucleation, or heterogeneous nucleation and growth. This is important for elucidation of the role played by protein in nucleation, growth, and/or or inhibition.

In this section, we have reported the crystal formation and growth modification of some common biologically important calcium and barium minerals in two different gels *viz*: Agarose and Agar-agar gels. Agarose is a linear polysaccharide extracted from marine red algae, and consists of alternating 1,3-linked β-D-galactose and 1,4-linked 3,6-anhydro-a-L-galactose.

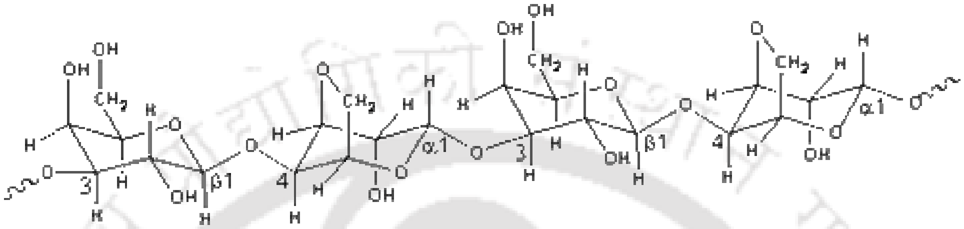

It forms a gel when a homogeneous solution is cooled to below the ordering temperature (~ 35°C) and an infinite three-dimensional network of agarose fibers develops; the melting of agarose gels occurs at a comparatively higher temperature (~ 85°C), leading to a setting–melting hysteresis behavior [3.33]. Agar consists mainly of a mixture of neutral agarose and anionic agaropectin, with a large number of attached side groups. Previous study [3.34] predicts that the main role agarose gels play on the $CaCO_3$ crystallization is the control on the diffusion process of reactant ions rather than the hindering of crystal growth. This was confirmed by considering the pore size for the 1% agarose gels which is around 140 nm [3.35], considerably smaller than the initial rhombohedral calcite crystals. Again to understand the mechanism how non-collagenous proteins and other biomolecules help to control the biomineralization processes *in vitro* growth of hydroxyapatite in different gels have been reported [3.30]. Hunter et al. [3.36] and Gold berg et al. [3.37] extended their gel diffusion method as a tool to characterize the mechanisms of protein-mineral interaction. We have shown the formation of different nano to micron-scale architectures of Ca and Ba minerals in presence of these hydrogels formed by well known gel diffusion technique when doped with soluble Ca/Ba salts and anions are allowed to diffuse through pores.

3.3.1. Crystallization Experiments

In a typical experiment, 0.5 M $CaCl_2$ / $BaCl_2$ solution in Milli-Q water was heated to 75-80 ^{O}C and 0.5 % (w/w) of agar-agar / agarose was added, which was further heated to 85-90 ^{O}C to ensure dissolution of agar-agar / agarose. The resulting hot solution was poured into a Petridis and cooled to room temperature slowly. The cooled thick gels plates were cut into cubic pieces about 1 cm^3 in volume. Then the gel cubic pieces were soaked in 0.5 M solution of counter anions viz. Na_2CO_3, Na_2SO_4, $Na_2C_2O_4$ and Na_2HPO_4 respectively at 25 ± 1 °C without any mechanical disturbance. After 1-3 days, the gel cubes were rinsed in Milli-Q water to get rid of the residual soluble inorganic salts. The resulting minerals were recovered from the gel matrix by dissolving the gel cubes in Milli-Q water (~95 ^{O}C). Crystalline products were collected through hot vacuum filtration followed by washing several times with Milli-Q. The preliminary experimental results showed that the short period heating in hot water does not affect the crystal morphology considerably (Scheme 3.5).

3.3.2. Results and Discussions

Effect of Concentration of Gel

To examine the effect of concentration of the gel on the crystal growth modification, experiments were performed varying the percentage of agar-agar / agarose gel as 1.5 %, 1.0 %, 0.5 % and 0.2 % (w/w). In case of 1.5 % and 1.0 %, hard gel cubes were obtained which results in the formation of very minute amount of precipitate even after 2 weeks. The reason behind this observation is that, with increasing the concentration of gel pore size becomes smaller [3.38], which prevents the easy diffusion of counter anions in the gel matrix to form the minerals. Very soft gel plates have formed in 0.2 % gel concentration, which cannot be cut into cubes, can be formed but as the percentage of gel is very less, it cannot be cut into cubes. Nevertheless, due to the less concentration and large pore size of the gel matrix, Ca^{2+} / Ba^{2+} came out of the matrix easily. This results in the formation of almost immediate precipitation when soaked in solution of counter anion. Best results were

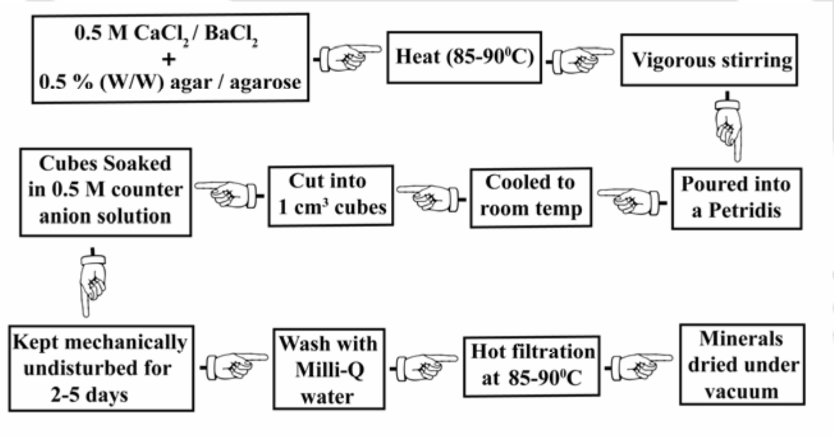

Scheme 3.5. Gel mediated mineral synthesis.

obtained in 0.5 % agar-agar / agarose gel concentration. Hence, 0.5 % (w/w) gel concentration was used for all the crystallization experiments (Scheme 3.6).

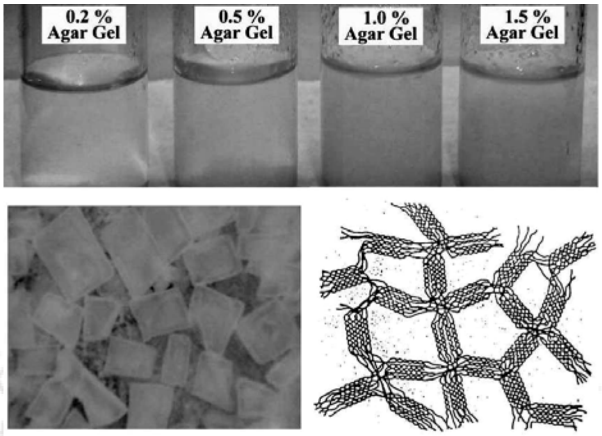

0.5% Agar Gel cubes Gel network with 10-10,000 helices

Scheme 3.6. Gel formation: Effect of concentration

Effect of the Concentration of Ions

The experiment was carried out separately in 0.5 % agar-agar and 0.5 % agarose gel by using six different concentrations: 1.0, 0.5, 0.1, 0.01, 0.001 and 0.0001 M of $CaCl_2$ / $BaCl_2$ and corresponding concentration of counter anions *viz.* Na_2CO_3, Na_2SO_4, $Na_2C_2O_4$ and Na_2HPO_4. It was observed that when the concentration was high, immediate precipitation took place without any modification on the crystal morphology. Crystallization was so fast that it was difficult to clearly distinguish between processes occurring during nucleation, growth and ripening stages. Most cases amorphous materials were formed. As we decrease the concentration, formation of the minerals took more time but crystal nature become more prominent. Best result was obtained in 0.5 M $CaCl_2$ / $BaCl_2$ and the counter anions concentrations. Hence, 0.5 M of ion concentration was used for all the crystallization experiments.

Crystallization of Calcium Carbonate

After an incubation time of 2 days in agar-agar gel, small calcite crystals (~ 4 μm) with a typical rhombohedral morphology were obtained Figure 3.33a. An enlarged image of rhombohedral calcite crystals (Figure 3.33b) shows the calcite micro steps, strongly indicating the single-crystalline nature of the rhombohedral calcite crystals. It shows the terraced excavation on each {104} face of the rhombohedra. In agrose gel, we got relative smaller (~ 2 μm) calcite crystals of rhombohedral morphology (Figure 3.33c). In contrast to the calcite crystal in agar-agar gel, these crystal surfaces are smooth and uniform with out any noticeable surface defects. The presence of the only Calcite polymorph (PDF No. 01-086-2342) in highly crystalline bulk sample was confirmed by PXRD analysis of the (Figure 3.34a). Characteristic FT-IR bands (Figure 3.34b) corresponding to calcite crystal found to be at 1080, 879 and 706 cm^{-1} [3.39].

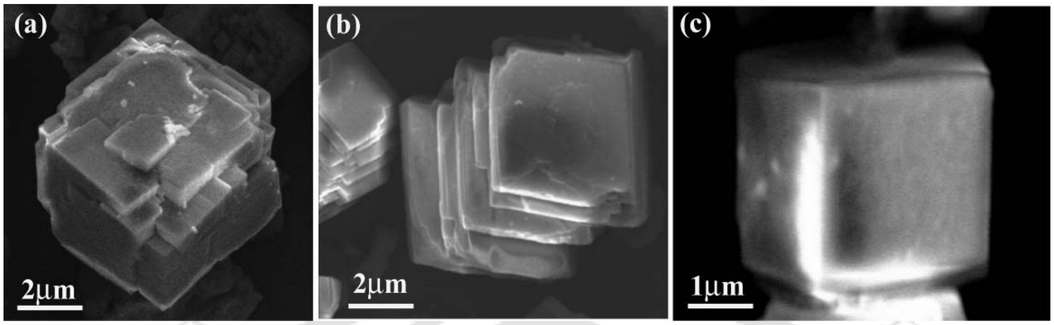

Figure 3.33. SEM image of (a) and (b) Calcite from Agar-Agar gel and (c) Calcite from Agarose gel.

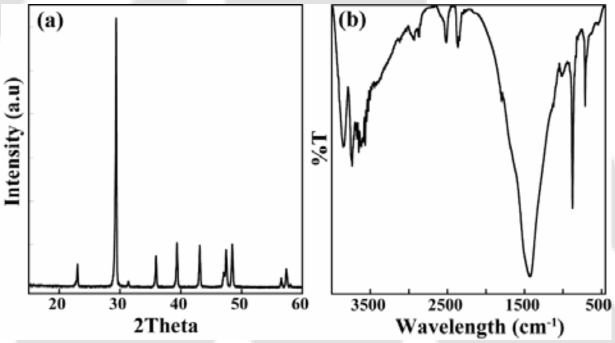

Figure 3.34. PXRD pattern of Calcite crystals and (b) FT-IR spectrum of Calcite crystals.

Crystallization of Calcium Sulfate

As shown in Figure 3.35a, calcium sulfate form bushes made of micro plates with length ranging from 6 to 10 μm in size in agar-agar gel. An enlarged image of the bushes Figure 3.35b shows the formation of hexagonal micro plates of average thickness ~ 2 μm, strongly indicating the single-crystalline nature of the gypsum crystals.

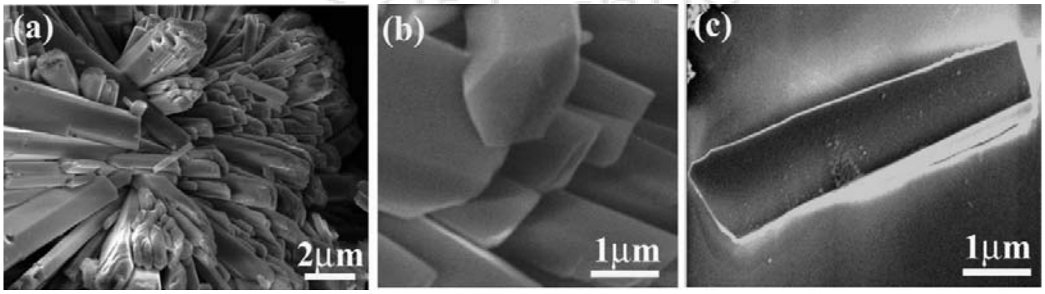

Figure 3.35. SEM image of (a) and (b) Gypsum micro plates from 0.5 % Agar-Agar gel and (c) Gypsum micro plates from 0.5 % Agarose gel.

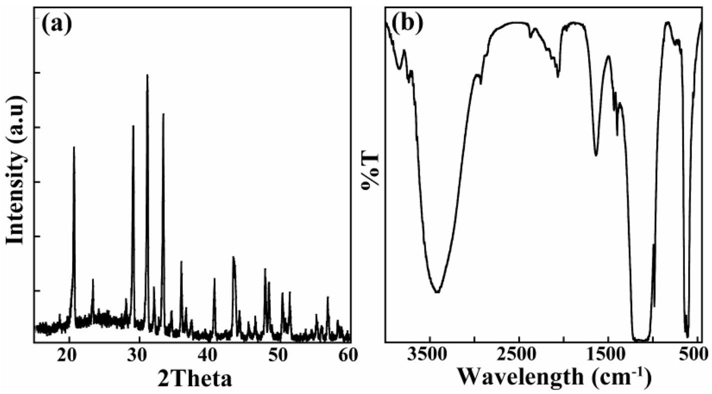

Figure 3.36. (a) PXRD pattern and (b) FT-IR spectrum of Gypsum.

However, in agarose gel it takes the shape of rectangular plates of width ~ 1 μm (Figure 3.35c). These plates does not form any aggregated structures in contrast to the former one. Surface of both the micro plates are smooth and even. The crystal phase is confirmed to be Gypsum ($CaSO_4. 2H_2O$) (PDF No. 01-076-1746) by PXRD pattern (Figure 3.36a). FT-IR spectrum shows (Figure 3.36b) the ν_3 band at 1150 cm^{-1} (ν_s) and ν_4 bands at 666 cm^{-1} (s), 600 cm^{-1} (s) correspond to the SO_4^{-2} ion [3.40].

Crystallization of Calcium Oxalate

Calcium oxalate crystals take the shape of octagonal plates Figure 3.37a in 0.5 % agar-agar gel. The thickness of these plates is in the range of 0.2 – 0.3 μm, whereas the length varies from 1 to 3 μm. In 0.5 % agarose gel, calcium oxalate crystals show hexagonal segmented plate morphology Figure 3.37b. In contrast to the octagonal crystals, hexagonal plates have lesser thickness (50 – 200 nm) and shorter length (0.2 – 0.5 μm). The PXRD confirms the crystal phase to be Whewellite (PDF No. 01-077-1160) with molecular formula $CaC_2O_4.H_2O$ (Figure 3.38a). FT-IR analysis (Figure 3.38b) shows the presence of peaks at 1618, 1325, 783, 665, 517 cm^{-1} characteristics of coordinate oxalate ion and calcium oxalate monohydrate (COM) [3.40].

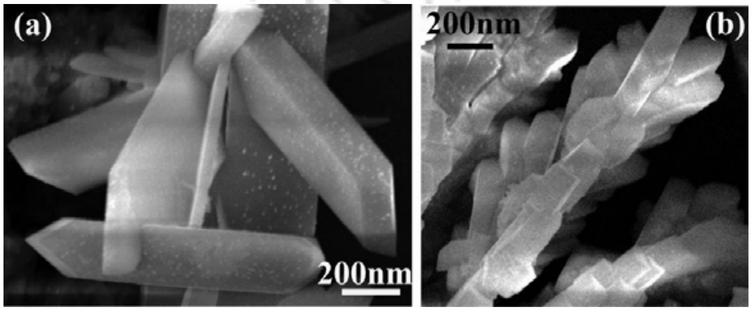

Figure 3.37. SEM image of (a) Whewellite from 0.5 % agar-agar gel and (b) from 0.5 % Agarose gel.

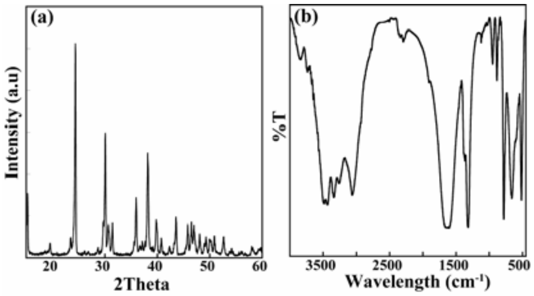

Figure 3.38. (a) PXRD pattern and (b) FT-IR spectrum of Whewellite.

Crystallization of Calcium Hydrogen Phosphate

Calcium hydrogen phosphate form typical brick morphology of length in the range of 8 – 10 µm (Figure 3.39a) from 0.5 % agar-agar gel. The average widths of these blocks are 3 µm. In presence of 0.5 % Agarose gel, calcium hydrogen phosphate form elongated thin rod like structure (Figure 3.39b) of same length but width and thickness are comparatively shorter. PXRD pattern confirm the crystal phase to be Brushite, $CaHPO_4 . 2H_2O$ (PDF No. 01-072-0713) (Figure 3.40a). FT-IR analysis (Figure 3.40b) shows broad band centered around 3450 cm^{-1} is due to intermolecular and weakly H bonded OH because of water of crystallization [3.41]. The weak absorptions at 2375 cm^{-1} is due to HPO_4^{2-} [3.42]. The H-O-H bending gives rise to absorption at 1651 cm^{-1}. The absorptions at 1210 and 1140 cm^{-1} are due to P = O associated stretching vibrations. Whereas, the absorption at 1068 cm^{-1} is due to P = O stretching vibrations. The P-O-P asymmetric stretching vibrations give rise to

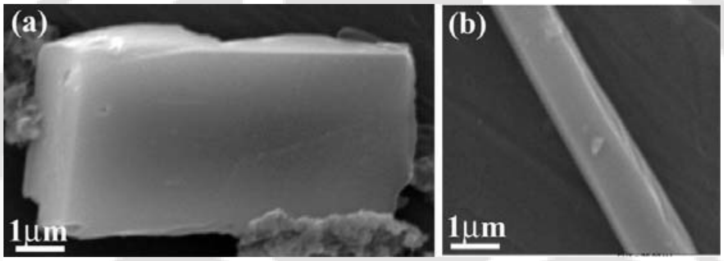

Figure 3.39. SEM image of (a) Brushite rods from 0.5 % Agar-Agar gel and (b) from 0.5 % Agarose gel.

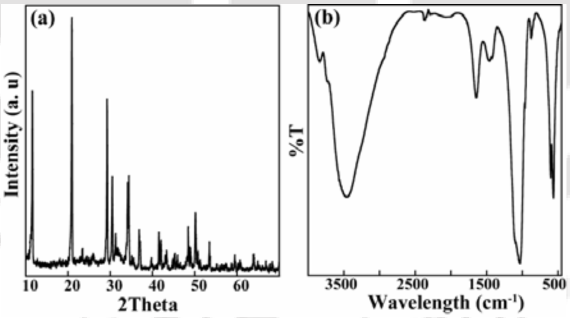

Figure 3.40. (a) PXRD pattern of Brushite and (b) FT-IR spectrum of Brushite.

absorptions at 987 and 874 cm^{-1}. The absorptions at 577 and 525 cm^{-1} are again due to acid phosphates [3.40].

Crystallization of Barium Carbonate

$BaCO_3$ forms aggregates of micro plates from 0.5 % agar-agar gel (Figure 3.41a). Mature crystals form a beautiful flower bouquet like structure. An enlarged image of these flower bouquets show that each micro plates have grown radially from a common point of origin (Figure 3.41b). The average thickness of the plates is 0.3 µm. In 0.5 % Agarose gel, $BaCO_3$ again does not form any aggregates. It forms the elongated thin plates with thickness range from 0.5 to 1 µm (Figure 3.41c). PXRD pattern shows that product is crystalline in nature and phase of the mineral is found to be as Witherite (PDF No. 01-071-2394) (Figure 3.42a). Characteristic stretching frequencies of witherite are found to be 1450 (υ_3), 1063(υ_1), 680 (υ_4) cm^{-1} in FT-IR spectra (Figure 3.42b).

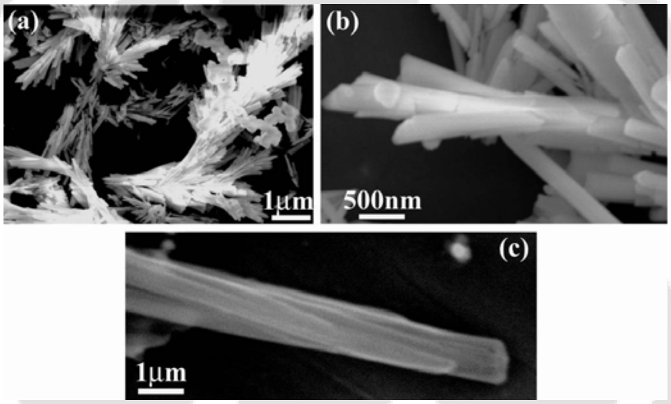

Figure 3.41. SEM image of Witherite (a) and (b) in 0.5 % Agar-Agar gel and (c) in 0.5 % Agarose gel.

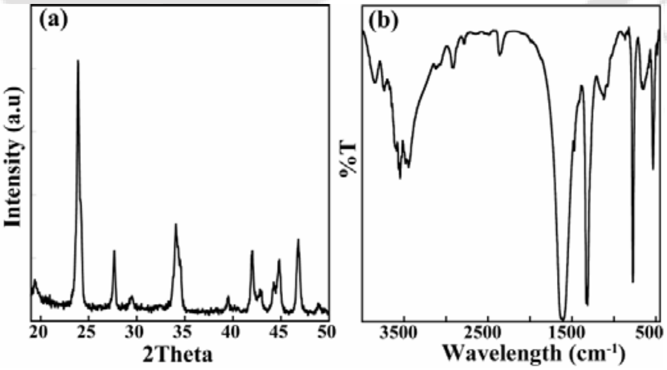

Figure 3.42. (a) PXRD pattern and (b) FT-IR spectrum of Witherite.

Crystallization of Barium Sulfate

Figure 3.43a shows the images of hierarchical $BaSO_4$ dendritic architectures with a length of 10-20 µm along the trunk in 0.5% agar-agar gel. Further observation reveals that the individual $BaSO_4$ dendrite is composed of a long central trunk with secondary and tertiary sharp branches having width in the range of 1.0 – 2.0 μm. It is interesting that the secondary branches are parallel to each other and emerge at 60 angles with respect to the central trunk. Similar phenomena are also found toward the tertiary branches. However, in 0.5 % agarose gel this type of dendritic growth is less prominent. In contrast to the former structure, the tip of each branches are round shape. The size of these blunt needles varies from 0.1 to 0.6 μm (Figure 3.43b). PXRD pattern confirms the mineralogical phase to be Barite (PDF No. 01-089-7357) (Figure 3.44a). FT-IR spectrum of Barite shows there are a υ_3 band at 1110 and 1085 cm^{-1} and υ_4 at 640 and 660 cm^{-1} corresponding to the sulfate (Figure 3.44b).

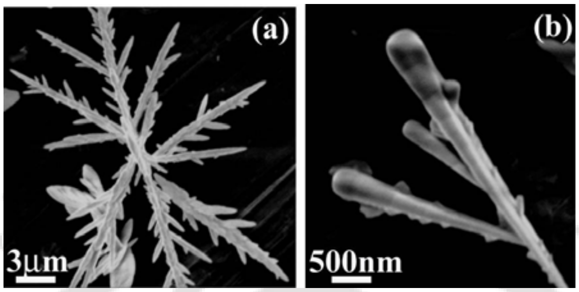

Figure 3.43. SEM image of Barite needles from (a) 0.5 % Agar-Agar gel and (b) 0.5 % Agarose gel.

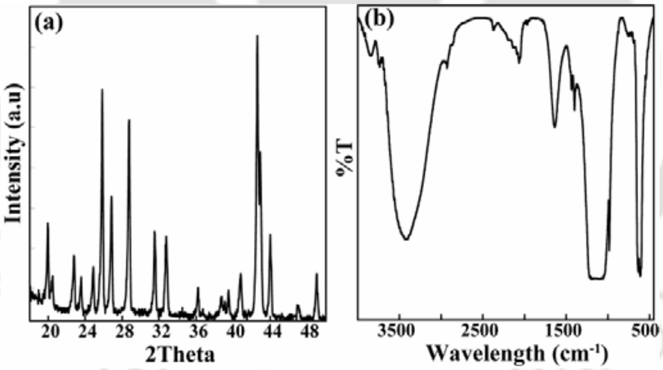

Figure 3.44. (a) PXRD pattern and (b) FT-IR spectrum of Barite.

Crystallization of Barium Oxalate

Barium Oxalate in 0.5 % agar-agar gel forms the bundles of micro plates, with a number of elongated sharp plates emerging out from a common point (Figure 3.45a). Higher magnified image reveals that the length of these plates varies from 4 to 10 μm while width are of < 1.0 μm in dimension (Figure 3.45b). In agarose gel Barium Oxalate forms a unique spider like structure (Figure 3.45c). Higher magnified image reveals that the whole structure is composed of small unit without any regular shape. The length of these small crystallites has a range from 0.2 to 0.6 μm (Figure 3.45d). PXRD pattern confirms the phase to be as Barium oxalate hemi hydrate i.e. $Ba(C_2O_4)$. 0.5 H_2O (PDF No. 00-020-0134) (Figure 3.46a). FT-IR analysis (Figure 3.46b) shows the presence of peaks at 3590, 1620 (υa), 1350 (υs), 840, 720 cm^{-1} which are characteristics of coordinated oxalate ions and barium oxalate hemi hydrate [3.40].

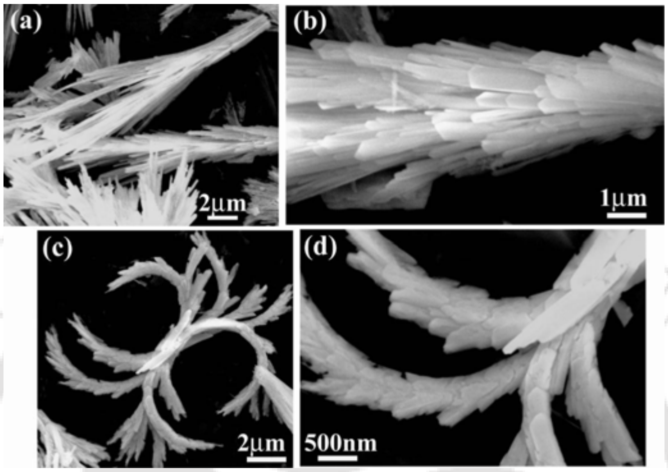

Figure 3.45. SEM image of (a) and (b) Ba-oxalate needles from 0.5% Agar-agar gel; (c) and (d) Spider like Ba-oxalate from 0.5% agarose gel.

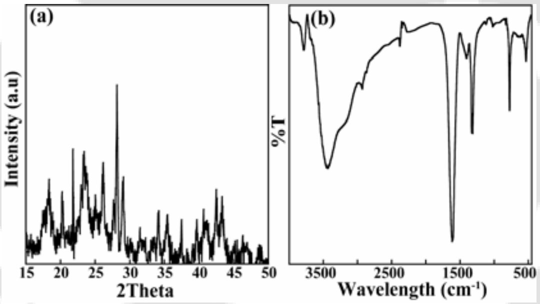

Figure 3.46. (a) PXRD pattern and (b) FT-IR spectrum of Ba-oxalate.

Crystallization of Barium Phosphate

In 0.5% agar-agar gel, Barium Phosphate forms a unique segmented arrow like morphology of width 3 - 4 μm (Figure 3.47a). Closer look at the structure revealed that these arrow structures are formed due to controlled agglomeration of nano-fibres (~ 30 nm). In 0.5 % agarose gel, we got morphology of broken leaf comprising of comparatively longer nano-fibres (Figure 3.47b). PXRD pattern shows that the phase of the mineral is found to be as Barium Hydroxide Phosphate with a molecular formula $[Ba_5(OH)(PO_4)_3]$ (PDF No. 00-001-0811) (Figure 3.48a). The FT-IR analysis (Figure 3.48b) shows characteristic stretching frequencies of Barium phosphate are at 3550, 1065, 980, 880 cm^{-1} corresponding to the OH^- and phosphate ion respectively [3.40]. The algal polysaccharides, agar-agar and agarose carry mainly hydroxy functional groups. The matrices of polysaccharides usually do not solely exert direct effects on mineral crystallization [3.43]. Therefore, it is expected that in the present case, agar-agar and agarose molecules do not directly affect the crystallization processes. Both the gels just play a role of reaction media that control the diffusion process of ions in the media and hinder the crystal growth when the crystal size reaches the pore size of the respective network. The pore size of the agar-agar gel matrix is more than that of the agarose gel at the same concentration [3.44]. We have compared and analyzed the size and shape of the building blocks of each micro structure of Ca and Ba minerals. It is observed that for a particular mineral, size of the building blocks are smaller in agarose gel compared to the agar-agar gel. However, pore size of the gel matrix has no control on the crystal phase and macroscopic aggregation of the small building units. This result implies that ion transport controlled by biological matrices may play an important role on biomineralization.

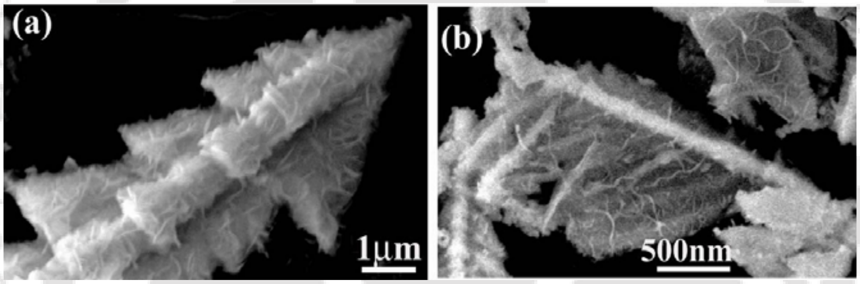

Figure 3.47. SEM image of (a) Barium hydroxide phosphate arrow like morphology from 0.5 % Agar-Agar gel, (b) Barium hydroxide phosphate at higher magnification and (c) Barium Hydroxide Phosphate in 0.5 % Agarose gel.

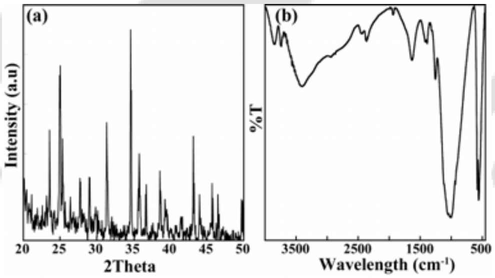

Figure 3.48. (a) PXRD pattern and (b) FT-IR spectrum of Barium hydroxide phosphate.

3.3.3. Summary

The advantage of gel diffusion technique over other non-gel adsorption processes is that, it is capable of characterizing the effects of matrix molecules on mineralization by using very small quantities of material. Again due to constraints of stirring and evaporation, it is difficult to reduce the volume of a solution reaction to less than a few milliliters without the use of gels. On the other hand, a biomolecule can be dissolved or suspended in a small volume of gel where it is ‘‘trapped’’ by diffusion [3.45], allowing precipitation studies to be done in 100 μL or less. In conclusion, we have shown that gel-diffusion-precipitation systems are the most realistic and practical of the cell-free in vitro methods of studying biomineralization processes. These methods provide a portrait of how matrix molecules act to nucleate, inhibit, or modify mineral formation, and how the structural features of these molecules affect the mineralization process. We have shown the versatility of this process by characterizing eight different biologically important minerals from agar-agar and agarose gel matrix. It is speculated that both agar-agar and agarose gels mainly play a role of control on the diffusion process of reactant ions, which might have relevant biological implications.

References:

[3.1] G. Krampitz, G. Graser, Angew. Chem. Int. Ed. Engl. 27 (1988) 1145.

[3.2] (a) G. S. Attard, P. N. Bartlett, N. R. B. Coleman, J. M. Elliott, J. R. Owen, J. Wang, Science 278 (1997) 838, (b) C. J. Brinker, Curr. Opin. Colloid In. 3 (1998) 166, (c) C. T. Kresge, M. E. Leonowicz, W. J. Roth, J. C. Vartuli, J. S. Beck, Nature 359 (1992) 710, (d) C. B. Murray, C. R. Kagan, M. G. Bawendi, Science**,** 270 (1995)1335, (e) P. V. Braun, S. I. Stupp, Scienc 277 (1997) 1242, (f) W. Shenton, D. Pum, U. B. Sleytr, S. Mann, Nature 389 (1997) 585.

[3.3] S. Mann, Biomineralization, Principles and Concepts in Bioinorganic Materials Chemistry, Oxford Chemistry Masters, Oxford University Press: UK (2001).

[3.4] J. T. Hana, X. Xub, K. Cho, J. Cryst. Growth 308 (2007) 110.

[3.5] (a) S. Kawaii, Y. Tomono, E. Katase, K. Ogawa, M. Yano, J. Agric. Food Chem.47 (1999) 3565, (b) A Sass-Kiss, M. Sass, J. Agric. Food Chem. 50 (2002**)** 2117.

[3.6] M. M. Bradford, Anal. Biochem. 72 (1976) 248.

[3.7] M. E. Böttcher, P. Gehlken, D. F. Steele, Solid State Ionics 101 (1997) 1379.

[3.8] H. Elfil, H. Roques, Desalination 137 (2001) 177.

[3.9] K. Nakamoto, Intrared and Ramman Spectra of Inorganic and Coordination Compounds. 5th Ed. John Wiley & Sons. Inc. New York, (1997).

[3.10] (a) S. Gunasekaran, R. Rajkumar, Asian J. Phys. 9 (2000) 50, (b) N. Srinivasan, S. Natarajan, Indian J. Phys. 70A (1996) 563.

[3.11] Y. G. Socrates, Infrared Characteristic Group Frequencies, John-Wiley, Chichester, (1980).

[3.12] (a) J. D. Hartgerink, E. Beniash, S. I. Stupp, Science 294 (2001) 1684, (b) E. Baeuerlein, Biomineralization: From Biology to Biotechnology and Medical Application, Wiley-VCH (2000), (c) H. A. Lowenstam,. S. Weiner, On Biomineralization, Oxford University Press, U.K. (1989), (d) S. Mann, Biomineralization, Oxford University Press, U.K., (2001), (e) K. Simkiss, K. M. Wilbur, Biomineralization: Cell Biology and Mineral Deposition, Academic Press, San Diego, CA (1989).

[3.13] S. Stocks-Fischer, J. K. Galinat, S. S. Bang, Biol. Biochem. 31 (1999) 1563.

[3.14] (a) E. Blackwelder, Proc. Natl. Acad. Sci. U.S.A. 11 (1916) 490, (b) L. Cayeux, C. R. Acad. Sci., Paris 23 (1936) 1198.

[3.15] E. Boquet, A. Boronat, A. Ramos-Cormenzana, Nature 246 (1973) 527.

[3.16] (a) R. Doetsch, T. M. Cook, Introduction to Bacteria and Their Ecobiology. Medical and Technical Publishing, Lancaster, UK (1973), (b) H. L. Ehrlich, Geomicrobiology, Marcel Dekker, NewYork, (1996).

[3.17] (a) K. O. Konhauser, FEMS Microbiology Reviews 20 (1997) 315, (b) H. A. Lowenstam, S. Weiner, On Mineralization, Oxford University Press, New York, NY, (1989).

[3.18] B. Nair, T. Pradeep, Cryst. Growth Des. 2 (2002) 293.

[3.19] P. M. Halami, A. Ramesh, A. Chandrashekar, World J. Microb. Biot. 21 (2005) 1351.

[3.20] M. M. Bradford, Anal. Biochem. 72 (1976) 248.

[3.21] A. L. Boskey, J. Cell. Biochem. Suppl. 30/31 (1998) 83.

[3.22] R. A. Keates, F. R. Hallett, Science 241 (1988) 1642.

[3.23] H. Elfil, H. Roques, Desalination 137 (2001) 177.

[3.24] (a) I. Sondi, B. Salopek-Sondi, Langmuir 21 (2005) 8876, (b) A. C. Mitchell, F. G. Ferris, Environ. Sci. Technol. 40 (2006) 1008.

[3.25] N. Moszner, U. Salz, V. Rheinberger, U. S. 5733968 (March 1998).

[3.26] S. Mann, Angew. Chem. Int. Ed., 39 (2000) 3392.

[3.27] L. Silverman, A. L. Boskey, Calcified Tissue Int. 75 (2004) 494.

[3,28] (a) G. Falini, S. Fermani, M. Gazzano A. Ripamonti, Chem. Eur. J. 3 (1997) 1807, (b) G. Falini, S. Fermani, M. Gazzano, A. Ripamonti, Dalton Trans. (2000) 3983.

[3.29] O. Grassmann, G. Müller, P. Löbmann, Chem. Mater. 14 (2002) 4530.

[3.30] H. K. Henisch, Crystals in gels and liesegang rings, Cambridge University Press; Cambridge: (1988).

[3.31] (a) S. Boggavarapu, J. Chang, P. Calvert, Mater. Sci. Eng. C, 11 (2000) 47, (b) Y. Levi-Kalisman, G. Falini, L. Addadi , S. Weiner, J. Struct. Biol. 135 (2001) 8.

[3.32] (a) N. A. Peppas, Y. Huang, M. Tottes-Lugo, J. H. Ward, J. Zhang, Ann. Rev. Biomed. Eng., 2 (2000) 9, (b) R. Langer, Acc. Chem. Res. 33 (2000) 94.

[3.33] V. Normand, D. L. Lootens, E. Amici, K. P. Plucknett, P. Aymard, Biomacromolecules 1 (2000) 730.

[3.34] D. Yang, L. Qi, J. Ma, Chem. Commun. (2003) 1180.

[3.35] C. I. D. Bica, R. Borsali, E. Geissler, C. Rochas, Macromolecules 34 (2001) 5275.

[3.6] G. K. Hunter, C. L. Kyle, H. A. Goldberg, Biochem. J. 300 (1994) 723.

[3.37] H. A. Goldberg, K. J. Warner, M. J. Stillman, G. K. Hunter, Connect Tissue Res. 35 (1996) 385.

[3.38] N. Pernodet. M. Maaloum. B. Tinland. Electrophoresis 18 (1997) 55.

[3.39] M. E. Böttcher, P. Gehlken, D. F. Steele, Solid State Ionics, 101 (1997) 1379.

[3.40] K. Nakamoto, Intrared and Ramman Spectra of Inorganic and Coordination Compounds, 5th Ed. John Wiley & Sons. Inc. New York (1997).

[3.41] (a) N. Srinivasan, S. Natarajan, Indian J. Phys. 70A (1996) 563, (b) S. Gunasekaran, R. Rajkumar, Asian J. Phys. 9 (2000) 50.

[3.42] Y. G. Socrates, Infrared Characteristic Group Frequencies, John-Wiley, Chichester, (1980).

[3.43] A. Sugawara, T. Kato, Chem. Commun., (2000) 487.

[3.44] D. W. Renn, Ind. Eng. Chem. Prod. Res. Dev., 23 (1984) 17.

[3.45] A. L. Boskey, M. Maresca, W. Ullrich, S. B. Doty, W. T. Butler, C. W. Prince, Bone Miner. 22 (1993) 147.

Chapter - 4

Precursor synthesis and applications of inorganic materials

4.1. Synthesis and application of metal oxides

The fabrication of assemblies of perfect nano to micrometer scale crystallites identically replicated in unlimited quantities is the ultimate challenge of materials research with outstanding fundamental and potential technological prospects [4.1]. Among the various inorganic materials, transition metal oxides and zinc oxide have attracted increasing technological and industrial interest and are widely used. Macroporous materials are of particular interest for applications such as separation and purification processes, supported catalysis, drug delivery, heavy metal trapping, smart fillers, *etc*. There are two main synthetic approaches that generally are used for the synthesis of macroporous materials [4.2]. In the first method, structure directing agents, typically in the form of supramolecular surfactant aggregates, are used as porogens, and a porous material is obtained after removal of the surfactant by combustion or by ion-exchange. In the second method, porous solid molds are used as sacrificial templates. Inorganic condensation reaction occurs in those pores or on the outer surface of the mold, and subsequently the mold is selectively removed in order to generate the porosity.

In the final chapter, a simple solid-state, environmentally benign chemical approach for the efficient synthesis of useful amounts of various macroporous metal oxides by thermolysis of the precursor salts of the organic acids has been reported. Metal precursor salts of different aliphatic organic acids were synthesized by simple solid-state synthesis. Such synthetic methodology is easy, quantitative and reproducible. Thermolysis of this precursor salts lead to the formation of macroporous metal oxides. Precursor-complex controlled mineral synthesis is a versatile tool toward inorganic mineral crystal morphogenesis and understanding of the self-assembly of solid-state superstructures in the formation of inorganic minerals. These macroporous metal oxides are used as a heterogeneous catalyst for various organic transformations (Scheme 4.1) [4.3]. A detailed analysis of the microstructural properties as well as magnetic and photoluminescence (PL) behavior of these metal oxides has been reported. Comparative studies of the formation of macroporous metal oxides have been discussed.

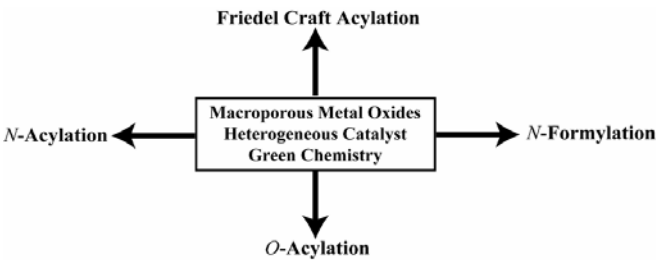

Scheme 4.1. Macroporous Metal Oxides as a heterogeneous catalyst for various organic transformations.

4.1.1. Experimental section

Materials

Freshly prepared metal hydroxide was used. Oxalic acid (OA), malonic acid (MA), succinic acid (SA), stearic acid (SA), trimesic acid (TMA), fluorescein, bovin serum albumin (BSA) used were analytically pure. The water used in the experiment was the Milli-Q water.

Structural characterization

Scanning electron micrograph (SEM) images were obtained by *LEO-1430 VP* electron microscope on samples glued on an aluminum stub and sputtered with gold. FT-IR analysis was carried out on air-dried samples. All IR spectra were recorded at 4 cm^{-1} resolution with 10 scan with a *Perkin Elmer-Spectrum One FT-IR Spectrometer* from 4000 to 450 cm^{-1}. A background spectrum was measured for pure KBr. To confirm the crystalline nature as well as the phase of the sample, PXRD data were recorded with *Seifert powder X-ray diffractometer (XRD 3003TT)* with CuK_α source (λ = 1.54 Å) on glass surface of air-dried sample. The room-temperature photoluminescence (PL) spectra were obtained on a *Varian Cary Eclipse luminescence* spectrometer with a Xe lamp as the excitation source. Room temperature magnetization was measured using a vibrating sample magnetometer (VSM, Lakeshore 7410). The VSM was calibrated using a standard reference (high-purity nickel sphere), supplied with the instrument. The magnetic hysteresis loop was obtained by using external magnetic fields of ± 20 kOe (kA/m).

General synthesis of metal-organic precursor salts

The metal-organic precursor salts were prepared by simple solid-state room temperature grinding methods. As shown in the scheme 4.2, the organic acid helps in the formation of solid state self assembled 3D superstructure in the solid-state which on thermolysis *via* calcination-reconstruction process form macroporous metal oxides. We have used three aliphatic organic acids (OA, MA, SA). This solvent-free solid-state method has an operationally simple and green in nature. In a typical experiment, a 2:1 mixture of organic acid and freshly prepared $M(OH)_n$ were ground with a pestle in a mortar at RT in open atmosphere until the mixture turned into a melt. The melt was then washed several times with cold 1% NaOH solution. Solid salt thus obtained were air dried in before characterization.

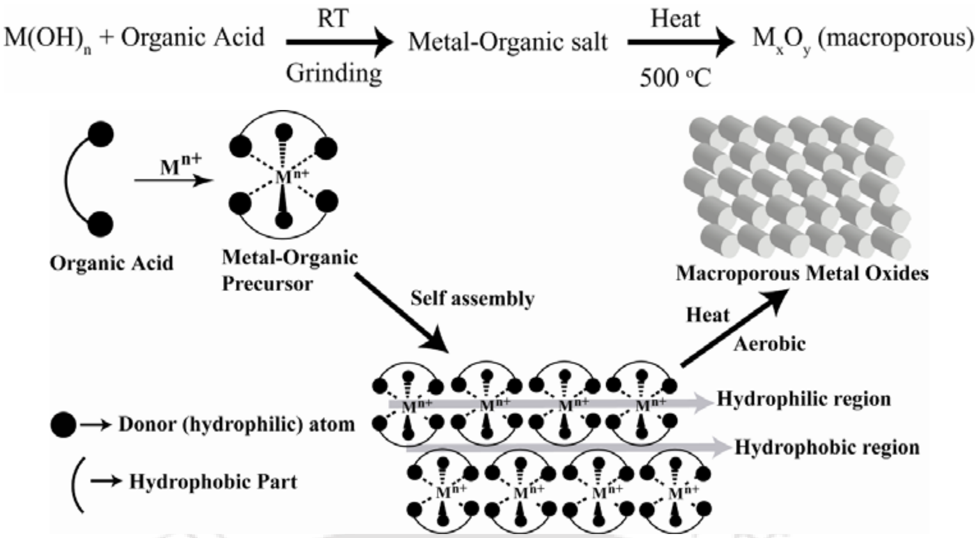

Scheme 4.2. Macroporous Metal Oxides on thermolysis of precursor salt.

General synthesis of macroporous metal oxide

Macroporous metal oxide were prepared by thermal decomposition of metal-organic precursor salts (Scheme 4.2). Precursor salts were heated at 500 ^{o}C for 6 h in muffle furnace to get thermally decomposed micro crystalline macroporous metal oxides. The results were shown schematically in scheme 4.3.

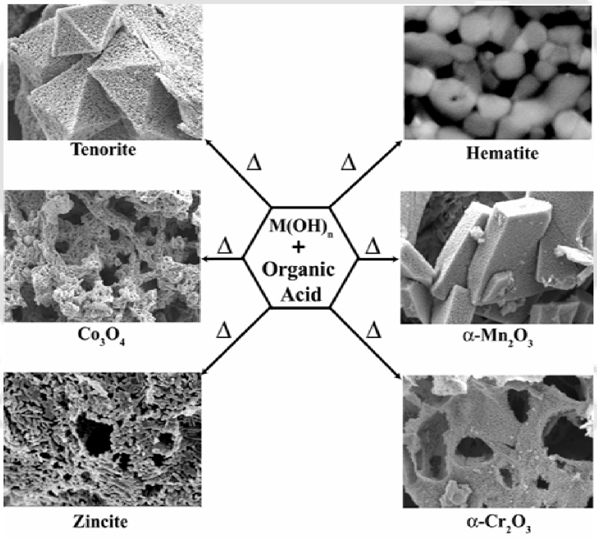

Scheme 4.3. Macroporous metal oxides obtained by thermal decomposition of precursor complex.

4.1.2. Result and discussion

Metal-organic precursor salts

As mentioned above, these salts were prepared in a simple, quantitative and reproducible solid phase synthetic route by simply grinding freshly prepared $M(OH)_n$ with various organic acids (Table 4.1). PXRD pattern of the Zn-precursor salt is shown

Table 4.1. Solid phase synthesis of various metal-organic precursor salts

Entry	Metal salts	Organic Acids	Yield (%)^a
1	$Zn(OH)_2$	Oxalic acid	98
2		Malonic acid	98
3		Suiccinic acid	97
4	$Cu(OH)_2$	Oxalic acid	98
5		Malonic acid	98
6		Suiccinic acid	98
7	$Ni(OH)_2$	Oxalic acid	96
8		Malonic acid	96
9		Suiccinic acid	96
10	$Co(OH)_2$	Oxalic acid	96
11		Malonic acid	97
12		Suiccinic acid	97
13	$Fe(OH)_3$	Oxalic acid	98
14		Malonic acid	97
15		Suiccinic acid	97
16	$Mn(OH)_2$	Oxalic acid	96
17		Malonic acid	95
18		Suiccinic acid	95
19	$Cr(OH)_3$	Oxalic acid	95
20		Malonic acid	94
21		Suiccinic acid	94

^{a} yield of the isolated product

in Figure 4.1. PXRD pattern of the precursor salts of other metals are provided in the Appendix 1 (Figure 4.1A-4.6A). PXRD pattern proves the bulk crystalline nature of all these precursor salts. Thermo gravimetric analysis of the as-prepared various precursor salt confirmed presence of organic acids in the bulk samples and it also confirms the formation of the corresponding metal oxides. Hence, all the precursor salts are forming micro-crystalline metal-carboxylate complexes of different crystalline phases. Representative TGA-DSC profile of as prepared Zn-precursor salt and Fe-precursor salt is shown in Figure 4.2a and 4.2b respectively.

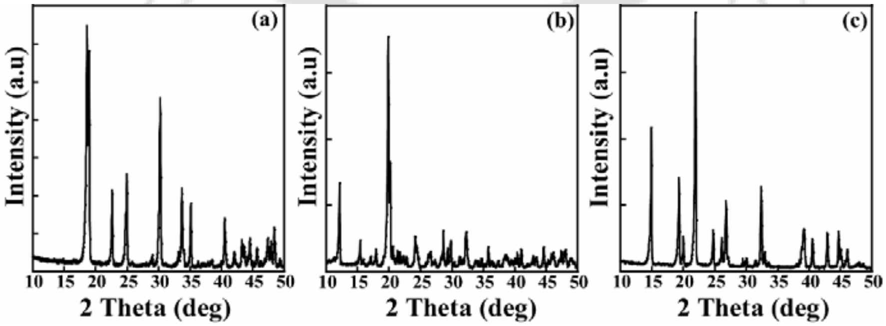

Figure 4.1. PXRD of the precursor salt of Zn with (a) OA, (b) Ma and (c) SA.

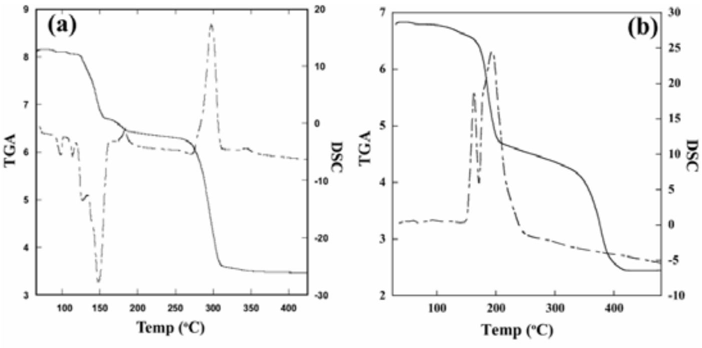

Figure 4.2. Representative TGA-DSC of the precursor salt of (a) Zn with OA and (b) Fe with SA.

FT-IR analysis of the precursor salt before and after heating

It is expected from the difference of structure of the starting organic acids. The FT-IR spectrum of all the precursor salts show a broad band centered on 3300 cm^{-1} due to the presence of water molecules (Figure 4.3). From FT-IR analysis it is also obvious that each precursor salt contains two types of carboxylic acid groups. One of which is uncoordinated, unionized and other one is coordinated, ionized. FT-IR spectrum clearly shows the presence of coordinated, ionized –COO- in the range of 1650-1590 cm^{-1}, which comprise well with the literature values [4.4]. The FT-IR spectrum of CuO appeared weak adsorptions at 3466 and 1629 cm^{-1}, and strong adsorptions at 596. The bands at 3466 and 1629 cm^{-1} could be attributed to the stretching vibration and bending vibration of absorbed water and surface hydroxyls, and those at 596 confirmed the formation of monoclinic CuO phase [4.4, 4.5].

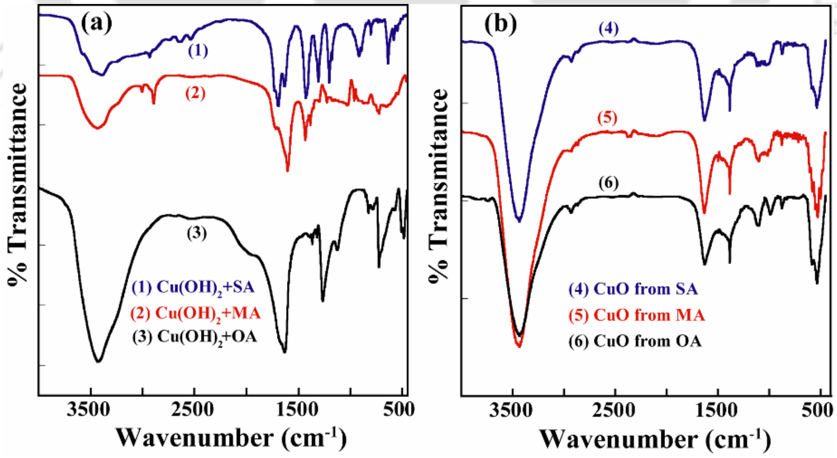

Figure 4.3. FT-IR of the Cu-organic acid precursor salt (a) before heating and (b) after heating.

In case of NiO (Figure 4.7A in appendix), the broad absorption in 3340 and 1630 cm^{-1} is assigned to the existence of water and the product has strong absorption ability for moisture. The absorption band at 420 cm^{-1} is Ni–O stretching vibration mode. [4.6]. The

FT-IR spectrum of Co_3O_4 is shown in Figure 4.8A in appendix. The absorption peaks at 666 and 572 cm^{-1} are assigned to υ (Co-O) modes [4.7], which confirms the formation of Co_3O_4. The broad band centered at 3455 cm^{-1} and the peak at 1633 cm^{-1} corresponds to the stretching and bending modes of hydroxyls respectively [4.8]. In the Figure 4.9A in appendix, the peaks at about 3438 and 1638 cm^{-1} can be assigned to $\nu_{O\text{-}H}$ stretching vibration and bending vibration of water molecules adsorbed by the Mn_2O_3 products, respectively [4.9]. The peaks around 666 and 571 were attributed to $\nu_{Mn\text{-}O}$ stretching vibration of Mn_2O_3, 514 cm^{-1} were attributed to $\nu_{Mn\text{-}O}$ bending vibration of Mn_2O_3 [4.10]. The FT-IR spectra of pure chromium oxide (Figure 4.10A in appendix) present relatively smaller number of absorption bands in the measured spectral range. The absorption bands located at 630 and 573 cm^{-1} are assigned to Cr–O bond [4.11]. The absorption band at 1102 cm^{-1} detected in the spectra of both Cr_2O_3, obtained at the two oxygen amounts can be associated with the chromyl (Cr-O) vibration [4.12].

Formation of macroporous ZnO micro structures

Regardless of the starting Zn (II) - organic acid precursor salt, on thermal decomposition *i.e,* on heating at 500 °C for 6 hrs we got macroporous Zincite micro crystallites of different surface morphologies. SEM micrographs (Figure 4.4a-4.4c) shows macroporous ZnO with average pore size in the range 30 – 100 nm. In each case the morphology of the micro crystallites is different. Layers of porous ZnO sheets of size range 80-150 nm are obtained from malonic acid salt. Spheroids of ZnO with average diameter of 100 nm are obtained from succinic and oxalic acid precursor salt. Oxalic acid precursor salt gives best porous materials. Here it is formed by random assembly of ZnO nano rods with an average aspect ratio of ~ 10 nm. The X-ray phase analysis of the bulk samples is given in Figure 4.4d. The diffraction patterns are in good agreement with those of a bulk ZnO with the hexagonal zincite structure (PDF: 01-089-7102) [4.13]. UV-Vis absorption study of ZnO obtained by thermolysis of all Zn-organic precursor salts were carried out in dry THF as dispersion. Figure 4.4e is the representative UV–Vis absorption spectra of ZnO micro crystals. In all cases, it shows a strong absorption in the range of 400–300 nm and a peak appears at the 378 nm with slight variation in the absorbance. The calculated band gap energy (3.28 eV) corresponds to the wide band gap semiconductor nature of the ZnO micro crystals. The room-temperature photoluminescence (PL) studies clearly show that ZnO is a strong fluorescence active material. The PL spectrum of the sample shown in Figure 4.4f shows strong UV emission at 420 nm at room temperature is attributed to the radiative annihilation of excitons [4.14]. PL spectrum also shows weak blue-green emission at 485 nm and weak yellow-green emission at 518 nm of the visible region which is attributed to singly ionized oxygen vacancy in ZnO and results from the recombination of a photon-generated hole with the single ionized charge state of this defect [4.15]. The weak blue-green emission may originate from the electron transition from the level of the ionized oxygen vacancies to the valence band. Usually the green PL arises from oxygen deficient samples possessing a porous structure [4.16]. Therefore, this particular UV emission behavior may be related to the porous morphology of the ZnO.

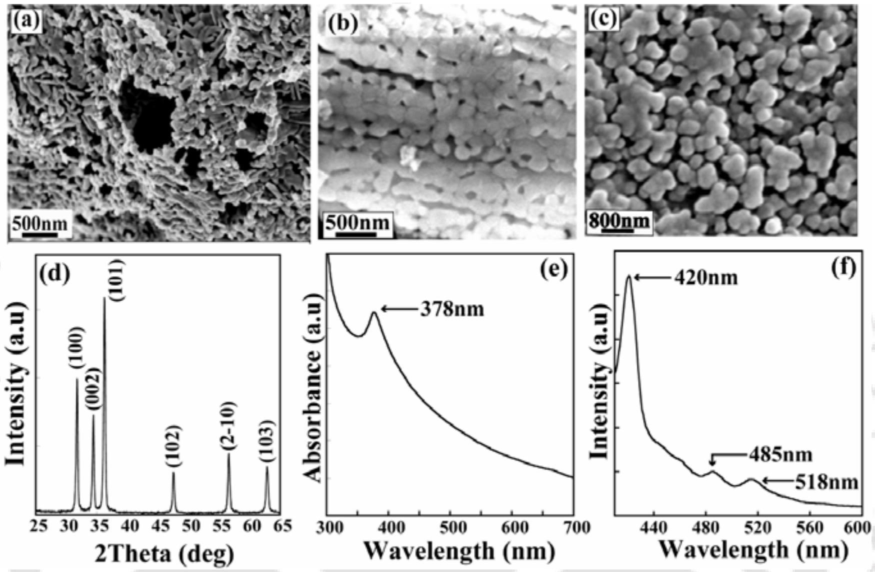

Figure 4.4. SEM micrograph of ZnO by thermolysis of precursor salt with (a) OA, (b) MA, (c) SA, (d) PXRD pattern of ZnO, (e) UV-Visible absorption spectrum (λ_{max}= 378 nm) and (f) PL spectrum of ZnO.

Formation of macroporous CuO micro structures

On thermal decomposition of Cu-precursor salts we got highly porous Tenorite (CuO) octahedrons. SEM micrographs (Figure 4.5a-4.5c) shows the formation of macroporous CuO with an average pore size of <100 nm. The PXRD pattern (Figure 4.5d) confirms the formation of the tenorite phase of CuO with characteristic PXRD pattern at 2θ = 35.55 correspond to (-111) plane, 38.75 correspond to (111) plan (PDF: 72-629). The VSM studies (Figure 4.5e) shows hysteresis loop. From initial slop, the magnetic susceptibility $\chi = M / H$ was found to be 43.13 x 10^{-6} emu /gOe with coercive force (H_c) 572 Oe at T = 300 K. These values indicate the presence of macroporous nature of solid CuO. These micro-crystalline tenorite phase exhibit an anomalous ferromagnetic behavior which is rare for CuO particle with size ≥ 10 nm. This is because the particles with size ≥ 10 nm resemble that of bulk CuO and the bulk CuO is a class of anti-ferromagnetic material [4.17]. It is claimed that the uncompensated surface spins produce a ferromagnetic/anti-ferromagnetic (FM/AF) interface in the pure anti-ferromagnetic nanoparticles (AFN), resulting in a shifted hysteretic loop of the ferromagnetic surface spins, due to a bias produced by exchange coupling to the AF spins. Macroporous materials has large specific surface area and this results in more uncompensated surface spins, which will ultimately leads to more exchange bias [4.17].

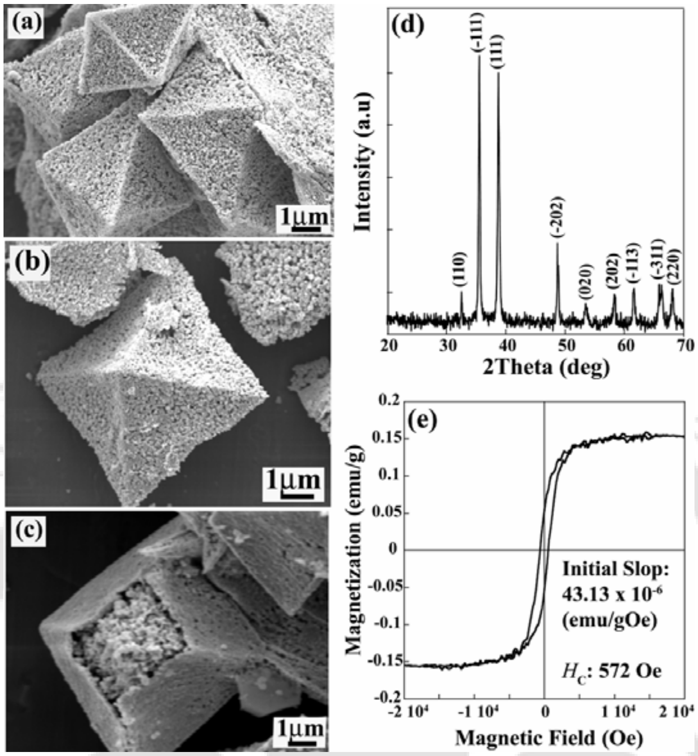

Figure 4.5. SEM micrograph of CuO by thermolysis of precursor salt with (a) OA, (b) MA, (c) SA, (d) PXRD pattern of CuO and (e) VSM of CuO.

Formation of macroporous NiO micro structures

On thermal decomposition at 500°C for 6 hrs we obtain macroporous NiO. SEM micrographs (Figure 4.6a-4.6c) shows that all Ni-precursor salts resulted in the formation of similar porous plate like morphology with an average pore size in the range 80-200 nm. The PXRD pattern (Figure 4.6d) confirms the formation of crystalline NiO with characteristic PXRD pattern at $2\theta = 37.32$ correspond to (111) plane, 43.41 correspond to (200) plan and 62.98 correspond to (220) (PDF: 72-629). The VSM studies (Figure 4.6e) shows hysteresis behavior with a very small hysteresis loop. From initial slop, the magnetic susceptibility (χ) was found to be 1.22×10^{-3} emu /gOe with low coercive force (H_c) 142 Oe at $T = 300$ K and it is described as anti-ferromagnetic material as NiO with reduced particle size of below 100 nm behaves as super paramagnetic or weak ferromagnetic [4.18a]. NiO is a potential material for room temperature spin-valve device applications because of its Neel temperature (T_N) being 523K [4.18b].

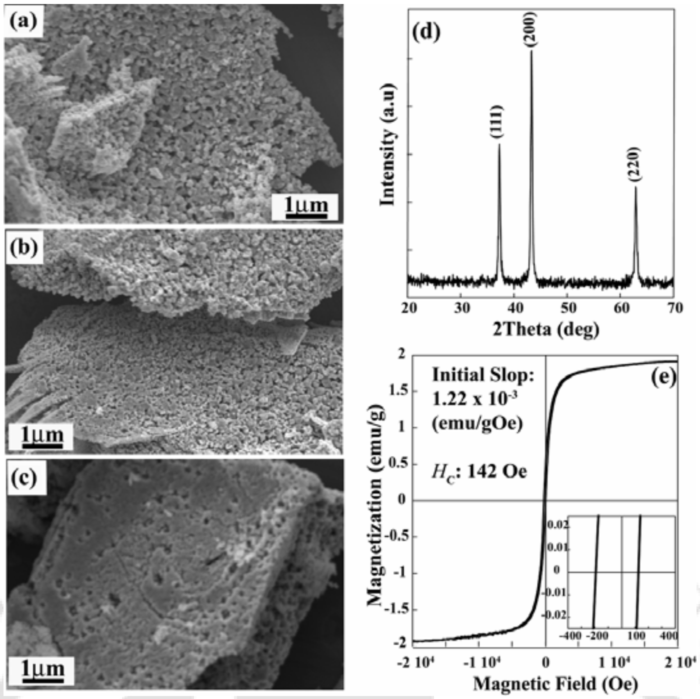

Figure 4.6. SEM micrograph of NiO by thermolysis of precursor salt with (a) OA, (b) MA, (c) SA, (d) PXRD pattern of NiO and (e) VSM of NiO.

Formation of macroporous Co_3O_4 micro structures

Here also regardless of the starting Co-organic precursor salts, on thermal decomposition at we got micro-crystalline macroporous spinel Co_3O_4. However, unlike the previous cases, here we got oxides of with different surface morphologies. Co-oxalic acid precursor salt form macroporous spinel Co_3O_4 seeds with pore size in the range 200-300 nm aggregates again to form a porous network of 1-2 µm in length (Figure 4.7a). Figure 4.7b shows macroporous Co_3O_4 needles with pore size in the range 100-200 nm obtained from the precursor salt with MA whic aggregates again to forms a porous aggregate of 1 µm. SA precursor salt forms macroporous Co_3O_4 with average pore size of 150 nm (Figure 4.7c). The PXRD pattern shown in the Figure 4.7d confirms the formation of spinel $CoCo_2O_4$ with characteristic PXRD pattern at $2\theta = 31.95$ correspond to (200) plane, 36.93 correspond to (311) plane, 59.9 correspond to (511) plan and 67.5 correspond to (440) (PDF: 01-1152). The VSM studies Figure 4.7e shows hysteresis behavior with a very small hysteresis loop. From initial slop, the magnetic susceptibility (χ) was found to be 45.68×10^{-6} emu /gOe with coercive force (H_c) 200 Oe at $T = 300$ K which is similar to those of Co_3O_4 particles reported in the literature [4.19]. Lack of saturation magnetization even at a high field of 20 kOe clearly shows antiferromagnetic nature of synthesized Co_3O_4.

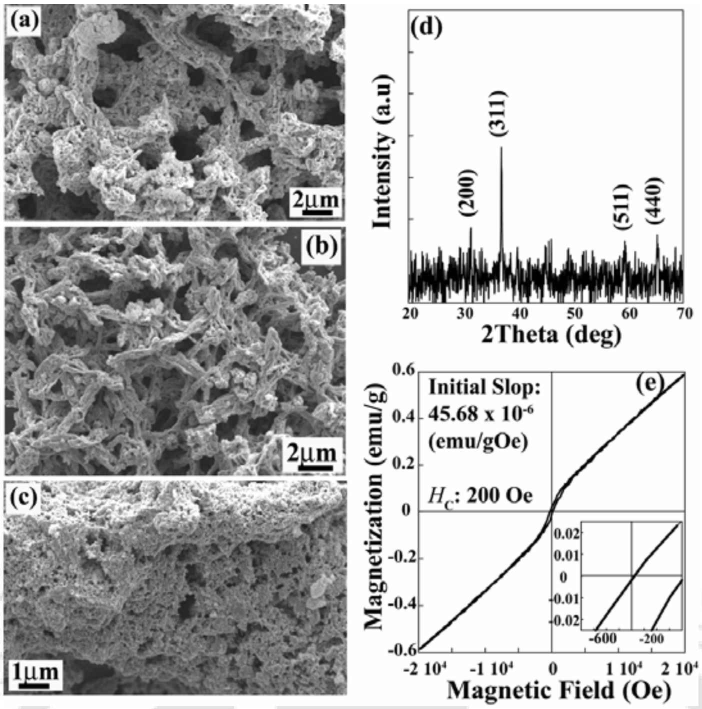

Figure 4.7. SEM micrograph of Co_3O_4 by thermolysis of precursor salt with (a) OA, (b) MA, (c) SA, (d) PXRD pattern of Co_3O_4 and (e) VSM of Co_3O_4.

Formation of macroporous α-Fe_2O_3 micro structures

In case of Fe-organic acid salts we got macroporous Hematite micro crystallites. In this case the morphology of the micro crystallites is different. α-Fe_2O_3 derived from OA form assembly of α-Fe_2O_3 spheroids with an average diameter of 200 nm (Figure 4.8a) whereas MA salt and SA salt form macroporous micro rods of thickness range of 1-1.5 μm and each pore diameter in the range of 70-150 nm (Figure 4.8b-4.8c) . The PXRD analysis of the is shown in Figure 4.18d. Strong reflect at $2\theta = 33.15$ (1 0 4) and at 35.59 (1 1 0) and some other prominent peaks at 24.13 (0 1 2), 40.83 (1 1 3), 49.43 (0 2 4), 54.04 (1 1 6), 62.38 (2 1 4) and 63.93 (3 0 0). The diffraction patterns are in good agreement with those of α-Fe_2O_3 with the Hematite (syn) (PDF: 01-089-8104). The VSM studies Figure 4.8e shows hysterisis behaviour. From initial slop, the χ was found to be 1.09×10^{-3} emu /gOe with high coercive force (H_c) 817 Oe at $T = 300$ K. In bulk hematite below the Neel temperature TN ($948 < T\text{N} < 963$ K) [4.20a], the Morin transition takes place as a first order magnetic transition at the temperature T_M ~263K [4.20a, 4.20b]. Below T_M spins are oriented in antiparallel directions along the trigonal (1 1 1) axis (*c*-axis), and the material behaves as a uniaxial antiferromagnet [4.20c]. Above T_M, spins show slight canting with respect to the basal (1 1 1) plane and a small net magnetic moment appears (weak ferromagnetism).

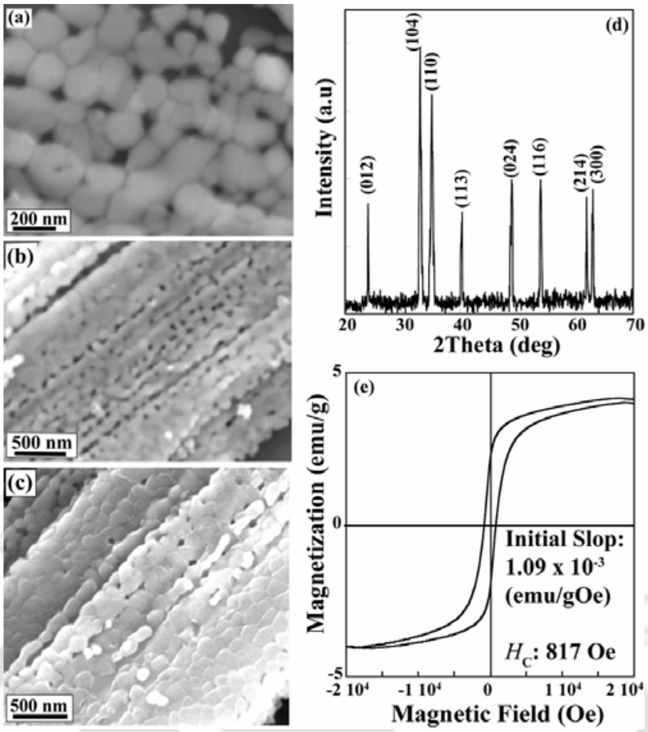

Figure 4.8. SEM micrograph of α-Fe_2O_3 by thermolysis of precursor salt with (a) OA, (b) MA, (c) SA, (d) PXRD pattern of α-Fe_2O_3 and (e) VSM of α-Fe_2O_3.

Formation of macroporous α-Mn_2O_3 micro structures

On thermal decomposition of different Mn-organic precursor salts we got macroporous α-Mn_2O_3. In this case we got different morphology of α-Mn_2O_3. Mn-oxalic acid precursor salt, we got beautiful uniformly arranged macroporous rectangular plates of average thickness of 1 μm and average pore size in the dimension of 100 nm (Figure 4.9a). Figure 4.9b shows the formation of macroporous thin plates of average pore size 150 nm from Mn-malonic acid precursor salt. However, Mn-succinic acid precursor salt is results in the formation of macroporous α-Mn_2O_3 without any regular shape (Figure 4.9c). PXRD pattern shown in the Figure 4.9d confirms the formation of α-Mn_2O_3 with characteristic PXRD pattern at $2\theta = 32.90$ correspond to (222) plane and 55.29 correspond to (440) plane, 59.9 correspond to (511) plan (PDF: 02-896). The VSM studies Figure 4.9e shows that the compound is paramagnetic as magnetic saturation or hysterisis loop is absent. This is because α-Mn_2O_3 is having $T_N \approx 90$ K and it is paramagnetic above its T_N [4.21]. From initial slop, the magnetic susceptibility (χ) was found to be 93.45 x 10^{-6} emu /gOe.

Formation of macroporous Cr_2O_3 micro structures

Figure 4.10a-4.10c shows SEM micrograph of macroporous Cr_2O_3 obtained bythermolysis of Cr-oxalic, malonic and succinic salts respectively. In each case the average pore size is in the range 50-80 nm. The PXRD pattern shown in the Figure 4.10d confirms the formation of Cr_2O_3 with characteristic PXRD pattern at $2\theta = 33.53$ correspond to (104) plane, 36.34 correspond to (110) plane and 54.94 correspond to (116) plane (PDF: 01-1294). The VSM studies Figure 4.10e shows hysteresis behavior with a very small hysteresis loop. From initial slop, the magnetic susceptibility (χ) was found to be 53.96 x 10^{-6} emu /gOe with low coercive force (H_c) 173 Oe at $T = 300$ K and exhibits an itinerant anti-ferromagnetic phase below the Neel temperature ($T_N = 311$ K) [4.22].

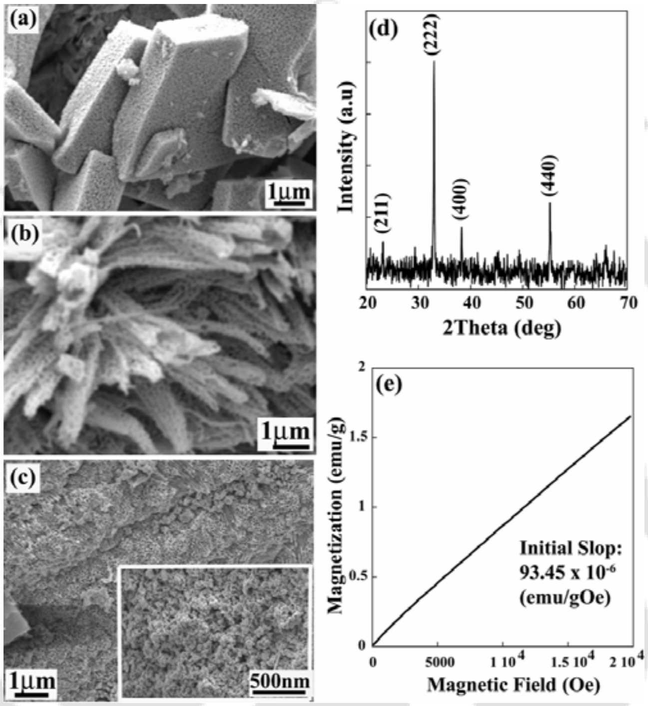

Figure 4.9. SEM micrograph of α-Mn_2O_3 by thermolysis of precursor salt with (a) OA, (b) MA, (c) SA, (d) PXRD pattern of α-Mn_2O_3 and (e) VSM of α-Mn_2O_3.

4.1.3. Summary

In summary, we have shown the simple, solid-phase efficient, green synthesis of several metal-organic precursor salts. All three aliphatic organic acids form micro-crystalline metal-carboxylate complexes of different crystal packing. Macroporous metal oxides have been successfully prepared by thermal decomposition of these precursor salts in solid-state. We have done detail comparison of 21 different thermally decomposed products. We have observed that regardless of the starting aliphatic organic acid, on thermal decomposition we got macroporous metal oxides. Hence, we can conclude that the molecular level interaction of carboxylic acid groups with metal ion in the solid-state are solely responsible for the formation of corresponding metal oxides. Backbone structure of the organic acid has negligible effect on the modification of the morphology of the thermally decomposed product. Thus, we can conclude the particle agglomeration process during calcinations is dependent on the coordination environment at the molecular level.

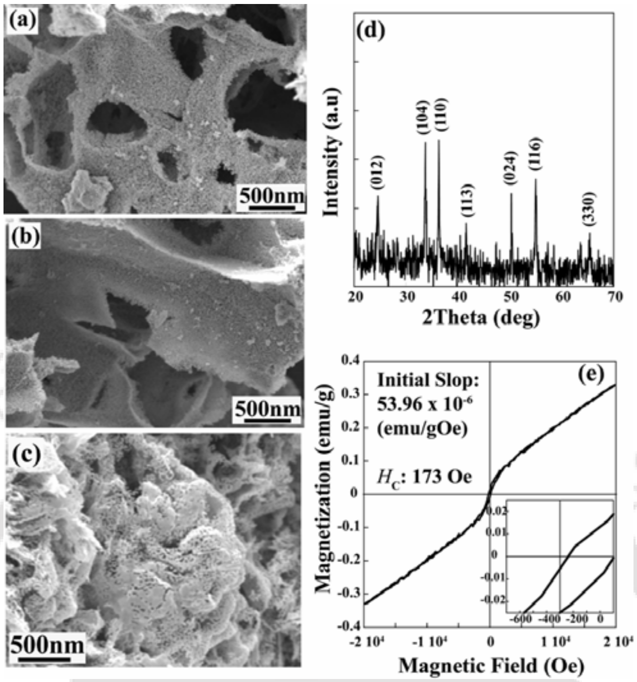

Figure 4.10. SEM micrograph of Cr_2O_3 by thermolysis of precursor salt with (a) OA, (b) MA, (c) SA, (d) PXRD pattern of Cr_2O_3 and (e) VSM of Cr_2O_3.

4.2. Synthesis and application of Soft Metal Ferrites

Spinel of the type $M^{2+}M_2^{3+}O_4$ attract the research interest because of their versatile practical applications [4.23]. In the case of M^{3+} = Fe, the resulting cubic spinel structured ferrites having a general chemical composition of $MO{\cdot}Fe_2O_3$ (M=Fe, Mn, Co, Ni, Zn) are among the most frequently used systems to understand fundamental aspects of nanomagnetism [4.24] and have been widely applied as magnetic materials. In this section, we have carried out a simple solid-state, environmentally benign chemical approach for the efficient synthesis of Transition metal ferrites and Zinc ferrites by thermolysis of the precursor salts of the organic acids.

4.2.1. Experimental section

Synthesis of binary Zinc-organic precursor salt

The binary metal-organic precursor salts were prepared by simple solid-state room temperature grinding methods (Scheme 4.4). The organic acid helps in the formation of solid state self assembled superstructure and on thermolysis *via* calcination-reconstruction process to microcrystalline metal ferrites. We have used oxalic acid for the synthesis of the precursor salt. This solvent-free solid-state method has an operationally simple and green procedure. In a typical experiment, 4:2 binary mixture of organic acid and freshly prepared $Zn(OH)_2$ and $Fe(OH)_3$ were thoroughly ground with a pestle in an open mortar at room temperature under open atmosphere maintaining the pH = 12 by adding excess of NaOH until the mixture turned into a melt. The melt was then washed several times with cold distilled water. Solid salt thus obtained were dried at 80 ^{o}C before characterization. Spinel zinc ferrite is prepared by thermal decomposition of metal-organic precursor salts (Scheme 4.4). Precursor salts were heated at 600 ^{o}C for 6 h in muffle furnace to get thermally decomposed nano crystalline spinel zinc ferrites.

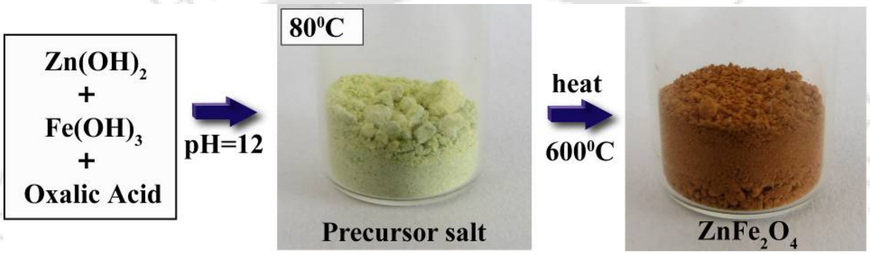

Scheme 4.4. Synthesis of Zinc ferrites by thermolysis of Zn(II)-oxalic acid precursor salts.

4.2.2. Result and discussion

Binary Zinc-organic precursor salts

As mentioned above, this salt is prepared in a simple, quantitative and reproducible solid phase synthetic route by simply grinding freshly prepared $Zn(OH)_2$ and $Fe(OH)_3$ with oxalic acids at pH of 12. The FT-IR spectrum of all the precursor salts show a broad band centered on 3300 cm^{-1} due to the presence of water molecules. From FT-IR analysis it is also obvious that each precursor salt contains two types of carboxylic acid groups. One of which is uncoordinated, unionized and other one is coordinated, ionized. FT-IR spectrum clearly shows the presence of coordinated, ionized –COO- in the range of 1650-1590 cm^{-1}, which comprise well with the literature values [4.25] (Figure 4.11).

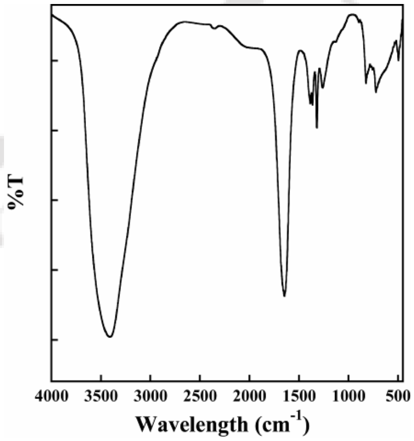

Figure 4.11. FT-IR spectrum of Zinc-oxalic acid precursor salt before heating.

Formation of Zinc Ferrite

On thermal decomposition of various binary zinc-organic precursor salts with pH of 12, we got nano crystalline zinc ferrites *i.e.* $ZnFe_2O_4$. The PXRD analysis confirms their formation with characteristic reflections at $2\theta = 30$ correspond to (220) plan, 36 correspond to (311) plan, 42 correspond to (400) plan, 58 correspond to (511) plan and 63 correspond to (440) plan which is shown in Figure 4.12a. The broad peaks suggest the nanocrystalline nature of the product. FT-IR analysis confirms the formation of the product. The band, observed at around 560 cm^{-1} for $ZnFe_2O_4$ can be assigned to tetrahedral Zn^{2+} stretching, v_1, and the band observed at 464 cm^{-1} involves the Fe^{3+} vibration at the octahedral site, v_2 (Figure 4.12b). Due to the limitation of our FTIR instrument below 400 cm^{-1}were not detected.

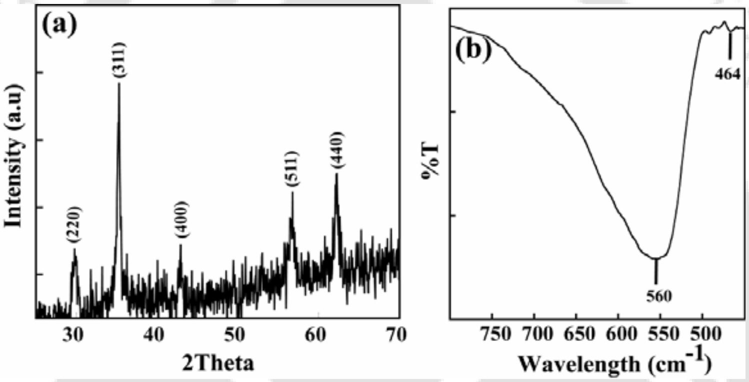

Figure 4.12. (a) PXRD pattern and (b) FT-IR spectrum of $ZnFe_2O_4$.

When we carried out the synthesis by thermal decomposition of the zinc-organic precursor salt prepared at different pH, different phases were formed. A mixture of α-Fe_2O_3 and a very small amount of ZnO phase was formed at acidic pH <7 (Figure 4.13a), whereas a mixed phase of α-Fe_2O_3 and $ZnFe_2O_4$ was detected at pH < 10 (Figure 4.13b).

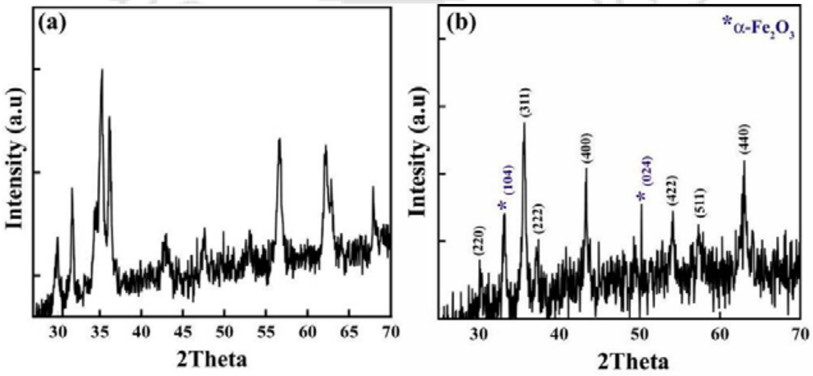

Figure 4.13. PXRD pattern of $ZnFe_2O_4$ (a) at acidic pH <7 and (b) at pH < 10.

However, the precursor salt prepared at pH=12 retained a pure zinc ferrite ($ZnFe_2O_4$) phase on thermal decomposition. The average crystallite size, *L*, was estimated by the Scherrer equation from the X-ray peak broadening (full-width at half maximum, FWHM): $\boldsymbol{L = 0.9\lambda / b \cos \theta_B}$ where λ is the wavelength of Cu K_α (1.54059 A°), θ_B is the angle of Bragg diffraction, and $\beta = B-b$. *B* is the full width at half maximum (FWHM) and *b* represents the instrumental line broadening [4.26]. Crystallite size of synthesized $ZnFe_2O_4$ powder, based on this equation, was calculated as 13.58 nm. TEM micrograph of as-synthesized zinc ferrite is given in Figure 4.14a and their particle size distribution is presented in Figure 4.14b which shows aggregation of nanoparticles. Particles are strongly aggregated despite sonication. Particles have almost spherical morphology and their size vary in the range of 6–18 nm, with almost a normal distribution centering around 12 nm. Average particle size is calculated as ~12 ± 2 nm from the TEM micrographs by counting a minimum of 100 nanoparticles.

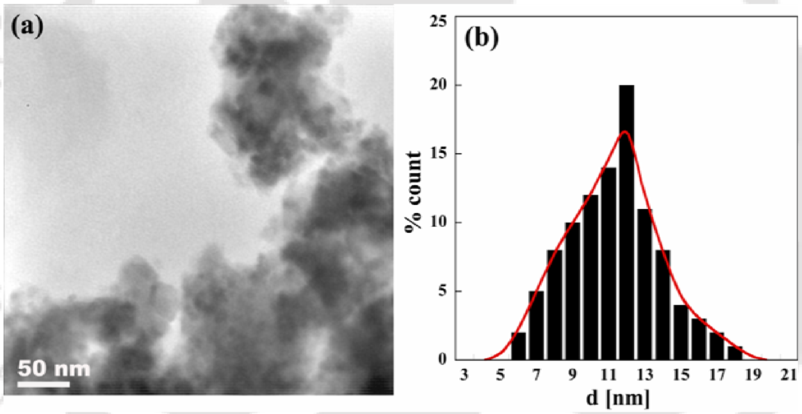

Figure 4.14. (a) TEM micrograph and (b) particle size distribution of $ZnFe_2O_4$ nanoparticles.

Magnetic measurements have been carried out by using vibrating sample magnetometer (VSM). The VSM studies (Figure 4.15a) shows S-shaped hysteresis loop. The value of magnetization sharply increases with the external magnetic field strength at low field region; however, it cannot reach a saturation state yet in the presence of a relatively strong magnetic field of even 20 kOe, which is consistent with the earlier reports [4.27]. The high field side of the curve is almost linear with the external field. This implies the co-existence of ferromagnetic and antiferromagnetic interactions. The non-saturated magnetization suggests the existence of strong antiferromagnetic inter-cluster interactions mixed with ferromagnetic interactions inside the clusters. This (co-existence of ferromagnetic and antiferromagnetic) can also cause the canted spin structures inside the clusters. By increasing the applied field, the ferromagnetic part tends to saturate, where as the antiferromagnetic part increases linearly, resulting in lack of saturation of magnetization even at 20 kOe magnetic field. From initial slop (Figure 4.11A in appedix), the magnetic susceptibility $\chi = M / H$ was found to be 1.19 x 10^{-3} emu /gOe with coercive force (H_c) 78 Oe at T = 300 K. Figure 4.15b display the M–T curves of the sample at the applied field of 100 Oe. It is found that for the ZFC curve with a measurement field of 100 Oe increases with decreasing temperature. This result is exactly matching with those of $ZnFe_2O_4$ nanoparticles reported in the literature [4.28]. Due to lack of instrumental setup, we couldn't study the M-T curve beyond 77 K.

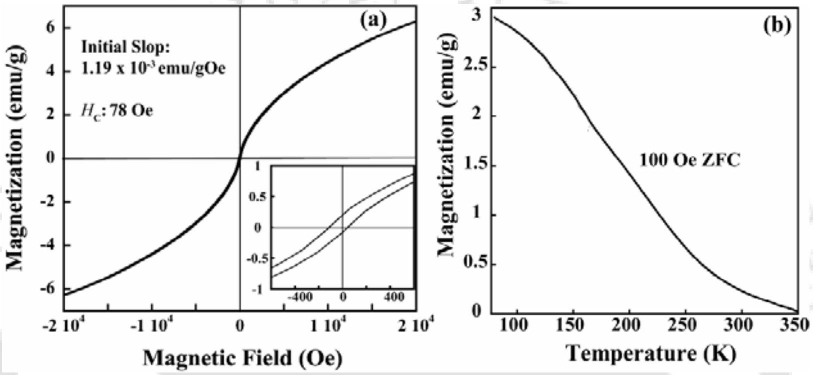

Figure 4.15. (a) Magnetic hysterisis loop and (b) M–T curves of $ZnFe_2O_4$ nanoparticle

We have extended this work by carrying out synthesis of other soft ferrites by following the same precursor synthesis method (Scheme 4.5). On thermal decomposition of various binary metal-organic precursor salts, we got micro crystalline metal ferrites *viz*: $CuFe_2O_4$, $NiFe_2O_4$, $CoFe_2O_4$ and $MnFe_2O_4$. The PXRD analysis confirms their formation with characteristic reflections at 2θ: 30 (220), 36 (311), 42 (400), 58 (511) and 63 (440) which is shown in Appendix. In case of $CuFe_2O_4$ a very small amount of CuO phase was found as impurity (Figure 4.12Ab). In case of $NiFe_2O_4$ a mixed phase of α-Fe_2O_3 and $CuFe_2O_4$ was detected (Figure 4.11Ac). This process is equally suitable for the synthesis of $CoFe_2O_4$ as evident from the PXRD with no impurities (Figure 4.12Ad). Whereas in the

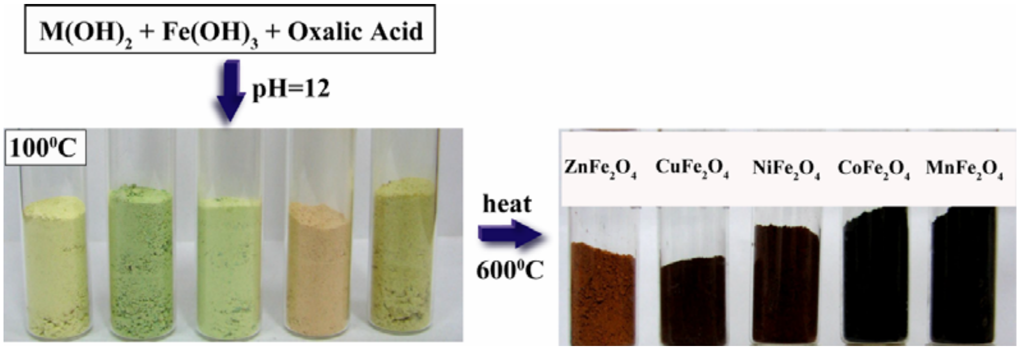

Scheme 4.5. Synthesis of soft metal ferrites by thermolysis of M(II)-organic precursor salts.

case of $MnFe_2O_4$ a mixture of Mn_2O_3 and a very small amount of α-Fe_2O_3 phase was formed (Figure 4.12Ae). With little modification *viz*: duration of thermal decomposition, temperature, pH etc. we can use this technique for synthesis of all the soft as well as hard metal ferrites. Figure 4.13A of Appendix shows the magnetization curves of the different ferrite particles obtained by thermolysis of the precursor salts. Magnetic susceptibility (χ) and coercivity (H_C) values obtained from VSM measurements are given in Table 4.2. Zn ferrite is softest among all with very less coercivity (Hc) of 78 Oe and Co ferrite is having highest H_C of 1494 which falls in between soft and borderline ferrites. Ni, and Co ferrites show a ferromagnetic nature with a hysteresis loop whereas Cu and Mn shows co-existence of ferromagnetic and antiferromagnetic exactly like Zn ferrites as mentioned above. In the present work we have also studied vibration reduction of cantilever beam with tip mass made of these soft magneto-elastic ferrites in collaboration. In such cases, the system has been modeled as a parametrically excited system [4.29]. For carrying out the simulation for vibration reduction of the cantilever beam, electrical conductivity value of the substance is a necessary parameter. As shown in the Table 4.2, the experimentally determined value of electrical conductivity of $ZnFe_2O_4$ was found to be 0.035 Ω^{-1} m^{-1}.

Table 4.2. VSM results of the metal ferrites at T = 300 K.

Sl. No.	MFe_2O_4	Magnetic Susceptibility (χ)	Coercive force (H_c)
1.	$ZnFe_2O_4$	1.19×10^{-3} emu /gOe	78 Oe
2.	$CuFe_2O_4$	2.39×10^{-4} emu /gOe	327 Oe
3.	$NiFe_2O_4$	6.11×10^{-3} emu /gOe	333 Oe
4.	$CoFe_2O_4$	5.49×10^{-3} emu /gOe	1494 Oe
5.	$MnFe_2O_4$	1.19×10^{-3} emu /gOe	146 Oe

Table 4.3. Conductivity measurement of $ZnFe_2O_4$.

Sl. No.	Voltage (mV)	I_{+ve} (μA)	I_{-ve} (μA)	σ ($\Omega^{-1}m^{-1}$)
1.	1	0.16	-0.17	0.0339
2.	2	0.33	-0.34	0.0350
3.	5	0.79	-0.81	0.0335
4.	10	1.58	-1.61	0.0335
5.	20	3.28	-3.32	0.0348
6.	50	8.30	-8.40	0.0350
7.	100	16.70	-16.7o	0.0350
8.	200	33.00	-33.20	0.0350
9.	500	83.70	-83.90	0.0355
10.	1000	169.00	-168.00	0.0359
11.	2000	0.34 mA	-0.338 mA	0.0360

4.2.3. Summary

We have shown the simple, solid-phase efficient, green synthesis of several metal-organic precursor salts. We have observed that regardless of the starting aliphatic organic acid, on thermal decomposition we got metal ferrites. Hence, we can conclude that the molecular level interaction of carboxylic acid groups with metal ion in the solid-state are solely responsible for the formation of corresponding metal oxides. Backbone structure of the organic acid has negligible effect on the modification of the morphology of the thermally decomposed product. Thus, we can conclude the particle agglomeration process during calcinations is dependent on the coordination environment at the molecular level.

4.3. Gel mediated Magnetite mineralization

Magnetite (Fe_3O_4) is a natural magnet and is a member of the spinel group. Magnetite biomineralization is a universal phenomena which is evident in a number of microorganisms *e.g.* magnetotactic bacteria under ambient conditions. In the final part of the thesis, I have reported the formation and growth modification of magnetite micro crystalline minerals in Agarose gel. They are formed by well known gel diffusion technique when doped with soluble $FeSO_4.7H_2O$ and then soaked overnight with $FeCl_3$ followed by diffusion of ammonia solution through pores. After their synthesis we have carried out surface modification for various practical applications such as protein adsorption studies, separation etc. This is because pure magnetic particles may have the following limitations [4.30]: (i) they tend to form large aggregates, (ii) their original structure may get changed if they are not stable enough resulting in the alteration of magnetic properties, and (iii) they can undergo rapid biodegradation when they are directly exposed to the biological system. Therefore, a suitable coating is very necessary to prevent such limitations. To make a stable suspension of particles for practical applications, their dimension should be sufficiently small so that precipitation due to gravitational forces could be avoided.

4.3.1. Experimental section

Synthesis of Magnetite in Agarose gel

In a typical experiment, 0.4 M $FeSO_4.7H_2O$ solution in Milli-Q water was heated to 75-80 ^{O}C and 0.5 % (w/w) of agarose was added, which was further heated to 85-90 ^{O}C to ensure dissolution of agarose. The resulting hot solution was poured into a Petridis and cooled to room temperature slowly. The cooled thick gels plates were cut into cubic pieces about 1 cm^3

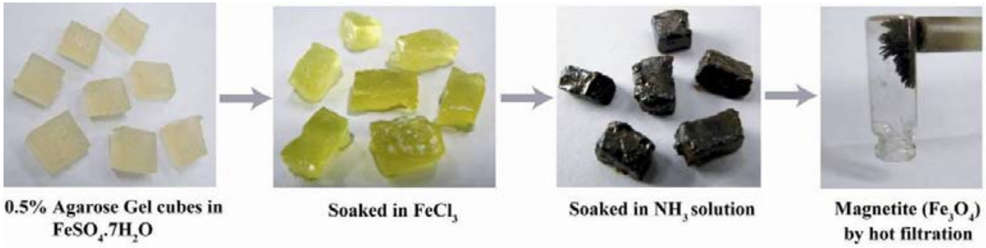

Scheme 4.6. Magnetite synthesis in 0.5% Agarose Gel.

in volume (Scheme 4.6). Then the gel cubic pieces were soaked in 0.4 M solution of anhydrous $FeCl_3$ at 25 ± 1 °C without any mechanical disturbance. After 1-2 days, the gel cubes were rinsed in Milli-Q water to get rid of the unabsorbed residual $FeCl_3$. After that the soft gel cubes were soaked in ammonia solution at 25 ± 2 °C without any mechanical disturbance for another 3 days to allow slow diffusion of ammonia. The resulting magnetite minerals were recovered from the gel matrix by dissolving the gel cubes in Milli-Q water (~95 ^{O}C). Crystalline products were collected through hot vacuum filtration followed by washing several times with Milli-Q, alcohol and diethyl ether. The preliminary experimental results showed that the short period heating in hot water does not affect the crystal morphology considerably.

Hydrophilic and hydrophobic surface modification of magnetite particles

In one set of experiment, Benzene-*1,3,5*-tricarboxylic acid (Trimesic acid, TMA) was adsorbed onto magnetite surface. Having three carboxylate groups TMA may enhance the surface hydrophilic properties upon coating (Scheme 2). Magnetite has a PZC of pH 6.0 - 7.0 [4.31] hence, below pH 6.0 magnetite surface will be positively charged. Again for TMA, pka_{1}, pka_{2}, pka_{3} values are pH~2.8, ~pH 3.7 and ~pH 4.7 respectively. Thus, above pka_{3} value, TMA will be negatively charged [4.32]. In a typical preparation, ~25 mM of TMA was dissolved in 100 ml of methanol followed by continuous addition of 100 mg of magnetite particles in portion wise with continuous stirring. The solution pH was maintained at ~5.0, where TMA is dissociated and magnetite surface is positively charged. After addition of magnetite the solution was stirred continuously for 6-7 h. Resulting mixture was vacuum-filtered and washed with cold water to remove un-adsorbed acids. Similarly Stearic acid (SA) with pK_a of 10.15 was coated/anchored onto magnetite particle following the same procedure (Scheme 4.7) at around pH ~8.0. The adsorption profile of trimesic acid and stearic acid was determined by measuring the concentration of acid remaining in the supernatant by base titration as function of time. Once equilibrium reached, the aliquots were separated from the solid phase by 10 min centrifugation at 10000 rpm in a REMI-2000 (India) centrifuge and subsequent filtration with a 0.2 µm filter paper. The filtrate was further re-suspended and washed with de-ionized milli-Q water to remove un-adsorbed acids and vacuum dried before adsorption studies. TMA and Stearic acid coated magnetite particles were characterized by FT-IR, VSM as shown in Appendix (Figure 4.14A, 4.15A).

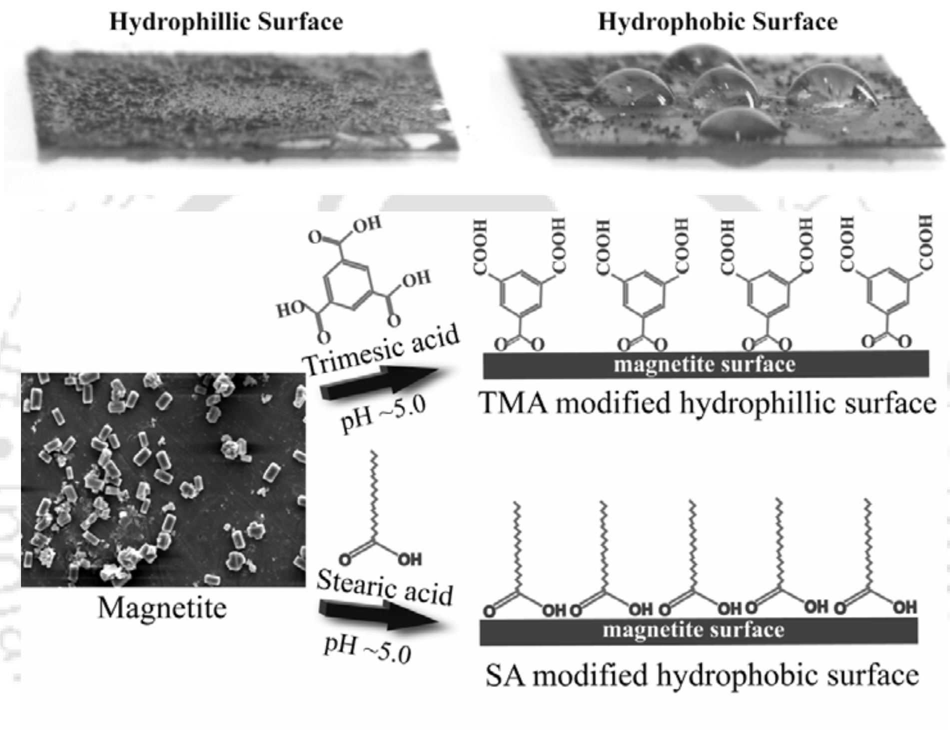

Scheme 4.7. Surface modification of magnetite micro particles.

Surface modification of magnetite with fluorescein

All the adsorption experiments were carried out in batch mode with 5 mL of 500 mg/L fluorescein stock solution in 10 mL specimen tube. Magnetite particles were added in a fixed concentration of 10 g/L and the specimen tubes were kept in a temperature controlled shaker at 200 rpm at room temperature (25 ^{o}C). Adsorption kinetics of fluorescein was followed by withdrawing the samples at regular interval and centrifuged to obtain suitable aliquots for analysis of residual fluorescein concentration. Solution pH was adjusted by adding 0.1 M NaOH and 0.1 M HCl. Isotherm experiments were performed with different initial fluorescein concentration solution (100-1000 mg/L). Adsorption capacity or the q_e value (mg/g) for fluorescein was calculated as follows (Eq.1):

$$q_e = \frac{(C_0 - C_e)\,V}{W} \qquad (1)$$

Where V is volume of solution (mL), C_0 and C_e is the initial and steady state fluorescein concentration respectively (mg/mL) and W weight of the magnetite particles (g). Where, C_o is the initial fluorescein concentration and C_e is steady state fluorescein concentration. In each experiments control was taken for proper validation of adsorption phenomenon. Desorption of fluorescein from magnetite surface was studied by re-suspending the fluorescein loaded solution in different fluorescein free solvent as well as with variation in solution pH. After desorption the fluorescein desorbed into solution was separated from magnetite particle by centrifugation and analyzed by UV-spectrophotometer for actual concentration (Figure 4.16).

Adsorption experiments of BSA

Batch adsorption experiments were performed in 10 mL vials by adding 100 mg (20 g/L) of each magnetite, TMA and stearic acid modified magnetite to 5 mL of BSA aqueous solution of 1 mg/mL concentration. These vials were stirred in an incubator shaker for 6 hrs at room temperature for achieving equilibrium. Preliminary studies showed that this period of time is sufficient to ensure adsorption equilibrium. Solution pH was kept at neutral atmosphere of ~7.0 to represent most of the biological system. Once equilibrium reached the protein adsorbed particles were separated from unbound proteins in solutions by centrifugation at 10000 rpm for 10 min and subsequent filtration. The supernatant was measured for residual BSA concentration in UV-spectrophotometer from the absorbance at 280 nm. The amount of protein adsorbed per unit weight of adsorbent (q_e; mg of BSA/g of NPs) was calculated from equation 1. Where V is volume of solution (mL), C_0 and C_e is the initial and equilibrium protein concentration respectively (mg/mL) and W weight of the adsorbent (g).

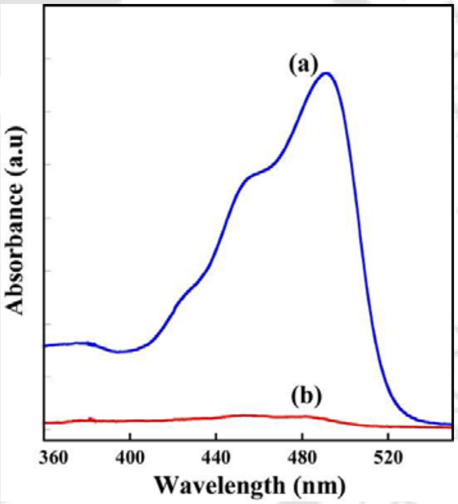

Figure 4.16. Fluorescein solution (a) before addition of magnetite and (b) after addition of magnetite.

Investigation of conformation of BSA at solid interface by fluorescence spectroscopy

The protein adsorbed on magnetite and surface modified magnetite particles are suitable to study in situ structural characteristics of BSA in adsorbed state using fluorescence spectroscopic techniques. These magnetite particles produced negligible light scattering in dispersed particle suspension; therefore can be directly used for fluorescence measurement to provide insight of conformation of proteins at interface. Tertiary structural changes of BSA in native and adsorbed state were measured using a tryptophan fluorescence emission technique in a Varian Cary Eclipse spectrophotometer. The BSA molecules were excited at ~295 nm to achieve mostly the tryptophan emissions. The excitation and emission slit widths both were set at 5 nm. The tryptophan emission fluorescence spectra were collected in the wavelength range of 300 to 420 nm at room temperature. All spectra were corrected for the background emission peak of water. Baseline correction was acquired from suspension of adsorbent particles without BSA.

4.3.2. Result and discussion

Effect of Concentration of Gel

To examine the effect of concentration of the gel on the crystal growth modification, experiments were performed varying the percentage of agarose gel as 1.5 %, 1.0 %, 0.5 % and 0.2 % (w/w). In case of 1.5 % and 1.0 %, hard gel cubes were obtained which results in the formation of very minute amount of precipitate even after 2 weeks. The reason behind this observation is that, with increasing the concentration of gel pore size becomes smaller [4.33], which prevents the easy diffusion of ammonia solution in the gel matrix to form the minerals. Very soft gel plates were formed in 0.2 % gel concentration, which cannot be cut into cubes. Nevertheless, due to the less concentration and large pore size of the gel matrix, Fe^{2+} / Fe^{3+} came out of the matrix easily. This results in the formation of almost immediate precipitation when soaked in ammonia solution. Best results were obtained in 0.5 % agarose gel concentration. Hence, 0.5 % (w/w) gel concentration was used for all the crystallization experiments.

Characterization of Magnetite synthesized in Agarose gel

SEM micrograph (Figure 4.17a) shows rectangular blocks of dimension in the range 500 nm. Previous study [4.34] predicts that the main role agarose gels play on crystallization of minerals is the control on the diffusion process of reactant ions rather in the media and hinder the crystal growth when the crystal size reaches the pore size of the respective network. This was confirmed by considering the pore size for the 0.5 % agarose gels which is around 250 nm [4.35], considerably smaller than the initial rhombohedral calcite crystals. The PXRD analysis confirms their formation with characteristic reflections at 2θ = 30 correspond to (220) plan, 36 correspond to (311) plan, 42 correspond to (400) plan, 58 correspond to (511) plan and 63 correspond to (440) plan which is shown in Figure 4.17b (PDF: 00-001-1111). Magnetic measurements have been carried out by using vibrating sample magnetometer (VSM). The VSM studies (Figure 4.17c) shows Ferromagnetic behavior was observed with an S-shaped hysteresis loop typical of magnetite nanoparticles with sizes larger than 10 nm. From initial slop (Figure 4.17d), the magnetic susceptibility $\chi = M / H$ was found to be 93.58 x 10^{-3} emu /gOe with coercive force (H_c) 34 Oe at $T = 300$ K.

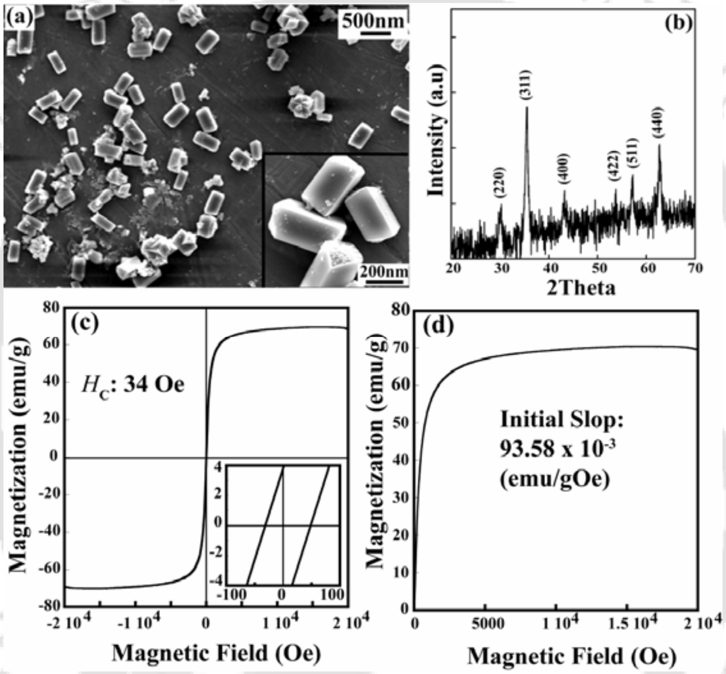

Figure 4.17. (a) SEM micrograph of magnetite, (b) PXRD pattern and (c) VSM hysteresis loop and (d) initial curve.

Fluorescein adsorption on magnetite surface

The adsorption phenomenon of fluorescein on magnetite surface was studied in the pH range of 4.0-8.0 and a high adsorption capacity was noticed (Figure 4.18a). Adsorption capacity (q_e) was almost invariant (47.0 - 49.0 mg/g) within this pH range. Adsorption isotherm was characterized by an initial slope which indicates a high affinity of fluorescein towards magnetite surface towards a plateau value approaching a complete surface coverage (Figure 4.18b).

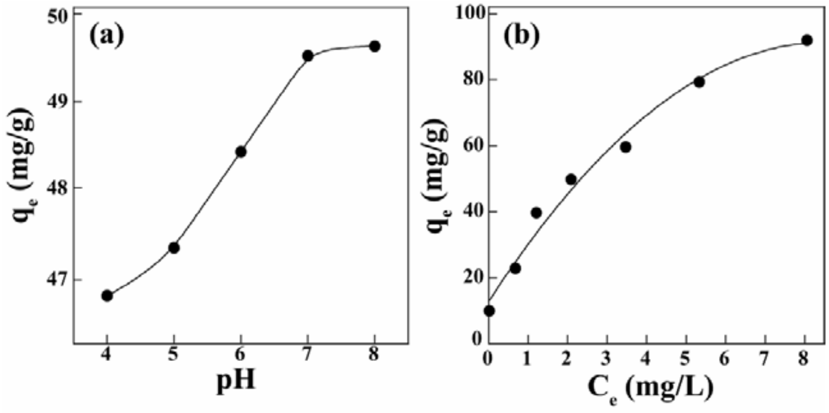

Figure 4.18. (a) Influence of pH on fluorescein adsorption on magnetite surface and (b) adsorption isotherm of fluorescein on magnetite surface at pH 7.0.

Both Langmuir (Eq. 2) and Freundlich (Eq. 3) models have been utilized to analyze the isotherm pattern (Table 4.4) [4.36]

$$q_e = \frac{Q_m b C_e}{1+bC_e} \tag{2}$$

$$q_e = k_f C_e^{1/n} \tag{3}$$

Freundlich isotherm represents a better agreement with the experimental data than Langmuir model (Figure 4.19), which represents a probable multi-layer adsorption of fluorescein on heterogeneous magnetite surface.

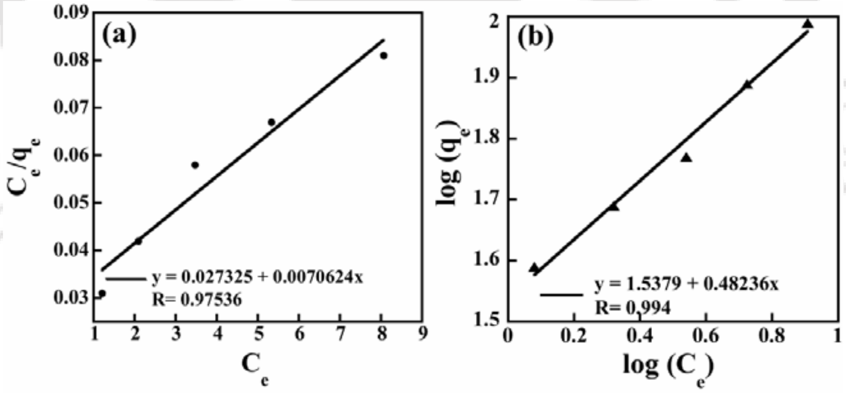

Figure 4.19. (a) Langmuir isotherm model for fluorescein adsorption and (b) Freundlich isotherm model for fluorescein adsorption.

Different isotherm parameters were calculated from the isotherm model analysis and given in Table 4.4. Value of Freundlich exponent factor (n) was 2.08 indicating a favourable adsorption as within a range of 1 -10 [4.36] Maximum adsorption capacity (Q_m) was found ~143 mg/g as calculated from Langmuir model. As described by Hall *et al.* [4.37], an equilibrium parameter R_L is a measure of the favorability of the sorption process. For a favorable reaction process, $0< R_L<1$ and the value achieved for fluorescein adsorption was 0.0007, indicates a favorable adsorption process. The adsorption kinetics was studied with respect to Lagergren pseudo first order (Eq. 4a) and pseudo second order kinetic model (Eq. 4b).

$$\log (q_e - q_t) = \log (q_e) - \frac{1}{2.303} k_1 t \qquad (4a)$$

$$\left(\frac{t}{q_t}\right) = \left(\frac{1}{q_e^2 k_2}\right) + \left(\frac{t}{q_e}\right) \qquad (4b)$$

Adsorption kinetics of fluorescein was very fast on magnetite surface as the steady state reaches within 30 min (Figure 4.20). Second order model was found to better fit for the fluorescein adsorption process (Figure 4.21).

Table 4.4. Parameters of different isotherm model for fluorescein adsorption

Langmuir isotherm				Freundlich isotherm		
Q_m (mg/g)	b (L/mg)	R_L	R	K_f (mg/g)	n	R
142.80	0.259	0.0007	0.875	33.8	2.08	0.994

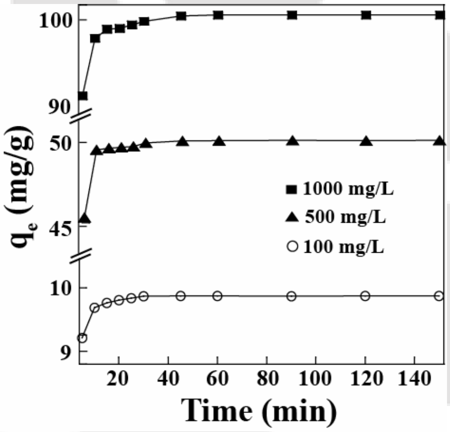

Figure 4.20. Adsorption kinetics of fluorescein on magnetite surface.

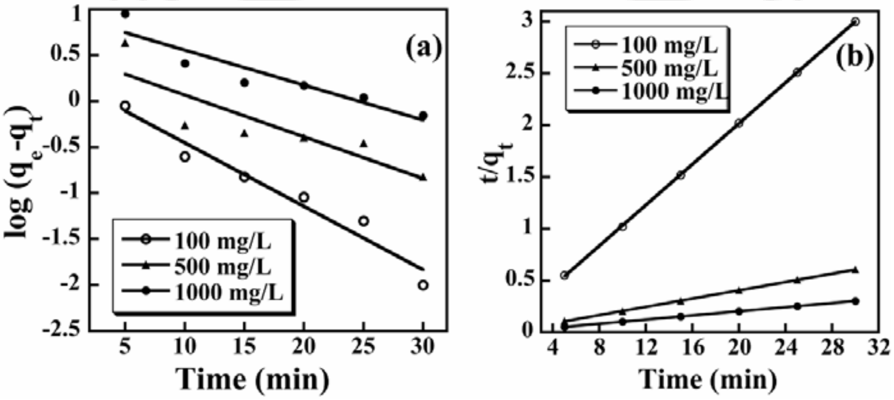

Figure 4.21. (a) 1st order kinetics model for fluorescein adsorption and (b) 2nd order kinetics model for fluorescein adsorption.

Lagergren pseudo first order model shown a correlation coefficient (R) of 0.926 on average, where the second order kinetic model shown a higher R value of 0.999 on average (Table 4.5). In addition, the Chi-square test was also done to support the best fit adsorption model. The equation for evaluating the best fit model is given as [4.38]

$$\chi^2 = \sum \frac{(q_e - q_{em})^2}{q_{em}} \tag{5}$$

Where q_e is the experimentally determined equilibrium solid phase fluorescein concentration and q_{em} is that of calculated from isotherm model. The χ^2 value of 2nd order kinetics (0.0043) was much less than the 1st order fit (3.97), supporting the better fitting of 2nd order model. The standard Gibbs free energy change (ΔG^o) at 25 ^oC of fluorescein adsorption was calculated from

$$\Delta G^o = - RT \ln(k_c) \tag{6}$$

The equilibrium stability constant, k_c was calculated using Eq. 7,

$$k_c = \frac{C_s}{C_e} \tag{7}$$

Where C_s and C_e is the equilibrium fluorescein concentration on adsorbent (mmol/g) and aqueous phase (mmol/L). The ΔG^o values for all concentration from 100 to 1000 mg/L was found to be negative (-15 KJ mol^{-1} to -6 KJ mol^{-1}) and therefore favorable for fluorescein adsorption.

Table 4.5. Comparison of first and second order kinetic model of fluorescein adsorption

Initial concentration (mg/L)	Experimental q_e value (mg/g)	First order kinetics			Second order kinetics		
		k_1 (l min^{-1})	R value	χ^2	k_2 (g mg^{-1} min^{-1})	R value	χ^2
100	9.99	0.156	0.977	3.97	0.204	0.999	0.0043
500	49.65	0.103	0.871		0.054	0.999	
1000	93.4	0.087	0.932		0.028	0.999	

Desorption of fluorescein

To ensure the stability of fluorescein coated magnetite, we have studied it's desorption phenomenon in different fluorescein free solvent. Once adsorbed, the coated magnetite particles were dried and re-suspended in a fluorescein free aqueous solution (pH ~7.0). These particles were found to be much stable in aqueous solution as only 1-3% desorption of fluorescein was noticed. Again, almost ~100% desorption was achieved while re-suspending in 1 M NaOH solution; whereas, re-suspending in 1 M HCl solution resulted in ~25% desorption. In non-aqueous solutions like methanol, desorption was very less (5-6%) and it has been found that fluorescein loaded magnetite particles were totally stable in a non-polar solvent like hexane as no fluorescein was found to desorb into the solution. Magnetite particles after fluorescein adsorption are shown in Figure 4.22.

BSA adsorption studies on organic acid modified magnetite particles

Equilibrium adsorption studies of BSA on magnetite and organic acid modified magnetite particles reveal a variation in adsorption capacity of BSA on different surfaces. Bare magnetite particles have been found to have an adsorption capacity of ~28 mg/g which increases to ~35 mg/g upon TMA coating. TMA modification generates a more hydrophilic surface having the carboxylate moieties. The increment in adsorption capacity upon TMA coating is might be due to the presence of these high number of carboxyl moieties on the magnetite surface which can strongly anchor BSA via hydrophilic and/or electrostatic interaction. In contrary, stearic acid modified surface showed a reduction in adsorption capacity, as only 10 - 20 % of initial BSA as found to adsorb. The carboxylate group in stearic acid molecule is reactive and can form hydrogen bonding easily with the magnetite surface, thus can generate a hydrophobic surface. Some previous reports on increased adsorption of proteins on stearic acid modified surface have been found which is different from our result [4.39]. A probable explanation to this can be the attachment of the carboxyl head group of stearic acid with magnetite surface and protruding the hydrophobic tails outwards. This might generate a flexible hydrophobic modified surface (Figure 4.23) in contrast to the previous cases where the horizontal interaction of hydrophobic tails with the solid surface (along with the head group of stearic acid moieties) generates a rigid-hydrophobic surface which has high affinity for protein binding. Flexibility of any modified layers has a good impact on protein adsorption features as it can reduce the protein adsorption more than rigid moieties. Hence the reduced BSA adsorption profile upon stearic acid modified surface may be an indication of a flexible layer of stearic acid hydrophobic tails on magnetite surface. Moreover,

Figure 4.22. Fluorescence optical microscope image of magnetite particles (a) before and (b) after fluorescein adsorption.

density of a coated layer has a high influence on protein adsorption, leading to complete rejection of protein at high dense grafting. Hence, the low adsorption capacity of BSA on stearic acid modified surface also indicates a high density of fatty acid layers. Being neutral, the hydrophobic tails of stearic acid moieties seems to have no electrostatic interaction with the BSA molecules and therefore interact differently with BSA molecules compared to rigid TMA moieties or bare magnetite surface. Therefore, the surface modification of magnetite particles with hydrophobic and hydrophilic moieties was found to have a strong influence on BSA adsorption compared to bare magnetite surface.

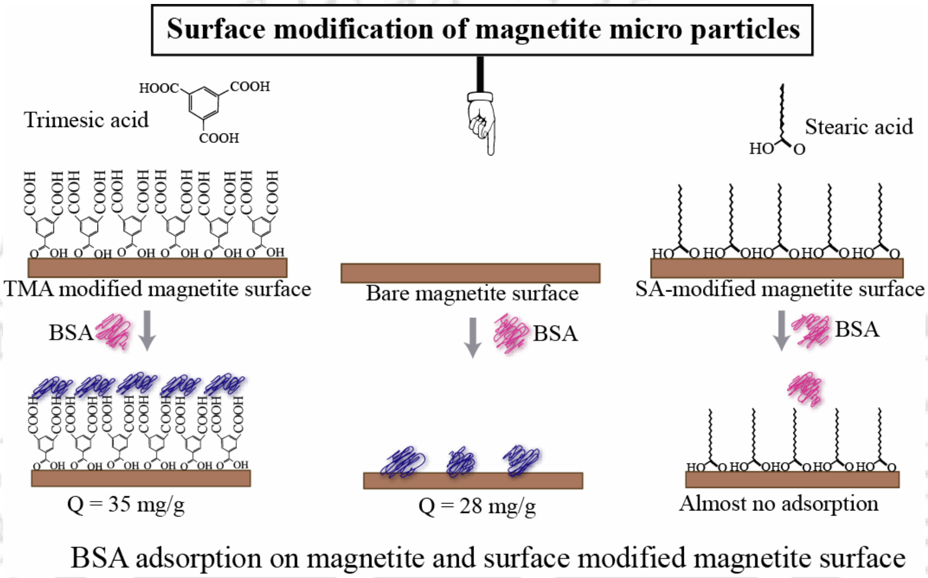

Figure 4.23. Adsorption of BSA on magnetite and surface modified magnetite surface.

Fluorescence emission spectroscopy for BSA structural analysis

The fluorescence emission of BSA at native solution, and adsorbed on bare magnetite, TMA- magnetite and stearic acid modified magnetite particles is shown in Figure 4.24. BSA possesses two tryptophan residues (Trp_{213} and Trp_{134}). Being on the surface of the molecule Trp_{134} contributes the major part in BSA fluorescence [4.40]. The characteristic emission maximum of BSA in native solution is at ~ 343 nm (Figure 4.24a) indicates that the Trp_{134} is fully exposed to aqueous solvent [4.41]. Upon adsorption on different surfaces, quenching in fluorescence intensity was observed in all cases. The quenching of fluorescence intensity might be due to the presence of strong tryptophan quenching groups like cysteine in spatial proximity of Trp or exposure to a less hydrophilic atmosphere [4.42] TMA modified magnetite-BSA interaction seems to have more influence on BSA native structure than the bare magnetite one (Figure 4.24b) as emission spectra of BSA on TMA modified magnetite particles quenched totally (Figure 4.24c). This represents a more un-ordered tertiary structure of BSA upon anchored on carboxylate modified surface, which might be due to the strong hydrophilic and/or electrostatic interaction of BSA with carboxyl moieties. However, BSA on stearic acid modified magnetite surface showed a little quenching in its emission intensity (Figure 4.24d). This implies a minor alteration in tertiary structure of BSA upon interaction with stearic acid modified layers and retention of mostly native structure. Thus, surface modification with TMA and stearic acid was found to have a strong influence on protein tertiary structure along with the adsorption phenomenon.

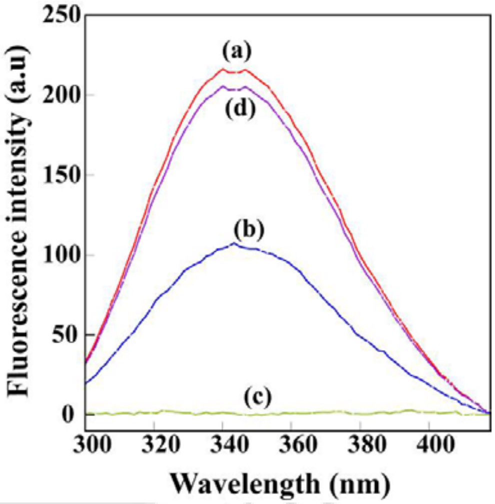

Figure 4.24. Fluorescence emission spectra of (a) native BSA, (b) BSA + bare Fe_3O_4, (c) BSA + TMA modified Fe_3O_4 and (d) BSA + SA modified Fe_3O_4.

4.3.3. Summary

The advantage of gel diffusion technique over other non-gel adsorption processes is that, it is capable of characterizing the effects of matrix molecules on mineralization by using very small quantities of material. Again due to constraints of stirring and evaporation, it is difficult to reduce the volume of a solution reaction to less than a few milliliters without the use of gels. On the other hand, a biomolecule can be dissolved or suspended in a small volume of gel where it is ‘‘trapped’’ by diffusion [4.43], allowing precipitation studies to be done in 100 μL or less. These methods provide a portrait of how matrix molecules act to nucleate, inhibit, or modify mineral formation, and how the structural features of these molecules affect the mineralization process. We have shown the versatility of this process by characterizing eight different biologically important minerals from agarose gel matrix. It is speculated that agarose gels mainly play a role of control on the diffusion process of reactant ions, which might have relevant biological implications.

References

[4.1] H. F. Janos, Nanoparticles and Nanostructured Films, Preparation, Characterization and Applications, Wiley/VCH, Weinheim, (1998).

[4.2] J. H. Smatt , N. Schuwer , M. Jarn , W. Lindner , M. Linden, Micropor. Mesopor. Mat. 112 (2007) 308.

[4.3] H. Thakuria, B. M. Borah, G. Das, J. Mol. Cat. A 274 (2007) 1.

[4.4] K. Nakamoto, Infrared and Ramman Spectra of Inorganic and Coordination Compounds. 5th Ed. John Wiley & Sons. Inc. New York (1997).

[4.5] R. A. Nyquist, R.O. Kagel, Infrared Spectra of Inorganic Compounds, Academic Press, Inc., New York and London, 1971, pp. 220.

[4.6] V. Biju, M. Abdul Khadar, Spectrochim. Acta, Part A: Mol. Biomol. Spect. 59 (2003) 121.

[4.7] J. A. Gaddsden, Infrared Spectra of Minerals and Related Inorganic Compounds, Butterworth, London, (1975).

[4.8] Y. Meng, D. Chen, X. Jiao, J. Phys. Chem. B 110 (2006) 15212.

[4.9] Y. Liu, W. Ren, L. Y. Zhang, X. Yao, Thin Solid Films 353 (1999) 124.

[4.10] B. Gillot, M. El Guendouzi, M. Laarj, Mater. Chem. Phys. 70 (2001) 54.

[4.11] P. M. Sousa, A. J. Silvestre, N. Popovici, M. L. Paramês, O. Conde, Mat. Sci. Forum 20 (2004) 455.

[4.12] O. Seiferth, K.Wolter, B. Dilmann, G. Klivenyi, H.-J. Freund, D. Scarano, A. Zecchina, Surf. Sci. 421 (1999) 176.

[4.13] Taubert, G. Wegner, J. Mater. Chem. 12 (2002) 805.

[4.14] J. Zhang, L. Sun, J. Yin, H. Su, C. Liao, C. Yan, Chem. Mater. 14 (2002) 4172

[4.15] L. Guo, S. H. Yang, C. L. Yang, P. Yu, J. N. Wang, W. K. Ge, G. K. L. Wong, Appl. Phys. Lett. 76 (2000) 2901.

[4.16] S. A. Studenikin, N. Golego, M. Cocivera, J. Appl. Phys. 84 (1998) 2287.

[4.17] H. M. Xiao, L. P. Zhu, X. M. Liu, S. Y. Fu, Solid State Commun. 141 (2007) 431.

[4.18] (a) S. Thota, J. Kumar, J. Phys. Chem. Solids 68 (2007) 1951, (b) J. Nogues, I.K. Schuller, J. Magn. Magn. Mater. 192 (1999) 203.

[4.19] Y. Ichiyanagi, Y. Kimishima, S. Yamada, J. Magn. Magn. Mater. e1245 (2004) 272.

[4.20] (a) M. Tadic, D. Markovic , V. Spasojevic , V. Kusigerski,M. Remskar, J. Pirnat, Z. Jaglicic, J. Alloy Compd. 441 (2007) 291, (b) A. Oles, F. Kajzar, M. Kucab,W. Sikora, Magnetic Structures Determined by Neutron Diffraction, Panstwowe Wydawnictwo Naukowe, Warszawa- Krakow (1976) p. 372, (c) C. Guilland, J. Phys. Radium 12 (1951) 489.

[4.21] M. Regulski, R. Przeniosło, I. Sosnowska, D. Hohlwein, R. Schneider, J. Alloy. Compd. 362 (2004) 236–240.

[4.22] L. E. T. Feliciano, A. J. A. de Oliveira, W. H. Schreiner, E. C. Pereira, J. Electroanal. Chem. 574 (2005) 333.

[4.23] (a) M. Sugimoto, J. Am. Ceram. Soc. 82 (1999) 269, (b) K. Raj, B. Moskowitz, R. Casciari, J. Magn. Magn. Mater. 149 (1995) 174.

[4.24] Z. Sun, L. Liu, D. Z. Jia , W. Pan, Sens. Actuators B 125 (2007) 144.

[4.25] K. Nakamoto, Infrared and Ramman Spectra of Inorganic and Coordination Compounds. 5th Ed. John Wiley & Sons. Inc. New York (1997).

[4.26] F. Li, H.Wang, L.Wang, J.Wang, J. Magn. Magn. Mater. 309 (2007) 295.

[4.27] D. Fiorani, S. Vitiocoli, J.L. Dorman, J.L. Tholence, A.P. Murani, Phys. Rev. B 30 (1984) 2776

[4.28] D. Fiorani, S. Viticoli, J. Magn. Magn. Mater. 49 (1985) 83.

[4.29] (a) A. H. Nayfeh, D. T. Mook, Nonlinear Oscillations, Wiley, New York (1995), (b) A. H. Nayfeh, B. Balachandran, Applied Nonlinear Dynamics—Analytical, Computational and Experimental Methods, Wiley, Canada (1995), (c) M. P. Cartmell, Introduction to Linear Parametric and Non-linear Vibrations, Chapman and Hall, London (1990).

[4.30] S. Santra, R. Tapec, N. Theodoropoulou, J. Dobson, A. Hebard,, W. Tan, Langmuir 17 (2001**)** 2900.

[4.31] (a) G. A. Parks, Chem. Rev. 65 (1965) 177, (b) M. Kosmulski, J. Coll. Inter. Sci. 275 (2004) 214.

[4.31] X. H. Guan, G. H. Chen, C. Shang, J. Coll. Inter. Sci. 301 (2006) 419.

[4.32] N. Pernodet. M. Maaloum. B. Tinland. Electrophoresis 18 (1997) 55.

[4.33] D. Yang, L. Qi, J. Ma, Chem. Commun. (2003) 1180.

[4.34] C. I. D. Bica, R. Borsali, E. Geissler, C. Rochas, Macromolecules 34 (2001) 5275.

[4.35] H. M. F. Freundlich, Z. Phys. Chem. 57A (1906) 385.

[4.36] K. R. Hall, L. C. Eagleton, A. Acrivos, T. Vermeulen, Ind. Eng. Chem. Fund. 5 (1966) 212.

[4.37] Y. S. Ho, W. Chiu, C. Wang, Bioresource Technol. 96 (2005) 1285.

[4.38] W.G. Pitt, S.L. Cooper, J. Biomed. Mater. Res. 22 (1988) 359.

[4.39] C. D. Wilson, S.G. Roscoe, Langmuir 20 (2004) 7547.

[4.40] B. Klajnert, L. Stanislawska, M. Bryszewska, B**.** Palecz, Biochm. Biophy. Acta 115 (2003) 1648.

[4.41] A. Filenko, M. Demchenko, Z. Mustafaeva, Y. Osada, M. Mustafaev, Biomacromolecules 2 (2001) 270.

[4.42] J. R. Lakowicz, Principles of Fluorescence Spectroscopy, 2nd ed.; Springer: New York, (2006).

[4.43] A. L. Boskey, M. Maresca, W. Ullrich, S. B. Doty, W. T. Butler, C. W. Prince, Bone Miner. 22 (1993) 147.

Table 2.1A. Crystallographic refinement parameters of Ca-TMA co-ordination polymer.

CCDC No.	648775	Empirical formula	$C_9H_{12}CaO_{10}$
Fw	320.27	Temp, K	273(2)
Radiation	Mo Kα	Wavelength	0.71073 Å
Size, mm	0.45 x 0.36 x 0.31	crystal system	Monoclinic
Space group	P2(1)/c	a, Å	10.202(4)
b, Å	16.449(7)	c, Å	7.476(3)
β, deg	102.316(2)	V, $Å^3$	1225.66(9)
Z	4	ρ_{calc} mg/m^3	1.730
μ	0.560	*F(000)*	512
GOF(S)	1.006	final R indices [$I > 2\sigma(I)$]	R1=0.0731 wR2=0.2037
R indices (all data)	R1=0.0810 wR2= 0.2096	Refinment	Full-matrix least-squares on F^2.

Table 2.2A. Selected Bond length (Å) and bond angles (°) of Ca-trimesic acid complex.

Ca1 - O1	2.334(3)	Ca1 - O3	2.469(3)	Ca1 - O5	2.320(3)
Ca1 - O7	2.476(4)	Ca1 - O8	2.360(4)	Ca1 - O9	2.413(3)
Ca1 - O10	2.386(4)				

O5 Ca1 O1	148.29(12)	O1 Ca1 O3	131.44(11)	O5 Ca1 O3	79.85(10)
O5 Ca1 O8	106.76(14)	O8 Ca1 O3	74.28(13)	O3 Ca1 O7	131.17(12)
O1 Ca1 O8	81.71(13)	O10 Ca1 O3	124.41(14)	O10 Ca1 O9	77.00(13)
O5 Ca1 O10	83.31(13)	O9 Ca1 O3	69.13(11)	O9 Ca1 O7	158.97(13)
O1 Ca1 O10	81.40(13)	O5 Ca1 O7	72.31(13)	O8 Ca1 O9	109.20(13)
O8 Ca1 O10	160.70(15)	O1 Ca1 O7	80.50(13)	O10 Ca1 O7	91.58(14)
O5 Ca1 O9	122.73(13)	O8 Ca1 O7	76.46(13)	O1 Ca1 O9	80.36(12)

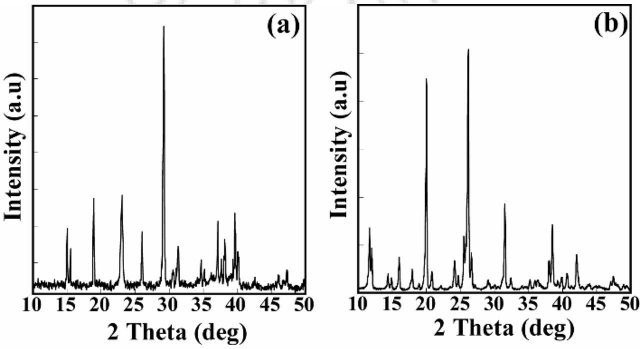

Figure 4.1A. PXRD of the precursor salt of Cu with (a) oxalic acid, (b) succinic acid.

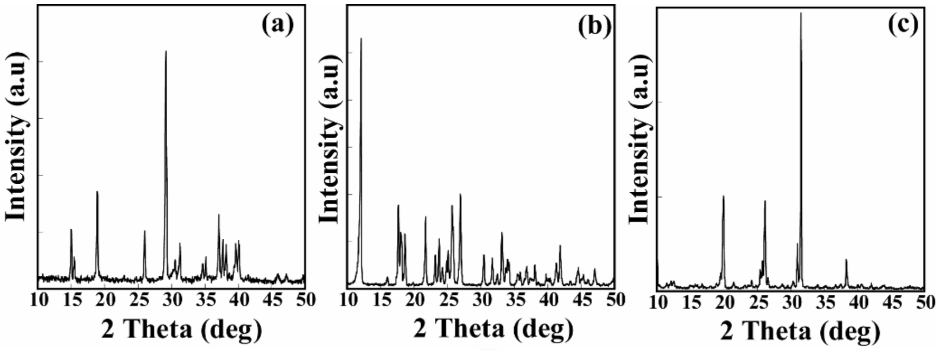

Figure 4.2A. PXRD of the precursor salt of Ni with (a) oxalic acid, (b) malonic acid and (c) succinic acid.

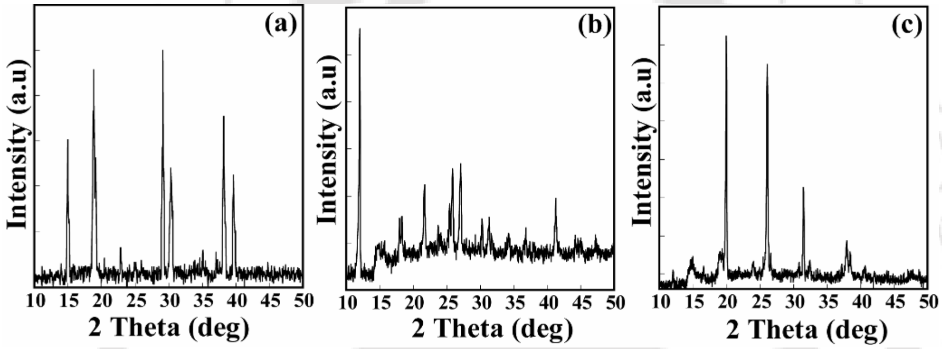

Figure 4.3A. PXRD of the precursor salt of Co with (a) oxalic acid, (b) malonic acid and (c) succinic acid.

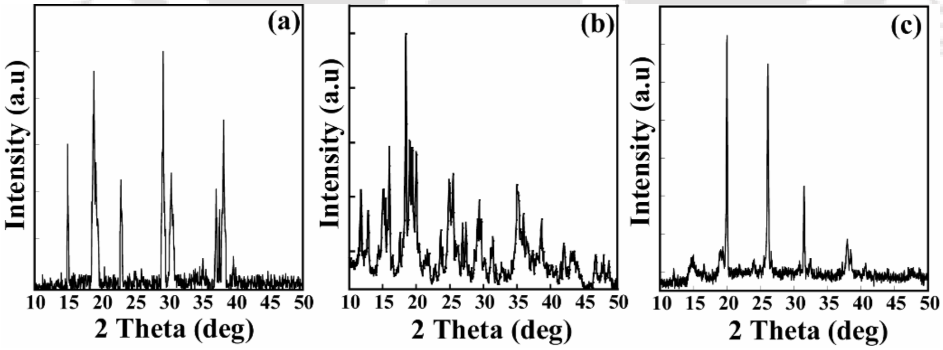

Figure 4.4A. PXRD of the precursor salt of Fe with (a) oxalic acid, (b) malonic acid and (c) succinic acid.

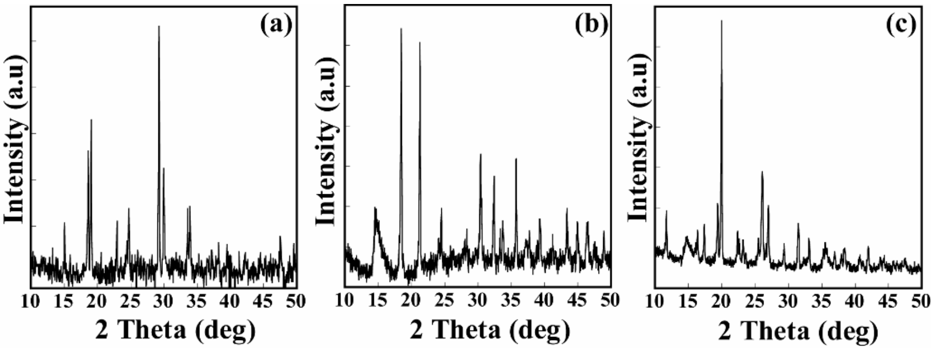

Figure 4.5A. PXRD of the precursor salt of Mn with (a) oxalic acid, (b) malonic acid and (c) succinic acid.

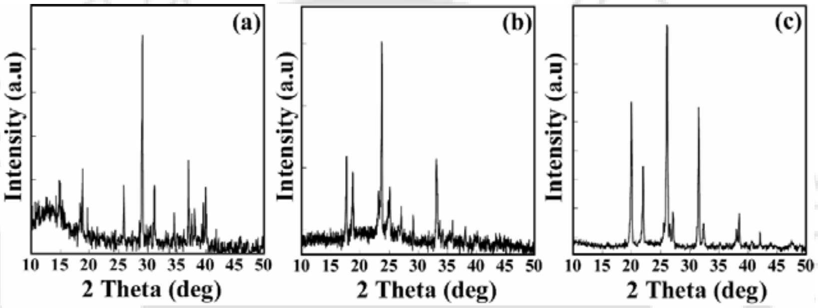

Figure 4.6A. PXRD of the precursor salt of Mn with (a) oxalic acid, (b) malonic acid and (c) succinic acid.

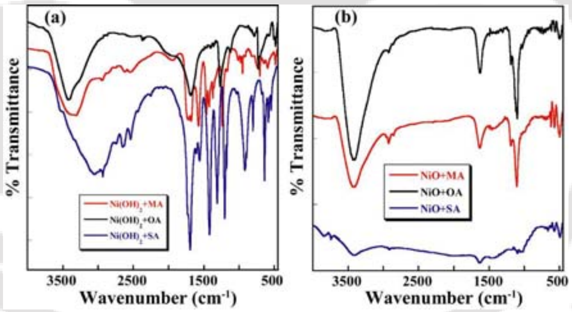

Figure 4.7A. FT-IR of the Ni-organic acid precursor salt (a) before heating and (b) after heating.

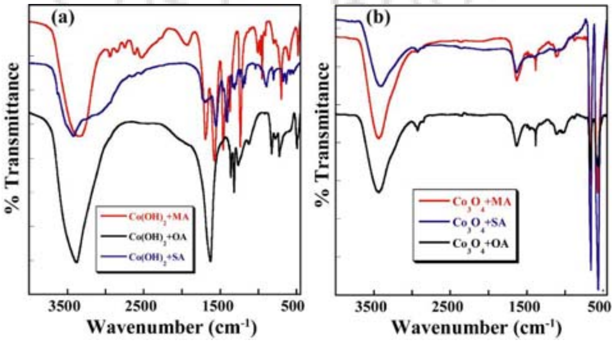

Figure 4.8A. FT-IR of the Co-organic acid precursor salt (a) before heating and (b) after heating.

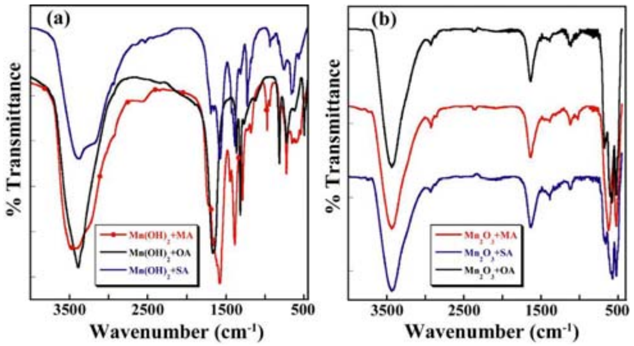

Figure 4.9A. FT-IR of the Mn-organic acid precursor salt (a) before heating and (b) after heating.

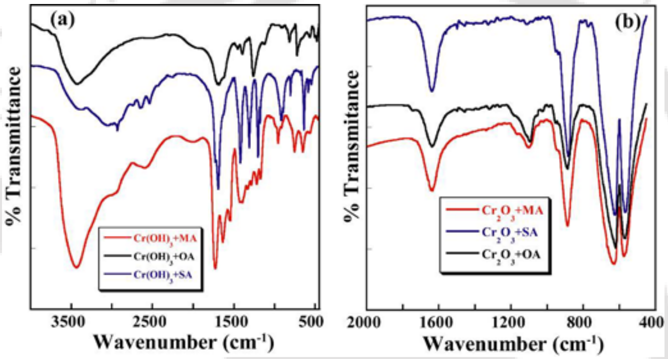

Figure 4.10A. FT-IR of the Cr-organic acid precursor salt (a) before heating and (b) after heating.

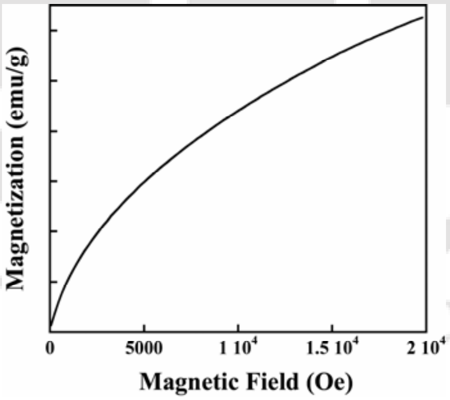

Figure 4.11A. VSM initial M/H curve of $ZnFe_2O_4$ nanoparticle.

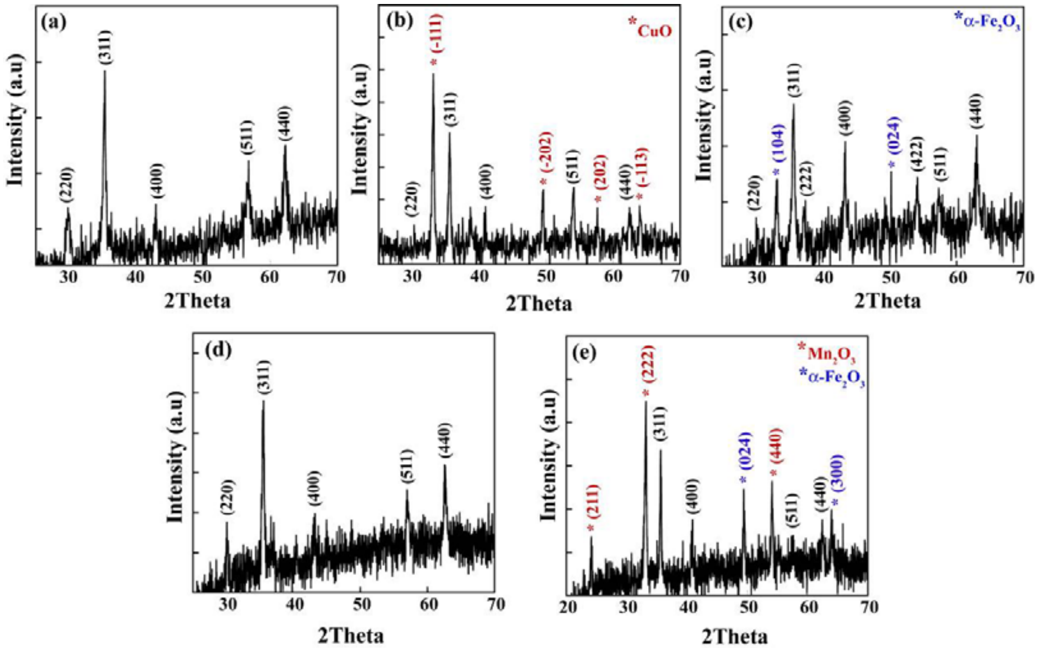

Figure 4.12A. PXRD pattern of (a) $ZnFe_2O_4$, (b) $CuFe_2O_4$, (c) $NiFe_2O_4$, (d) $CoFe_2O_4$ and (e) $MnFe_2O_4$.

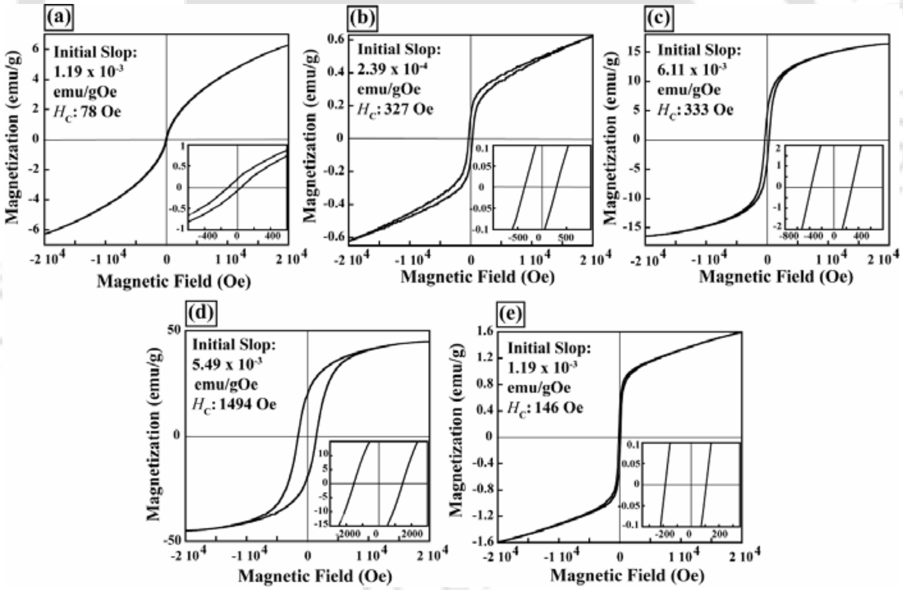

Figure 4.13A. VSM studies of (a) $ZnFe_2O_4$, (b) $CuFe_2O_4$, (c) $NiFe_2O_4$, (d) $CoFe_2O_4$ and (e) $MnFe_2O_4$.

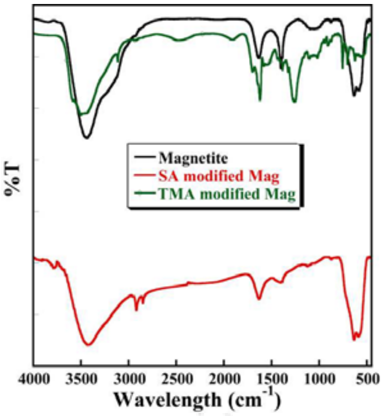

Figure 4.14A. FT-IR of Magnetite (black line), TMA modified magnetite(green line) and SA modified magnetite (red line).

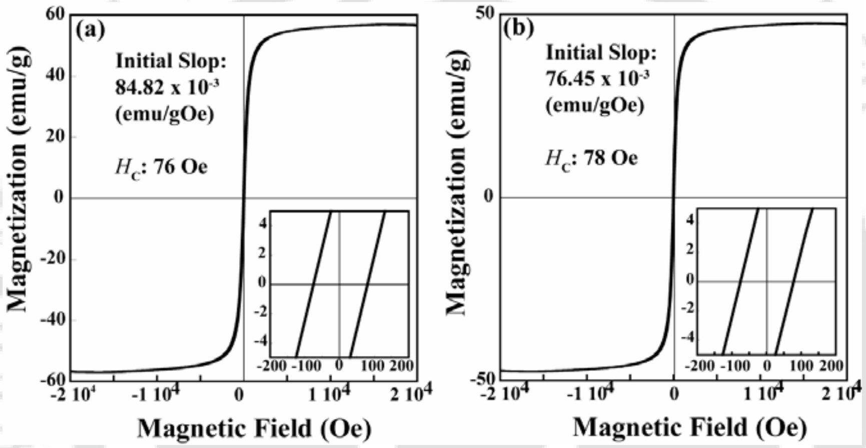

Figure 4.15A. VSM of (a) TMA modified magnetite and (b) SA modified magnetite.

LIST OF PUBLICATIONS

1) “A one-pot synthesis and self assembled superstructure of an oeganic salt of 1,5-benzodiazepine derivative” H. Thakuria, A. Pramanik, **B. M. Borah,** G. Das, Tetrahedron Lett. 2006, 47(18), 3135-3138.
2) “Low-Molecular-Weight Poly-Carboxylate as Crystal Growth Modifier in Biomineralization” **B. M. Borah,** B. J. Bhuyan, Gopal Das, J. Chem. Sci, 2006, 118(6), 519-524.
3) “Zno Nano Particle from Metal-Organic Framework of Zn(II)-Metacycles” H. Thakuria, **B. M. Borah,** G. Das, Eur. J. Inorg. Chem. 2007, 524-529.
4) “Macroporous metal oxides as an efficient heterogeneous catalyst for various organic transformations—A comparative study” H. Thakuria, **B. M. Borah,** G. Das, J. Mol. Cat. A, 2007, 274, 1-10.
5) “Solid State Synthesis and Hierarchical Supramolecular Self-assembly of Organic Salt Cocrystals” H. Thakuria, **B. M. Borah**, A. Pramanik, G. Das, J. Chem. Cryst. 2007, 37, 807-816.
6) “Biomimetic Modulation of Crystal Morphology using Gel: From Nano to Micron Scale Architecture” **B. M. Borah,** P. Hema Lakshmi, Gopal Das, Mat. Sci. Eng. C 2008, 28, 1173–1182.
7) “Lactic Acid Bacterial Extract as a Biogenic Mineral Growth Modifier” **B. M. Borah,** A. K. Singh, A. Ramesh, G. Das, J. Cryst. Growth 2009 (*article in press*).
8) “Additive control CaCO3 polymorph synthesis” **B. M. Borah,** G. Das *(submitted)*.
9) “High-Molecular-Weight Proteins from Lemon as a Biogenic Crystal Growth Modifier” **B. M. Borah,** G. Das *(submitted)*.
10) “Solid-State Precursor Synthesis of Macroporous Metal Oxides: A comparative study” **B. M. Borah**, B. Ojha, G. Das *(submitted)*.
11) “Solid State Synthesis of $ZnFe_2O_4$ nanoparticles as a materials for Vibration Reduction of Cantilever Beam” **B. M. Borah**, B. Ojha, G. Das *(submitted)*.
12) “Gel mediated Magnetite synthesis and their surface modification for protein adsorption studies” **B. M. Borah**, B. Saha, S. K. Dey, G. Das *(submitted)*.